NTNU

Norwegian University of
Science and Technology

Electrical Characterization of Amorphous Silicon Nitride Passivation Layers for Crystalline Silicon Solar Cells

Susanne Helland

Nanotechnology
Submission date: June 2011
Supervisor: Eivind Øvrelid, IMTE
Co-supervisor: Ørnulf Nordseth, Institutt for Energiteknikk
                             Erik S. Marstein, Institutt for Energiteknikk

Norwegian University of Science and Technology
Department of Materials Science and Engineering

Preface

The work on this master's thesis was carried out at the Department for Solar Energy at Institute for Energy Technology, during spring 2011. The assignment was developed by Ørnulf Nordseth (IFE) and Erik Stensrud Marstein (IFE), and Eivind Johannes Øvrelid (NTNU) was responsible supervisor. The work has been performed independently, and according to NTNU regulations.

I wish to thank Ørnulf Nordseth for outstanding guidance and experimental training throughout the process. Erik Stensrud Marstein is acknowledged for inspiration, technical discussions and feedback. Additionally, I am grateful for the help of Eduard Monakhov (IFE) with the conductance method and the help from Martin Kirkengen (REC) through useful discussions. I would like to thank Halvard Haug (IFE) and Lars Løvlie (IFE) for enjoyable cooperation, good dialogues and support, and Jostein Thorstensen for performing much appreciated laser processing. I wish to thank all students in the Nanotechnology class of 2011 and the researchers at the Department for Solar Energy for making my student days enjoyable and memorable. Last but not least, Mario: I am sincerely grateful for your support and endless patience.

Susanne Helland
Kjeller, 14 June, 2011

Abstract

High quality surface passivation is important for the reduction of recombination losses in solar cells. In this work, the passivation properties of amorphous hydrogenated silicon nitride for crystalline silicon solar cells were investigated, using electrical characterization, lifetime measurements and spectroscopic ellipsometry. Thin films of varying composition were deposited on p-type monocrystalline silicon wafers by plasma enhanced chemical vapor deposition (PECVD). Highest quality surface passivation was obtained for silicon-rich thin films, where a surface recombination velocity of 30 cm/s was obtained after a heat treatment corresponding to the industrial contact firing process. Electrical characterization of the interface between silicon nitride and silicon was performed by capacitance and conductance measurements. Several challenging aspects related to the interpretation of these measurements were investigated in detail, including charging and discharging, leakage currents, and frequency dependent capacitance.

Table of Contents

1 Introduction

In light of future challenges concerning increasing energy demand, decreasing reservoirs of fossil fuels, and climate change, the interest in renewable energy has increased dramatically worldwide. Solar energy has a great potential of contributing to a sustainable development, and tremendous progress has been made in photovoltaics, by which sunlight is converted directly into electric power [1]. However, power generation from photovoltaics needs to become more cost effective in order to compete with other energy sources [2]. The solar cell based on crystalline silicon is dominating the marketplace, and further cost reduction is necessary for the industry to grow [2]. Ways of reducing the price per watt of the electricity produced by solar panels include developing more efficient solar cells and reducing the production cost [2].

Recombination of charge carriers in the silicon material is a significant loss mechanism in industrial solar cells today, and recombination losses must be minimized in order to make high efficiency solar cells [3]. Surface recombination losses are reduced by passivating the surface using dielectric films. The front sides of industrially produced silicon solar cells are passivated by deposition of a thin layer of amorphous hydrogenated silicon nitride, a-SiN$_x$:H [3]. An advantage of a-SiN$_x$:H as a passivation material is that passivation is achieved by two effects simultaneously. Chemical bonding between the film and the silicon substrate results in chemical passivation, while fixed positive charges near the silicon surface cause field-effect passivation [4]. In addition to good surface passivation properties, the silicon nitride film serves an important function as an anti-reflection coating, attributing to the characteristic blue color of silicon solar cells [3]. In order to reduce surface recombination losses further, passivation of the rear side of the solar cells is also important [2]. Today's solar cells have a small degree of rear passivation from aluminium atoms diffusing from the rear contact into the silicon, giving field-effect passivation [2]. However, the interface between silicon and metal features a very high surface recombination velocity [3]. Due to high material costs, the wafer thickness is continuously decreased, and the solar cells become thinner. As a consequence, rear passivation becomes more important in order to achieve high cell efficiencies [3]. By depositing a dielectric passivation film on the rear side of the solar cell, and using laser processing to create localized contacts, better surface passivation can be achieved and lower amounts of expensive aluminium paste is needed [2, 3, 5].

An example of a solar cell design with a-SiN$_x$:H passivation layers on both front and rear side of the cell is shown in Figure 1 [3]. The front contacts are screen printed silver contacts, extensively used in industrial solar cells. At the rear of the cell, aluminium point contacts with localized back surface fields (BSF) give field effect passivation close to the contact in addition to minimizing the metal-silicon interface area.

Screen printed silver front contacts

n$^+$-Si

p -Si

Local aluminium BSF

a-SiN$_X$:H

Aluminium rear contacts
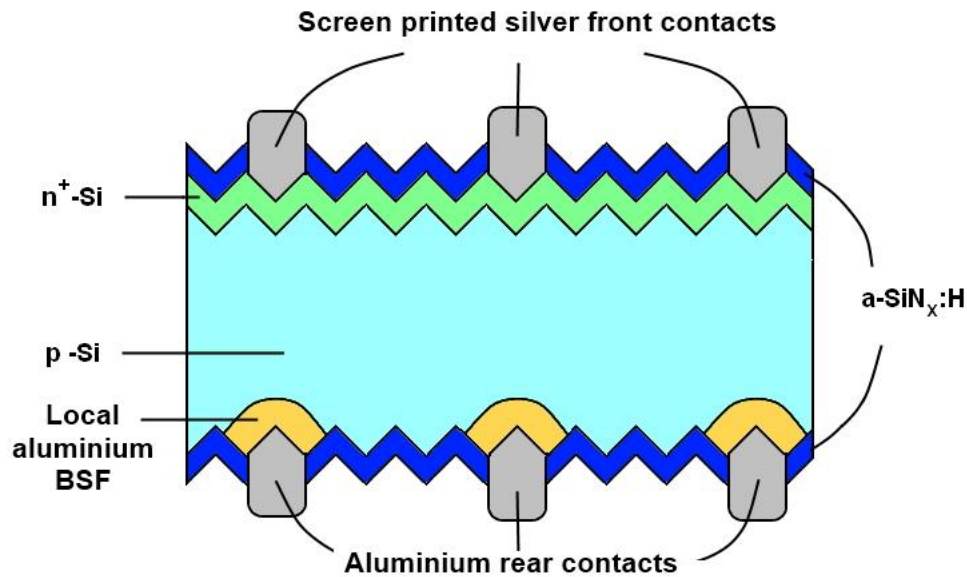
Figure 1: **Example of solar cell design with a-SiN$_x$:H passivation layers at front and rear side.**

Plasma enhanced chemical vapor deposition (PECVD) is the most common deposition method for a-SiN$_x$:H in the industry today. The quality of passivation depends on film properties, which are controlled by various deposition parameters. Additionally, the heat treatment associated with screen printing of front contacts affects the passivation layer. A great deal of research has focused on optimization of the deposition process with the aim of achieving high quality surface passivation of silicon for photovoltaic applications [6-14]. However, a large variety of PECVD reactor designs exist, and optimization of deposition parameters depends on the equipment used.

Electrical characterization is extensively used in order to investigate the properties of a-SiN$_x$:H dielectric films for microelectronics applications [15-23]. However, it is not widely used for characterization of a-SiN$_x$:H passivation layers for photovoltaic applications, and difficulties with respect to methodology and interpretation of results are reported [4, 6, 24].

1.1 Thesis outline

In this work, surface passivation of silicon using a-SiN$_x$:H deposited by PECVD is explored. The experiments are limited to passivation of p-type substrates, for passivation of the rear side of solar cells with n^+p configuration. However, the aspects regarding passivation properties of a-SiN$_x$:H on p-type silicon are also applicable to a-SiN$_x$:H passivation layers on n-type substrates and emitters. This work is part of a larger research project at the Department for Solar Energy at Institute for Energy Technology, and film deposition is performed in cooperation with PhD student Halvard Haug and research scientist Dr. Ørnulf Nordseth.

The objective of my work can be summarized in 4 key goals:

1. Investigate properties of passivation layers using electrical characterization, in addition to more traditional characterization techniques in photovoltaic research, in order to achieve a more fundamental understanding of the passivation properties of a-SiN$_x$:H

2. Separate the contributions from chemical and field-effect passivation using electrical characterization, and linking the macroscopic carrier lifetime measurements to microscopic interface properties

3. Contribute to the optimization of deposition process in two different reactor systems, in order to tailor the deposition parameters to improve the passivation quality. This is a core activity of the Department for Solar Energy at Institute for Energy Technology.

4. Give a detailed analysis of the possibilities and difficulties related to electrical characterization of a-SiN$_x$:H for photovoltaic applications

1 Introduction

2 Theory

In this chapter, basic theory related to passivation of silicon using a-SiN$_x$:H and electrical characterization is described. Because the goal of passivation is to reduce recombination of carriers, the mechanisms of recombination and the effect of recombination on solar cell performance are described in Section 2.1. Then a description of the two contributing mechanisms to surface passivation of silicon is given in Section 1.1. As electrical characterization of a-SiN$_x$:H is central in this work, a brief summary of Metal-Insulator-Semiconductor capacitor theory is included in Section 2.2. Section 1.1 gives background information about a-SiN$_x$:H thin films, including properties and previous work done in this field. Due to the large impact of leakage currents on electrical characterization of a-SiN$_x$:H, an overview of carrier transport mechanisms in a-SiN$_x$:H is given in Section 1.1.

2.1   Recombination in silicon

Recombination is the process where an excited electron from the conduction band recombines with a hole in the valence band, releasing the absorbed energy [4]. Recombination losses have to be minimized in order to make high efficiency solar cells. When charge carriers recombine before they reach the external circuit, current is lost and the efficiency of the cell is reduced.

In a semiconductor under illumination, the excess electron concentration is given by

$$\Delta n \equiv n - n_0$$

(1)

where n is the total electron concentration and n_0 the thermal equilibrium concentration. Equivalently, for holes the excess concentration is given by

$$\Delta p \equiv p - p_0 \, .$$

(2)

The excess carrier concentration is also referred to as the injection level of the semiconductor, and depends on illumination. High intensity illumination with photon energies larger than the semiconductor band gap excites a large number of electrons, leading to a high injection level. Equivalently, low intensity illumination causes a low injection level.

Minority carrier lifetime τ is the average time before minority carrier recombination, and in p-type silicon it is defined as

$$\tau \equiv \frac{\Delta n}{U}$$

(3)

where U is the net recombination rate. The effective carrier lifetime, τ_{eff} is the lifetime measured experimentally, and is composed of the bulk and surface lifetimes according to the relation

$$\frac{1}{\tau_{eff}} = \frac{1}{\tau_{bulk}} + \frac{1}{\tau_{surf}}.$$

(4)

2.1.1 Bulk recombination

There are three main bulk recombination mechanisms in silicon: Radiative recombination, Auger recombination and recombination via defects. The three mechanisms are illustrated in Figure 2.

Radiative recombination is in principle the opposite process of excitation. An electron recombines with a hole, and a photon with energy equal to the band gap is emitted, as shown in Figure 2a. Silicon is an indirect semiconductor, hence absorption or emission of a phonon is necessary for radiative recombination to occur.

Auger recombination is a process where the energy from recombination of one electron-hole pair increases the kinetic energy of another excited electron, see Figure 2b. The second electron is relaxed again by emitting phonons.

Radiative and Auger recombination are fundamental processes of intrinsic silicon, independent of material quality. In contrast, recombination via defect energy levels (Figure 2c) is highly dependent of composition and structure. Impurities and defects may introduce energy levels in the semiconductor band gap, called trap states or defect levels. Charge carriers might get trapped in these states, and either be reexcited or recombine. This type of recombination is described by Shockley-Read-Hall (SRH) theory, also referred to as SRH recombination.

Bulk lifetime is given by the individual lifetimes of the three recombination mechanisms, according to the relation

$$\frac{1}{\tau_{bulk}} = \frac{1}{\tau_{rad}} + \frac{1}{\tau_{Auger}} + \frac{1}{\tau_{defect}}.$$
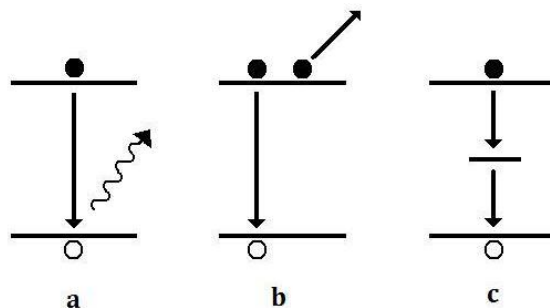
(5)

Figure 2: **Recombination mechanisms in bulk silicon. a) Radiative recombination, b) Auger recombination and c) recombination via defect energy level.**

2.1.2 Surface recombination

At the surface of silicon, there is a density of unsaturated bonds, often referred to as «dangling» bonds. These may introduce energy levels within the band gap of the semiconductor. In addition to dangling bonds, surface states can result from dislocations, or chemical residues and metallic depositions on the surface [4]. Surface recombination via defect levels is described by SRH theory, and the recombination rate at the surface is given by

$$U_s = \frac{n_s p_s - n_i^2}{\dfrac{n_s + n_{st}}{S_{p0}} + \dfrac{p_s + p_{st}}{S_{n0}}} \tag{6}$$

where n_s and p_s are the concentrations of electrons and holes at the surface. S_{n0} and S_{p0} are the surface recombination velocity parameters for electrons and holes, defined by

$$S_{n0} \equiv \sigma_n v_{th} N_{st} \; , \qquad\qquad S_{p0} \equiv \sigma_p v_{th} N_{st}. \tag{7}$$

respectively, where σ_n and σ_p are the corresponding carrier capture cross sections, v_{th} is the thermal velocity of the carriers and N_{st} is the density of surface states. When considering surface recombination, the surface recombination velocity (SRV) S is commonly used instead of the lifetime τ_{surf}. It corresponds to the inverse carrier lifetime and is defined as

$$S \equiv \frac{U_s}{\Delta n_s} \tag{8}$$

where U_s is the surface recombination rate with units of cm^{-2}s^{-1} and Δn_s is the excess minority carrier density at the surface. Assuming a known bulk lifetime and equal surface recombination velocity on both sides of the silicon wafer, the effective SRV, S_{eff}, can be estimated from the measured effective lifetime, according to the approximate relation

$$\frac{1}{\tau_{eff}} \approx \frac{1}{\tau_{bulk}} + \frac{2 S_{eff}}{W} \tag{9}$$

for small values of S_{eff} [4]. Here, W is the wafer thickness. However, if S_{eff} is large, the recombination process is limited by the diffusion of carriers to the surfaces:

$$\frac{1}{\tau_{eff}} \approx \frac{1}{\tau_{bulk}} + \frac{D_n \pi^2}{W^2} \tag{10}$$

where D_n is the diffusion coefficient of electrons [4].

2.1.3   Effect of surface recombination on solar cell efficiency

Surface recombination affects solar cell efficiency, especially for high efficiency cells made with high quality silicon. The effect of surface recombination velocity and bulk lifetime on cell efficiency is shown in Figure 3. The graph was obtained by simulations performed in the solar cell modeling program PC1D. Surface recombination velocity was varied from 1 to 10^6 cm/s, for bulk lifetimes between 1 µs and 10 ms. An idealized solar cell model was used, consisting of an *n*-type emitter on *p*-type silicon substrate. Shunting, electrical losses, front and rear reflection were neglected. Surface recombination velocities were assumed equal for the front and rear surfaces. A summary of the cell parameters are given in Table 1.

Table 1:   Specifications of idealized solar cell model used in PC1D simulation.

Cell parameter	Specification
Thickness	300 µm
Dielectric constant	11.9
Band gap	1.124 eV
Intrinsic carrier concentration at 300 K	1×10^{10} cm^{-3}
Refractive index	3.58
p-type doping level	1.513×10^{16} cm^{-3}
n-type doping level	1.579×10^{18} cm^{-3}
Emitter doping distribution	Complementary error function, $\mathrm{erfc(z)} = 1 - \mathrm{erf(z)}$
Temperature	300 K
Light intensity	0.1 W cm^{-2}
Spectrum	Reference Solar Spectral Irradiance for Air Mass 1.5

As expected, highest efficiency is obtained for high bulk lifetime and cell efficiency increases as the surface recombination velocity decreases. For poor bulk lifetimes, the efficiency saturates below 10^3 cm/s, due to small diffusion lengths in bulk. As bulk lifetimes increase, saturation is shifted towards smaller surface recombination velocities. Diffusion lengths in bulk are no longer limiting cell efficiency, hence surface passivation is more important for high quality silicon with high bulk lifetimes.
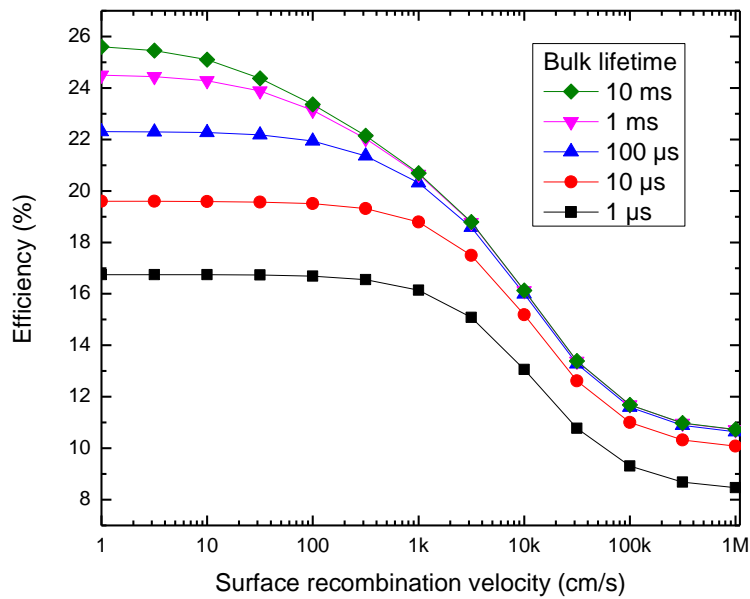
Figure 3:   Efficiency as a function of surface recombination velocity for a variety of bulk lifetimes. The graph is obtained by PC1D simulations.

2.2   Surface passivation of silicon

Generally, there are two different strategies for reducing the surface recombination velocity at the silicon surface: Chemical passivation and field-effect passivation. Both effects are present in a-SiN$_x$:H, and a description of both is given below.

2.2.1   Chemical passivation

Chemical passivation reduces the SRH recombination rate by lowering the density of interface traps, D_{it}. This can be done by deposition of a passivating film on the surface, saturating the dangling bonds. Silicon oxide and silicon nitride are the most common materials used, as both give long term stability required for solar cells. In a-SiN$_x$:H films, chemical passivation is obtained by chemical bonding of silicon, nitrogen and hydrogen atoms to surface silicon atoms, as illustrated in Figure 4.
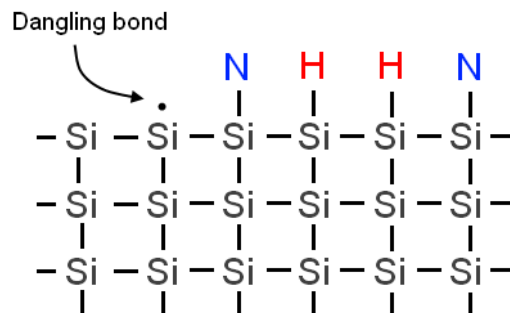
Figure 4:   Illustration of silicon surface with unpassivated dangling bond and silicon surface atoms chemically passivated by nitrogen and hydrogen atoms.

9

2.2.2 Field effect passivation

For surface recombination to occur there must be both electrons and holes present. Plotting the surface recombination rate from equation 6 as a function of the ratio of carrier concentrations shows that the recombination rate is largest when the carrier concentrations of holes and electrons are in the same order of magnitude. For a mid-gap surface trap with equal surface recombination velocity parameters for electrons and holes, the maximum recombination rate is observed for $n = p$, as shown in Figure 5. The recombination rate drops rapidly if the concentration of one carrier type is decreased. One way of reducing the carrier concentration is by introducing an electric field. Dielectric thin films with fixed electrostatic charges will repel one type of carriers, depending on the polarity of the film. This method for reducing the SRV is referred to as field-effect passivation, and is illustrated in Figure 6.

A different approach for obtaining an electric field is by implementing a doping profile in the silicon, i.e. by creating a p^+p or n^+n high-low junction. This method is commonly used when making the back surface field at the rear side of crystalline silicon solar cells.

Figure 5: **Surface recombination rate as a function of the carrier concentration ratio, for a mid-gap surface trap with equal surface recombination velocity parameters for electrons and holes.**

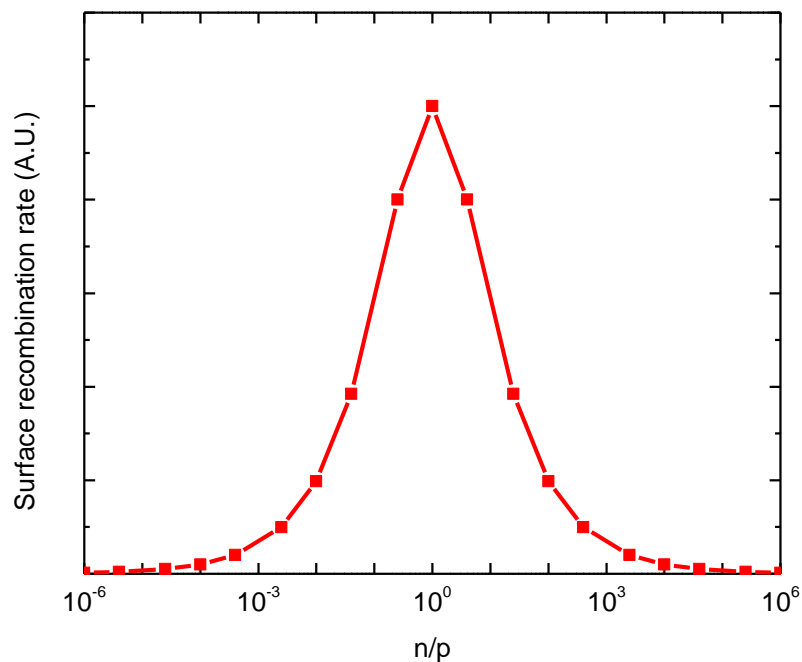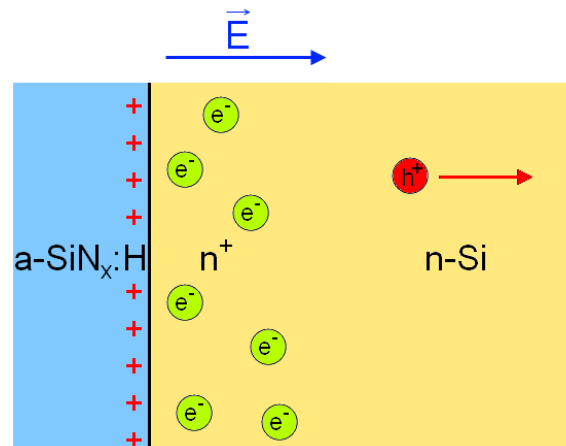**Figure 6:**   **Field effect passivation by a-SiN$_x$:H dielectric film with fixed positive charges on _n_-type silicon substrate. Accumulation of electrons creates an electric field, repelling holes.**

The field-effect passivation depends on the polarity of the fixed charges in the thin film and on the doping of the semiconductor. Silicon nitride contains positive charges fixated near the insulator/semiconductor interface. For _n_-type silicon, majority carriers will _accumulate_ at the interface, causing the bands to bend downwards [25], as is illustrated in Figure 7 (a). An _n$^+$n_ region is formed, in which minority carriers are repelled, and the total recombination velocity is decreased.

Depositing a passivation layer with fixed positive charges on _p_-type silicon introduces field effects depending on the charge density. Small densities of fixed charges repel majority carriers, giving a _depletion_ region at the interface, shown in Figure 7 (b). Depletion does not cause large enough difference in carrier concentrations to achieve good field effect passivation.

Films with a larger concentration of fixed charges will result in stronger band bending. If the intrinsic level E_i bends below the Fermi level E_f, the semiconductor is _inverted_, and switched from _p_ to _n_-type in the interface region, as illustrated in Figure 7(c). The _n_-region is separated from the _p_-region by a depletion region.

The polarity and density of fixed charges, Q_f, determine the direction and strength of the electric field and hence the extent of field effect passivation. Accumulation or strong inversion is desirable from a passivation point of view, due to a decreased recombination rate.

Figure 7: **Band diagrams of doped silicon with positively charged silicon nitride: (a)** *n*-**doped silicon with electron accumulation, (b)** *p*-**doped silicon with hole depletion, (c)** *p*-**doped sili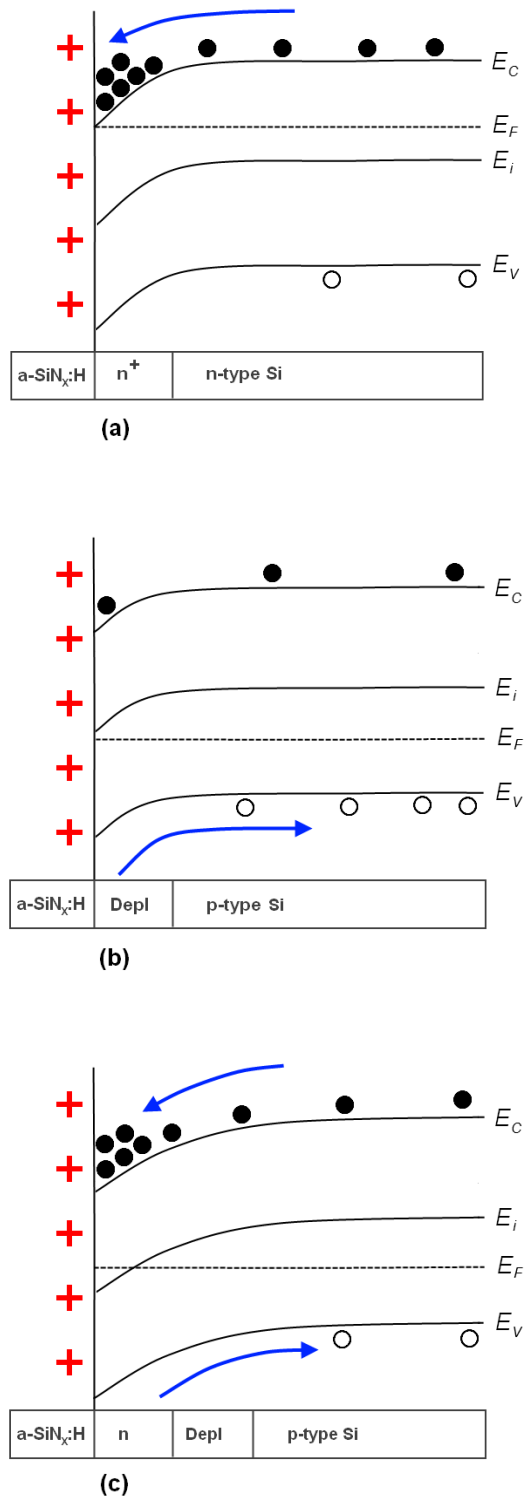con with inversion layer at the semiconductor surface.** E_C **and** E_V **are the conduction and valence band edges,** E_i **is the intrinsic energy level, and** E_F **is the Fermi level.**

2.3 Metal-Insulator-Semiconductor (MIS) theory

This section deals with the application of traditional semiconductor electrical characterization to silicon nitride for photovoltaic applications. Capacitance and conductance measurements can be used in order to characterize the passivating properties of the silicon nitride film. This yields information about the charges in the material, and the fixed charge density Q_f responsible for field effect passivation can be estimated. The density of interface traps between nitride and silicon D_{it} can found by conductance measurements. In this section an overview of the topic is given, and a general description can be found in semiconductor device textbooks, e.g. Streetman and Banerjee [25], whereas Nicollian and Brews give a more detailed guide to the topic [26].

By depositing an aluminium contact on top of the silicon nitride, a Metal-Insulator-Semiconductor (MIS) capacitor is formed, as illustrated in Figure 8. This structure can be electrically characterized by measuring the capacitance and conductance as a function of applied voltage. Electrical characterization gives information about the charge distributions and interface properties of the semiconductor/insulator system. The most important charge type is the positive fixed charges, contributing to field effect passivation. In addition, the film also possesses mobile ions, trapped electrons/holes or charges occupying interface states. Hence the total charge density of the film is given by the sum of charge types [10]:

$$Q_i = Q_f + Q_m + Q_t + Q_{it} \, .$$

(11)

Here Q_f are the fixed, Q_m the mobile, Q_t the trapped and Q_{it} the interface trapped charge densities.

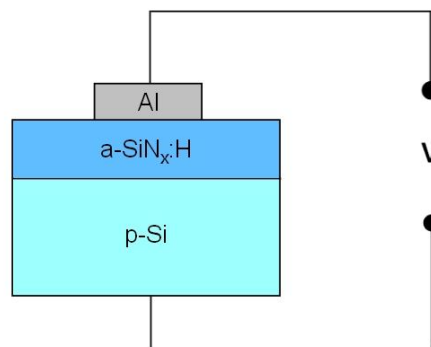**Figure 8:** Device structure of a Metal-Insulator-Semiconductor (MIS) capacitor. The semiconductor substrate is made of silicon, with an insulating amorphous silicon nitride film and aluminium contacts.

2.3.1 Capacitance of MIS structures

The MIS structure is a parallel plate capacitor where the two plates are formed by the metal and the semiconductor, and the nitride prevents current from flowing between them. The

capacitance of the parallel plate capacitor, *C*, is the material's ability to hold an electric charge, and is defined as

$$C = \frac{\mathrm{d}Q}{\mathrm{d}V} = \frac{\epsilon_r \epsilon_0 A}{d} \tag{12}$$

where *Q* is charge, *V* is the applied voltage, ϵ_r is the relative permittivity or dielectric constant of the insulator, ϵ_0 is the permittivity in vacuum, *A* is the area of the capacitor and *d* is the distance between capacitor plates. For the MIS structure, the total capacitance C_{tot} is given by the series connection of the constant capacitance of the insulator C_i and the voltage dependent capacitance of the semiconductor space charge region C_s *(V)* [4]:

$$C_{tot}(V) = \frac{C_i C_s(V)}{C_i + C_s(V)}. \tag{13}$$

The ideal MIS capacitor

In order to analyze C-V curves from real systems, it is useful to compare with an idealized case. For an ideal MIS structure, some assumptions are made in order to simplify the calculations. The work functions of the semiconductor and metal are assumed to be equal ($\phi_m = \phi_s$), there are no interface states between insulator and semiconductor ($D_{it} = 0$), and no charge in the insulating layer ($Q_i = 0$)[4].

The C-V curve for an ideal *p*-type MIS capacitor is given in Figure 9. Applying a large negative voltage will cause accumulation of electrons in the semiconductor surface, minimizing the distance between charges in the semiconductor and the insulator. Hence the semiconductor capacitance is large and the total capacitance approaches C_i (see point 1 in Figure 9).

Increasing the voltage will drive the semiconductor from accumulation via flat band (point 2) to depletion for small positive voltages (point 3). The width of the depletion region increases, and the semiconductor capacitance in depletion C_d decreases.
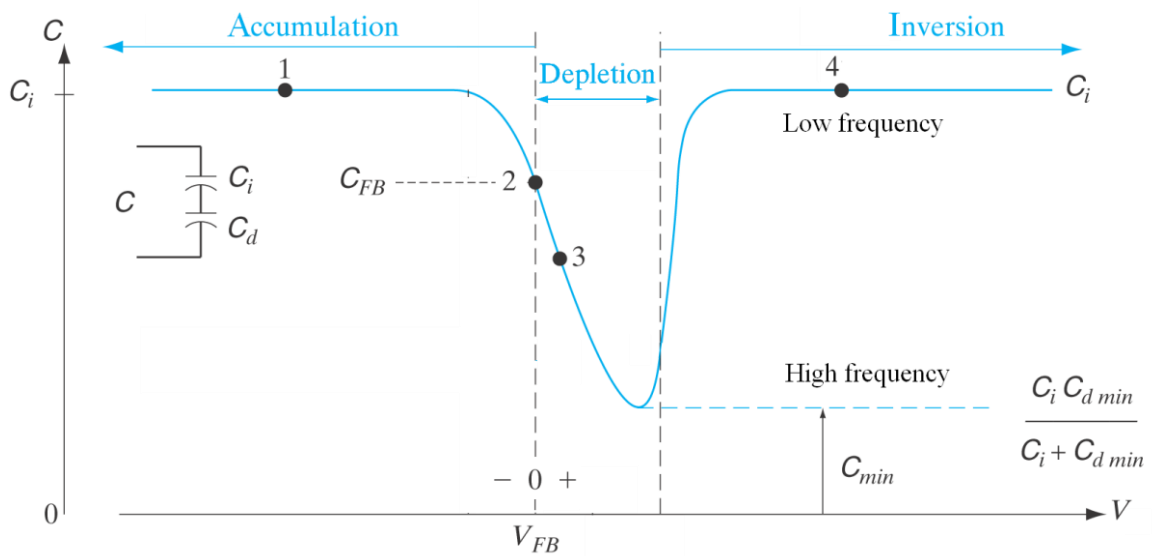
Figure 9: Capacitance – Voltage curve for a *p*-type MIS capacitor in quasi-static or low frequency mode. The dashed curve in inversion is characteristic for high frequency measurements. In depletion, the semiconductor capacitance is denoted as C_d. Figure taken from ref. [25] and modified.

An additional voltage increase will cause inversion in the semiconductor. In inversion, the frequency of the applied voltage becomes important. Frequencies are «high» or «low» compared to the generation and recombination rates in the inversion layer [25]. In high frequency measurements the AC signal is typically ~1MHz, and the amplitude is normally in the range 10—30 mV. The rapid variation of the voltage is too fast for the charges in the inversion layer to follow; hence they do not contribute to the total capacitance. In strong inversion, high frequency measurements give a non-voltage dependent capacitance minimum, illustrated by the dashed curve in Figure 9. The minimized semiconductor capacitance corresponds to the maximum extent of the depletion zone. For low frequencies, between 1 and 100 Hz, minority carriers have time to compensate for the applied electric field, giving a narrower depletion region and a higher semiconductor capacitance in inversion as compared to the high frequency response. Once again, C_{tot} approaches C_i, as indicated by point 4 in Figure 9.

Non-ideal MIS capacitor

The assumptions made for an ideal MIS capacitor are generally not valid for real devices. Work functions of metal and semiconductor are not necessarily equal, as the semiconductor work function depends on the doping level. Silicon has an electron affinity of 4.05 eV, and with a doping level of 4.5×10^{15} cm^{-3} for a p-type substrate, the semiconductor work function is $\phi_s = 4.97$ eV. For a top electrode made from aluminium, which has a work function of $\phi_m = 4.10$ eV, the work function difference is $\Delta\phi_{ms} = -0.87$ eV.

Neither Q_i nor D_{it} can be neglected in physical device and the non-ideal effects will influence C-V measurements. Flat bands are obtained when the applied voltage compensates for the difference in work functions, $\Delta\phi_{ms}$, and insulator charges Q_i. The flat band voltage is given by

$$V_{FB} = \Delta\phi_{ms} - \frac{Q_i}{C_i} \qquad (14)$$

where C_i is the insulator capacitance. The shift in flat band voltage, relative to the ideal case will cause the ideal C-V curve to shift parallel to the voltage axis, as illustrated in Figure 10.

By extracting the flat band potential from the C-V curve, the insulator charge density can be determined. At flat band conditions, the semiconductor capacitance is assumed to be determined by the Debye length λ_D according to the equations

$$\lambda_D = \sqrt{\frac{\epsilon_{Si} kT}{q^2 N_A}} \qquad (15)$$

and

$$C_s = \frac{\epsilon_{Si} \epsilon_0 A}{\lambda_D} \qquad (16)$$

where $\epsilon_{Si} = 11.68$ is the relative permittivity of silicon and N_A is the doping concentration [24]. The flatband capacitance can be estimated from equation 16.

Assuming no mobile or interface charges, $Q_i = Q_f$, the fixed charge density can be calculated from [24]

$$Q_f = \frac{C_i}{Aq}(\Delta\phi_{ms} - V_{fb}). \qquad (17)$$

The density of interface traps can be extracted from combined high frequency and quasi- static measurements. As the bias is varied, the Fermi level at the semiconductor surface changes. Electrons or holes will occupy trap states depending on whether the trap is positioned below or above the Fermi level, respectively. The trap state capacitance contributes to the low frequency capacitance, but the charge/discharge process is too slow to contribute at high frequencies. This leads to a split in the C-V curve at minimum capacitance, as shown in Figure 10. The density of interface traps is given by the relation

$$D_{it} = \frac{1}{q} \left(\frac{C_i C_{lf}}{C_i - C_{lf}} - \frac{C_i C_{hf}}{C_i - C_{hf}} \right) \tag{18}$$

where q is the elementary charge, C_i is the insulator capacitance, and C_{lf} and C_{hf} are the low and high frequency capacitances at the minimum, respectively [25].
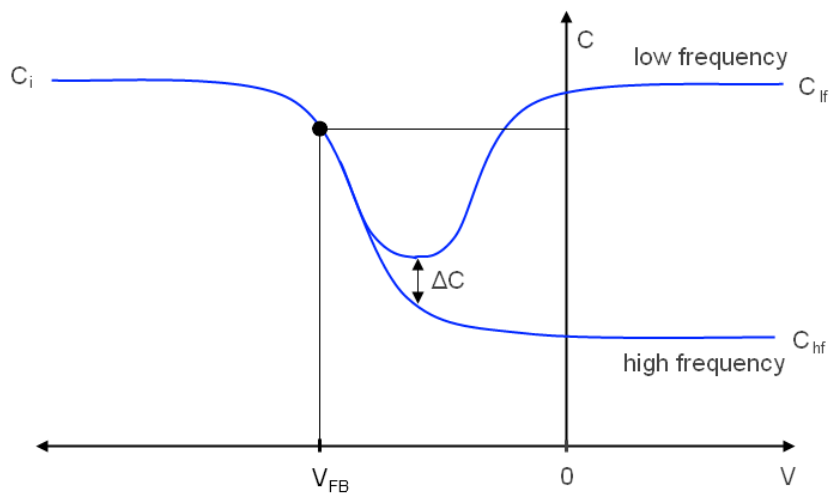

Figure 10: C-V curve of non-ideal MIS capacitor. The curve is shifted to the left, giving a negative flat band voltage due to positive charges in the insulator. The shift *ΔC* between low and high frequency curves is caused by interface traps.

2.3.2   Conductance of MIS structures

The conductance method is an alternative method to quasi-static C-V measurements for determining the density of interface traps [27]. Measurements are performed on MIS capacitor structures using the same experimental setup as for C-V measurements. The conductance G is defined as the inverse of resistance R, or as a function of conductivity σ according to

$$G = \frac{1}{R} = \frac{\sigma A}{d} \tag{19}$$

where A is the area of the capacitor and d is the distance between capacitor plates. Capture and emission of carriers in the traps increase the AC-conductivity of the structure; hence conductance is a measure of the density of interface traps [27].

The equivalent circuit of a MIS capacitor with interface trap states is given in Figure 11 (a), representing the interface trap states as a series connection of a capacitance C_i and a resistance R_{it}. The interface trap time constant is given by $\tau_{it} = C_{it}R_{it}$. This circuit can be simplified by introducing a parallel connection of a conductance G_P and a capacitance C_P, as shown in Figure 11 (b), where G_P and C_P are given by [27]

$$C_P = C_S + \frac{C_{it}}{1 + (\omega\tau_{it})^2} \tag{20}$$

and

$$\frac{G_P}{\omega} = \frac{q\omega\tau_{it}D_{it}}{1 + (\omega\tau_{it})^2}. \tag{21}$$

Here ω is the angular frequency determined from the measurement frequency by $\omega = 2\pi f$, C_S is the semiconductor capacitance. The interface trap capacitance is related to the density of interface traps according to $C_{it} = q^2 D_{it}$. This model pertains to a single mid-gap trap state, and for a continuum of trap states equation 21 modifies to [27]

$$\frac{G_P}{\omega} = \frac{qD_{it}}{2\omega\tau_{it}} \ln[1 + (\omega\tau_{it})^2]. \tag{22}$$

Experimentally, D_{it} is found by applying a voltage to keep the semiconductor in depletion and measuring the equivalent parallel conductance G_P as a function of frequency. Plotting G_P/ω versus frequency gives a curve with a maximum value $(G_P/\omega)_{max}$, as illustrated in Figure 12. D_{it} can then be estimated from the relation [26]

$$D_{it} = \frac{2.5}{qA} \left(\frac{G_P}{\omega}\right)_{max}. \tag{23}$$
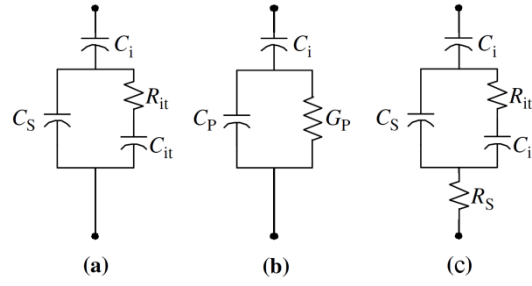
Figure 11: Equivalent circuits of the MIS structure for conductance measurements: (a) C_i is the insulator capacitance, C_s the semiconductor capacitance, C_{it} the capacitance of interface traps and R_{it} the interface trap resistance. (b) is the simplified circuit of (a) where C_P and G_P are the equivalent parallel capacitance and conductance, respectively. (c) is the circuit from (a) with an additional series resistance R_S. The figure is taken from [27] and modified.
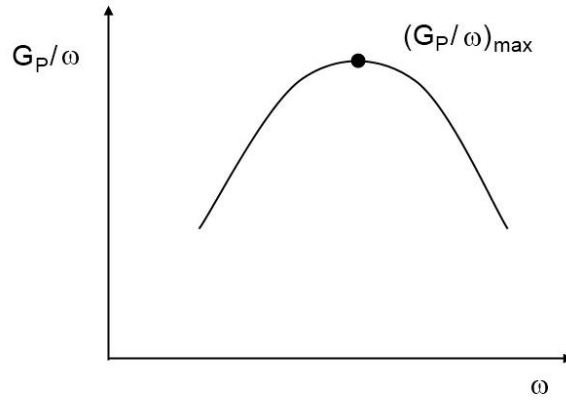
Figure 12: Sketch showing a typical G_P /ω vs. ω curve obtained by conductance-frequency measurements. The maximum is related to D_{it} through equation 23.

Alternatively, the peak conductance can be extracted from conductance-voltage plots, as described by Nicollian and Brews [26]. The peak conductance in the depletion region originates from the increased conductance from interface states. By correcting for series resistance, the magnitude of the peak is found. In general, there are various contributions to series resistance: The contact between probe and metal, the back contact to the silicon, resistance in the silicon bulk, or contamination and non-uniformities in the doping distribution [26]. An equivalent circuit including series resistance is given in Figure 11 (c), and an expression for R_S can be found from the relation

$$R_S = \frac{G_a}{G_a^2 + \omega^2 C_a^2} \tag{24}$$

where G_a and C_a are the measured conductance and capacitance in accumulation, respectively [26]. The voltage dependent conductance and capacitance corrected for series resistance are given by the formulas

$$G_C = \frac{(G_P^2 + \omega^2 C_P^2)a}{a^2 + \omega^2 C_P^2} \tag{25}$$

and

$$C_C = \frac{(G_P^2 + \omega^2 C_P^2)C_P}{a^2 + \omega^2 C_P^2} \tag{26}$$

where

$$a = G_P - (G_P^2 + \omega^2 C_P^2)R_S \tag{27}$$

and G and C are the measured conductance and capacitance, respectively [26]. The series resistance component of the conductance, G_R, is given by [26]

$$G_R = \frac{\omega^2 C_C^2 R_S}{1 + \omega^2 R_S^2 C_C^2}. \tag{28}$$

Figure 13a illustrates the measured conductance, the contribution from series resistance and the corrected curves. The maximum conductance on the corrected curve can be used to calculate D_{it} using equation 23. This method is referred to as the analytical method for series resistance correction. An alternative approach to finding the height of the conductance peak is to perform a simple linear interpolation, as illustrated in Figure 13b.

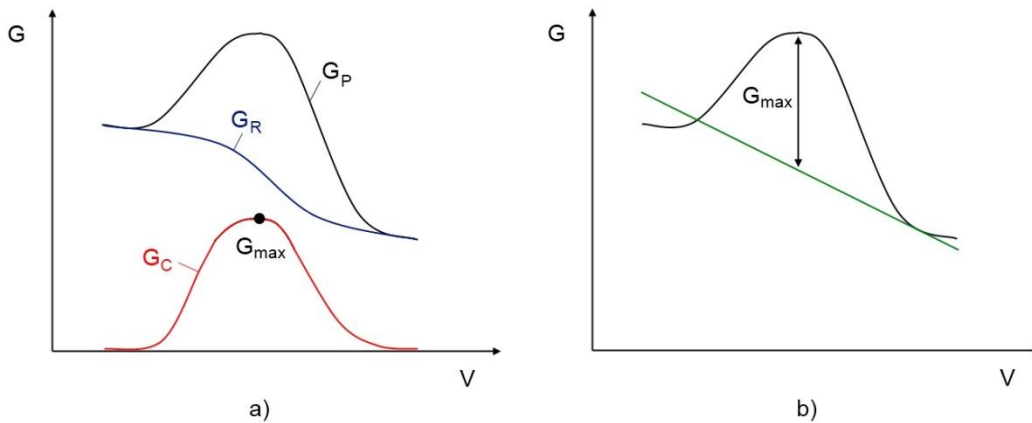**Figure 13:** **Methods for series resistance correction on G-V measurements: a) Analytical method using equations 24—28. G_P is the measured conductance, G_R the series resistance contribution to the conductance and G_C the obtained corrected curve. G_{max} is used to determine D_{it}. b) Linear interpolation method for series resistance corrected determination of D_{it}.**

2.4   Amorphous hydrogenated silicon nitride (a-SiN$_x$:H)

In this section, the properties of a-SiN$_x$:H surface passivation layers for photovoltaic applications are presented. Large effort has been put into understanding the passivation properties of a-SiN$_x$:H, and optimizing the fabrication processes in order to improve the passivation quality, and a brief overview of previous work in the field is given here.

2.4.1   Effective lifetime and surface recombination velocity

The measured effective lifetime and estimated surface recombination velocity are macroscopic measures of the average passivation quality. Naturally, a low surface recombination velocity is reflected in a high measured lifetime. For unpassivated silicon wafers, surface recombination is limiting lifetime measurements. As a lower limit of passivation quality, the transport of carriers to the surface region is rate determining. By inserting a diffusivity of approximately 30 cm/s into equation 10, and assuming a high bulk lifetime of 1 ms, a minimum value of the measured effective lifetime of 3 µs is found. Lifetime analysis of PECVD a-SiN$_x$:H show that excellent passivation can be achieved. Lifetimes in the ms range can be obtained [4], corresponding to surface recombination velocities around ~10 cm/s for high quality silicon.

2.4.2   Fixed charges and interface traps

As previously mentioned, the surface passivation is influenced by the properties of the interface between silicon and the passivation layer. The band structure of an a-SiN$_x$:H film on *p*-type silicon with zero applied bias is illustrated in Figure 14. Here, the surface is in inversion due to the distribution or positive charges within the film, Q_f. The density of interface traps, D_{it}, is indicated by defect levels in the silicon band gap. For an unpassivated silicon wafer, D_{it} is approximately 10^{13} cm^{-2} eV^{-1} [4]. For plasma a-SiN$_x$:H passivated wafers, D_{it} values between 1×10^{11}—5×10^{12} cm^{-2} eV^{-1} are reported [4].

At the interface between silicon and a-SiN$_x$:H, there is a thin layer of SiO$_x$ originating from oxidation in the period after the HF dip to before the start of a-SiN$_x$:H deposition [4]. This film is converted to an interfacial oxynitride SiO$_x$N$_y$ film during deposition, and exhibits positively charged defects contributing to Q_f.

The origin of the fixed positive charges are believed to be the *K centers,* which are the dominating defects in a-SiN$_x$:H. A K center consists of a silicon atom, with one unpaired electron, bonded to three nitrogen atoms ($N_3 \equiv Si \cdot$) [4], and this state is referred to as the neutral K^0 state [16]. The unpaired electrons can be donated to the silicon, leaving the positively charged K$^+$ centers characteristic for a-SiN$_x$:H, according to the mechanism:

$$K^0 \rightarrow K^+ + e^-. \tag{29}$$

Elmiger and Kunst determined the depth of K^+ centers in the silicon nitride film to 20 nm, by measuring the increase in conductivity due to transfer of electrons into the silicon with an increasing Q_f [28]. Similarly, negatively charged defects can be obtained by trapping of two electrons [16]:

$$K^+ + 2e^- \rightarrow K^-. \tag{30}$$

However, other possible configurations of positively charged defects are suggested as well. De Wolf proposed a model were the definition of K centers is generalized to consisting of silicon atoms bonded to either nitrogen or silicon: $Si_{3-y}N_y \equiv Si \cdot$, where y is 1, 2 or 3 [29].
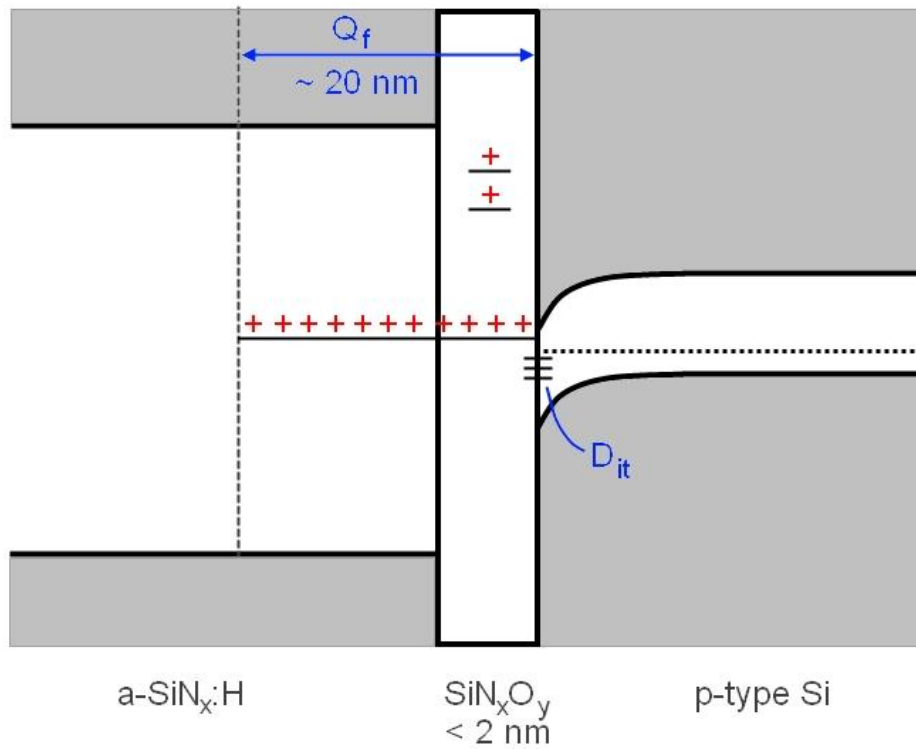

Figure 14: **Approximate band structure of a-SiN$_x$:H thin film on *p*-type silicon substrate, with an nitride/oxide intermix layer in between. The silicon surface is in inversion, due to band bending caused by fixed charges (K$^+$ centers) in the a-SiN$_x$:H layer. Interface traps are present between the semiconductor and intermix layer.**

C-V measurements confirm the presence of positive charges, and values in the range 1×10^{11}—5×10^{12} elementary charges per cm^2 have been reported [4]. A well-known challenge with C-V measurements, however, is that the thin films are affected by the measurements. The charge of K centers can be altered by applying a bias, causing trapping and emission of charge carriers, resulting in a varying Q_f and hysteresis effects in C-V measurements [4]. Beylier et al. describe these hysteresis effects and additionally observe shifts in flat band voltage with applied bias [16]. Increasing negative bias led to larger quantities of positive charges, and positive bias resulted in a formation of negatively charged states in the a-SiN$_x$:H thin film [16]. Another characteristic of the C-V behavior of a-SiN$_x$:H MIS structures described by Beylier et al. is an increasing inversion capacitance with decreasing frequency of the applied signal. This is explained by the positive charges in the a-SiN$_x$:H layer creating a permanent inversion layer. The inversion layer electrons act as a reservoir of carriers compensating for the applied bias at lower frequencies, leading to an increasing capacitance [15].

2.4.3   Chemical composition and optical properties

The chemical composition and refractive index in a-SiN$_x$:H are interlinked, and hence measuring the refractive index gives an indication of the stoichiometry of the sample. By controlling the deposition conditions, a-SiN$_x$:H films with varying [N]/[Si]-ratio, *x*, can be obtained. Normally, amorphous silicon nitride has *x*-values ranging from *x* = 0 for a-Si:H to *x* = 4/3 for stoichiometric silicon nitride, a-Si$_3$N$_4$:H. Makino proposed the following equation relating the refractive index to stoichiometry, neglecting contributions from hydrogen [23]:

$$n = \frac{n_{a-Si:H} + \frac{3}{4}x\left(2n_{a-Si_3N_4} - n_{a-Si:H}\right)}{1 + \frac{3}{4}x} \tag{31}$$

where $n_{a\text{-}Si:H}$ and $n_{a\text{-}Si3N4}$ are the refractive indices of amorphous silicon and stoichiometric silicon nitride, respectively. Performing a first order Taylor expansion around x = 1, gives a linear approximation indicating a decrease in refractive index with increasing nitrogen content. The refractive indices of amorphous silicon and near stoichiometric silicon nitride deposited by PECVD depend on the hydrogen content in the films. Inserting $n_{a\text{-}Si:H}$ = 3.3 and $n_{a\text{-}Si3N4}$ = 1.9, in the expressions for *n(x)* and the linear Taylor expansion result in the plot shown in Figure 15. The first order Taylor expansion is a good approximation for refractive indices in the interval 1.8—2.5. Alternatively, the Taylor expansion can be made using the ratio [Si]/[N] = 1/*x* as a variable, giving a linear approximation where the refractive index increases with increasing silicon concentration.
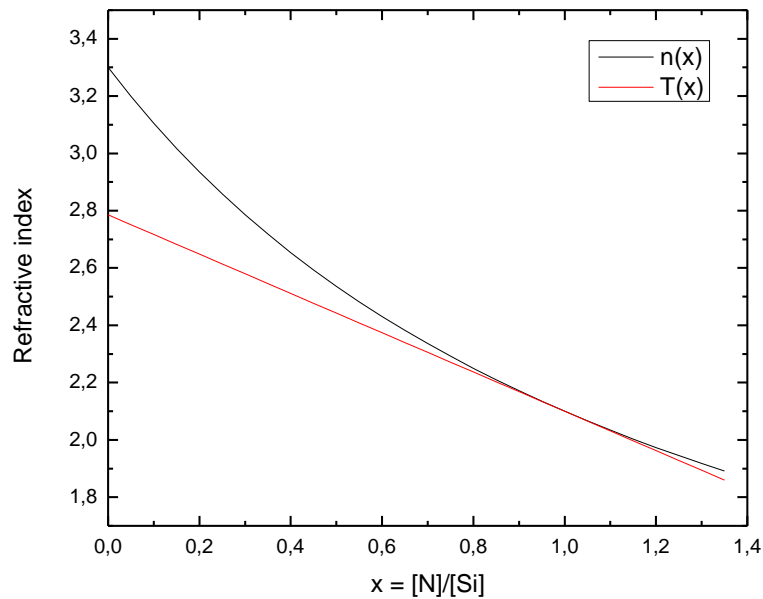
Figure 15: **Refractive index as a function of layer stoichiometry:** *n(x)* **is the formula in equation 31 proposed by Makino, and** *T(x)* **is the linear Taylor expansion around** *x* **= 1.**

The linear dependence of refractive index on layer stoichiometry has been confirmed experimentally using Rutherford back scattering (RBS) [30], X-ray photoelectron spectroscopy (XPS) [13] and Fourier transform infrared (FTIR) spectroscopy [31]. Due to different deposition methods and conditions, the hydrogen content is varying in the different studies, explaining deviations in the coefficients of the linear trends. Lauinger et al., Lelièvre et al. and De Wolf et al. report that adjusting the gas flow ratio, SiH_4 / NH_3 , results in films of varying refractive indices and stoichiometry [6, 13, 29].

Lauinger et al. have demonstrated a strong correlation between lifetime and refractive index, where higher lifetimes are obtained for refractive indices larger than 2.3, for silicon nitride films deposited in remote PECVD reactors [6]. This is confirmed by Mäckel and Lüdemann and De Wolf et al. [29, 31], where a high refractive index is achieved by adjusting the composition of the film towards high silicon content through adjustment of the gas flow ratios. However, Schmidt and Kerr found the optimum surface passivation for films with near stoichiometric composition, with a refractive index of 1.9 [7]. The results were explained by an additional flow of nitrogen in the process chamber, and the use of a remote reactor system.

The optical properties of the a-SiN$_x$:H thin film should be considered when designing the combined passivation and anti-reflection coating. The wavelength dependent reflectance of the finished solar cell should be as low as possible, and this is dependent of film thickness and refractive index [32]. Additionally, the absorption in the a-SiN$_x$:H layer should be minimized in order to avoid reducing cell efficiency. Typical values for an optimized a-SiN$_x$:H single layer ARC

are refractive index in the range 1.9—2.1 and film thicknesses around 70—85 nm, depending on surface texture and the refractive index of the surrounding media [32-34]. Hence there is a tradeoff between low index a-SiN$_x$:H with low absorption and high index a-SiN$_x$:H with high passivation quality.

Composition was also observed to affect the electric properties of a-SiN$_x$:H MIS capacitors. Beylier et al. reported decreasing hysteresis effects for increasing refractive indices from 1.95 to 2.8, as well as increased leakage currents [15]. This was explained by a reduced defect quantity with higher silicon content, and increased conductivity due to band gap narrowing. This is supported by the investigations of De Wolf et al., who found a decrease in hysteresis effects and increase in leakage currents for refractive indices increasing from 2.0 to 3.0. According to the observations of Lau et al., the width of the hysteresis loop for recorded C-V curves increased with the silicon content, for samples with Si/N ratios 0.62 and 1.05 [35]. From equation 31, this roughly corresponds to refractive indices of 1.7 and 2.2. The large hysteresis effects of silicon rich films were related to the charging of a-SiN$_x$:H, and were found to be symmetric with respect to polarity. N-rich films showed an asymmetric behavior, where positive charges were easier to induce than negative charges. Hezel and Schörner observed an increase in the concentration of positive charges with increasing gas flow ratio for films with low refractive index (1.8—1.9)[36]. De Wolf et al. reports increasing charge density for refractive index in the interval 2.0—2.7, followed by a decrease for higher refractive indices [29].

2.4.4   Stability under illumination

The thermal and UV stability of a-SiN$_x$:H for photovoltaic applications should be high. Aberle and Hezel found that a-SiN$_x$:H thin films were stable under illumination of wavelengths larger than 400 nm, and suffered from degradation when exposed to UV radiation below 400 nm [37]. The surface recombination velocity increased with decreasing film thickness and films deposited by remote PECVD were found to be more stable than films deposited by direct PECVD.

2.4.5   Effect of heat treatment

Industrially, solar cells are often contacted using screen printing after nitride deposition. Metal front contacts are formed by applying a metal paste through a patterned mask, and a heat treatment allows the metal to etch through the silicon nitride layer. This process is rapid, and temperatures of about 800 °C are reached. This heat treatment is often referred to as «firing», and it affects the properties of the a-SiN$_x$:H passivation layer.

Lelièvre et al. have investigated the effect of a rapid heat treatment up to 800 ˚C for 1 s, corresponding to the screen printing firing process, on a-SiN$_x$:H films deposited by low frequency direct PECVD [13]. A deterioration of the surface passivation quality was observed for Si-rich films (n>2.2) and lightly improved for N-rich films (n=2.0–2.1). The N-rich films were found to be denser and more thermally stable. Additionally, the improvement in effective

lifetime was explained by diffusion of atomic hydrogen into the silicon, passivating both surface and bulk defects in a chemical manner.

C-V measurements indicated Q_f values larger than 1×10^{12} cm^{-2} for all samples [13]. After a rapid thermal anneal, a decrease in Q_f was observed. This was explained by the neutralization of K$^+$ centers by diffusing hydrogen. The density of interface traps decreased after the heat treatment, due to hydrogen passivation of dangling bonds.

Similarly, in a study of films prepared by remote PECVD, Lenkeit et al. found a deterioration of the films with refractive index below 2.0 and above 2.2 after an 850 ˚C annealing step. For films with refractive index between 2.0 and 2.1, an improvement of the SRV from 20 to 4 cm/s was observed [14].

Aberle, however, states that the passivation quality degrades for both high and low frequency direct and remote plasma techniques [4]. He claims the explanation is thermally activated loss of hydrogen from the a-SiN$_x$:H films, reducing the chemical passivation from hydrogen at the interface. Degradation is strongly dependent on annealing time and temperature, and at 800 ˚C, degradation occurs after 1 min [4]. An exception of this general trend was observed for low frequency direct plasma silicon nitride, where the lifetime increased for the first minutes of the annealing time. The proposed explanation was that hydrogen passivates defects caused by ion bombardment. Aberle claims this effect occurs for low frequency direct plasma techniques only [4].

De Wolf et al. observed lower lifetimes after a firing treatment, and related the degradation to blistering [29]. Further, a decrease in Q_f after firing and no trend with respect to lifetime versus stoichiometry after the firing step were reported [29].

Hong et al. studied the effect of firing on the film properties of industrial remote PECVD silicon nitrides, and found that hydrogen was released by a high temperature treatment [38]. Depending on deposition conditions and film properties, the hydrogen can evaporate as H$_2$ or NH$_3$ or diffuse into the silicon and passivate defects. The loss of hydrogen was found to be larger for Si-rich films, and nearly absent for N-rich films.

2.5   Carrier transport in insulators

Ideally, DC leakage currents are not present in insulating thin films. However, for real devices carrier transport in the insulating layer is not negligible, and may complicate the electrical characterization of dielectric materials. Leakage currents influence measurements, and can make the data analysis more difficult. Thus, understanding the mechanisms behind the phenomena is important for electrical characterization.

2.5.1   Transport mechanisms

There are several transport mechanisms for carriers through insulating films, which are used to describe temperature dependent current–voltage (I-V) characteristics of MIS and MIM (metal-insulator-metal) structures. Three basic mechanisms are discussed here: Schottky conduction, the Poole-Frenkel effect and tunneling currents. Illustrations of the conduction processes with and without an applied voltage are shown in Figure 16. In Table 2, expressions for current as a function of applied electric field and temperature are given, together with mathematical relations for linearization [39].

Schottky transport is characterized by carriers being thermally excited into the insulator conduction band, and the barrier towards transport is reduced by an applied field [39]. The barrier height is strongly dependent on the polarity of the applied field and the work functions of the metal or semiconductor in the MIM or MIS [20, 40].

In Poole-Frenkel conduction, carriers are «hopping» between defect states in the insulator band gap, and an applied bias will reduce the barriers towards hopping [39]. This is an insulator bulk effect, and is symmetric with respect to direction of applied field and contact work functions [20, 40].

Tunneling of carriers through the insulator can be enhanced by applied fields, as shown in Figure 16, and the effect is independent of temperature [25, 39].

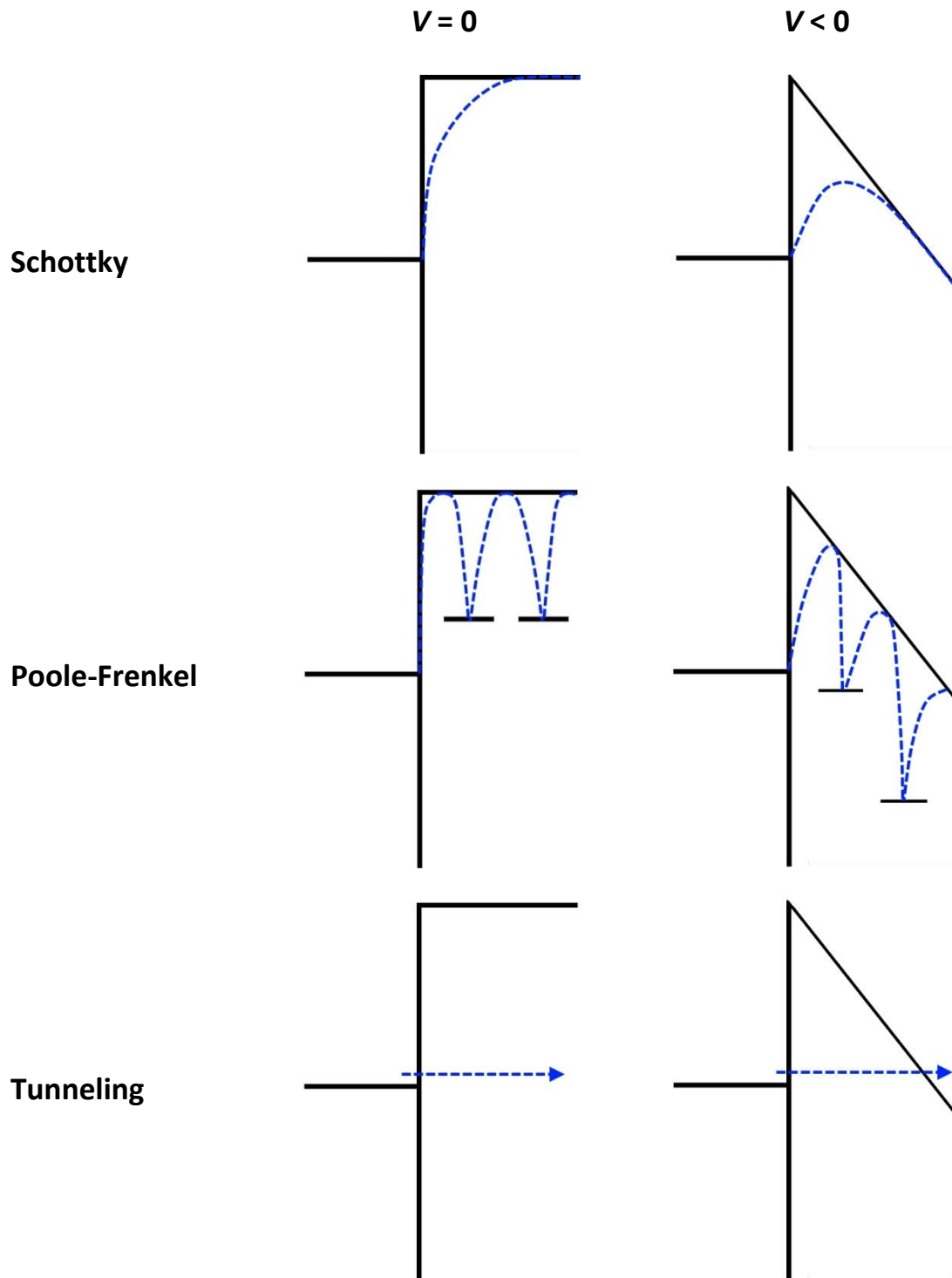**Figure 16:** **Band diagrams illustrating Schottky, Poole-Frenkel and tunneling transport in insulators. Electron transport paths from the metal Fermi level or semiconductor conduction band through the insulator conduction band are shown, for no bias and negative bias applied to the metal/semiconductor contact. The blue lines represent the effective barrier and the transport path of electrons.**

Table 2: Carrier transport mechanisms in insulators [39], with mathematical relations for linearization. *J* is current density, *A* is the effective Richerson constant, φ_B the barrier height, *E* the electric field related to voltage by *V = Ed* where *d* is the insulator thickness. ϵ_i is the insulator dynamic permittivity and *m** the effective mass.

Transport mechanism	Expression *J(E,T)*	Linear plot from I-V		Linear plot from I-T	
Schottky	$J = AT^2 \exp\left[\dfrac{-q\left(\phi_B - \sqrt{qE/4\pi\epsilon_i}\right)}{kT}\right]$	$\ln(I)$	$V^{1/2}$	$\ln(I/V)$	$1/T$
Poole-Frenkel	$J \sim E \exp\left[\dfrac{-q\left(\phi_B - \sqrt{qE/\pi\epsilon_i}\right)}{kT}\right]$	$\ln(I/V)$	$V^{1/2}$	$\ln(I)$	$1/T$
Tunneling	$J \sim E^2 \exp\left[-\dfrac{4\sqrt{2m^*(q\phi_B)^3}}{3q\hbar E}\right]$	$\ln(I/V^2)$	$1/V$	*I* independent of *T*	

2.5.2 Leakage currents in amorphous silicon nitride

The conduction mechanism in a-SiN$_x$:H has been investigated by Sze [20], Maeda and Arita [22], Lowe et al. [21], Sinha and Smith [19] and Jeon et al. [18]. They all find the leakage current to be largely dependent on temperature, and suggest the Poole-Frenkel mechanism to be dominating. However, Jeon et al. include contributions from tunneling for lower fields [18], and Sinha and Smith report tunneling for temperatures over 60 °C [19]. Yeargan and Taylor argue that the Schottky and Pool-Frenkel effects cannot be separated by the occurrence of straight line plots as described in Table 2, because linearity is observed for both [40]. According to Sze, the two mechanisms can be separated by looking at symmetry of the measurement polarity, as the Poole-Frenkel mechanism is bulk limited and hence symmetric with respect to measurement polarity, whereas the Schottky effect is an interface effect and strongly influenced by the polarity of the applied bias [20]. Measurements on a-SiN$_x$:H were observed to be symmetric by Lowe and Arita [21], Yeargan and Taylor [40] and Sze [20], indicating presence of the Poole-Frenkel effect. Barrier heights in the range 0.6 —1.7 eV were found [19-22], and obtained values for the dynamic permittivity were in the range 1.8—6.5 [19, 20, 22]. The dynamic permittivity is approximately equal to the optical permittivity, which is given by the refractive index squared [41].

2 Theory

3 Experimental

3.1 Device fabrication

3.1.1 Substrate preparation

Monocrystalline *p* and *n*-type Czochralski (CZ) and *p*-type float zone (FZ) silicon wafers were used as substrates for film deposition. The wafers were boron or phosphorus doped and double side polished. In Table 3, the wafer specifications are given.

Table 3: Specifications of CZ and FZ wafers used for device fabrication.

	Czochralski *p*-type	**Czochralski *n*-type**	**Float zone *p*-type**
Supplier	Siltronix	Siltronix	Topsil
Diameter	4 inches	4 inches	4 inches
Thickness	300 ± 25 μm	300 ± 25 μm	280 ± 25 μm
Crystal orientation	[100]	[100]	[100]
Resistivity	1–3 Ωcm	1–3 Ωcm	1–5 Ωcm
Doping level	4.5×10^{15}–1.5×10^{16} cm^{-3}	1.5×10^{15}–4.5×10^{15} cm^{-3}	2.5×10^{15}–1.5×10^{16} cm^{-3}

All wafers were cleaned using standard RCA-1, RCA-2 and HF wet chemical cleaning. RCA-1 removes organic contaminants, RCA-2 removes metal contaminants and HF removes silicon oxide at the wafer surface [42]. RCA-1 consists of 5 parts DI water, 1 part NH_4OH (27 %) and 1 part H_2O_2 (30 %), while RCA-2 consists of 6 parts DI water, 1 part HCl (27 %) and 1 part H_2O_2 (30 %). The RCA-1 and RCA-2 baths were prepared by heating the NH_4OH/HCl in DI water to 70 °C before adding hydrogen peroxide. After mixing, the solution was allowed to settle for 2 minutes before use. The concentration of HF acid was 5 %. Between cleaning steps, the wafers were rinsed in DI water. An overview of the cleaning procedure is given in Table 4.

Table 4: **Wafer cleaning procedure.**

Step	Bath	Composition	Temperature	Immersion time
1	RCA-1	$NH_4OH + H_2O_2 +$ DI-water 1:1:5	70 °C	15 min
2	DI-water rinse 1		25 °C	30 sec
3	HF	5 %	25 °C	30 sec
4	RCA-2	$HCl + H_2O_2 +$ DI-water 1:1:6	70 °C	10 min
5	DI-water rinse 2		25 °C	30 sec
6	HF	5 %	25 °C	30 sec
7	DI-water rinse 3		25 °C	30 sec
8	DI-water rinse 4		25 °C	30 sec
9	Blow dry with N_2			

3.1.2 Thin film deposition by plasma enhanced chemical vapor deposition (PECVD)

a-SiN$_x$:H was-deposited on the cleaned silicon wafers by direct plasma enhanced chemical vapor deposition (PECVD), which is a common method for depositing passivation layers for photovoltaic applications. Deposition is performed at low temperature and pressure, typically below 500 °C and 1 Torr [4]. Plasma transforms precursor molecules into highly reactive radicals, ions, neutral atoms, and molecules, and the excited gas species interact with the sample forming the desired thin film.

The quality of passivation depends on film properties, such as thickness, chemical composition and refractive index. Passivation properties are sensitive to the quality of the interface between the dielectric film and the substrate, and on the concentration of fixed charges. The growth rate is also dependent of deposition parameters. A high growth rate is desirable with respect to mass production [6]. In the PECVD process, the deposition parameters can be controlled in order to tailor thin film properties. Deposition parameters include the substrate temperature, total pressure in the reactor, gas flows of different precursor gases, and the plasma energy.

A variety of different PECVD systems exist. In this work, two different PECVD chambers were used: A direct high frequency plasma reactor and a remote expanding thermal plasma (ETP) system.

Direct high frequency PECVD

For the direct high frequency plasma method, the process chamber is a parallel plate batch reactor, where the samples are placed within the plasma [4]. A schematic of the direct PECVD reactor is given in Figure 17. Samples are placed on the heated lower electrode, and precursor gases flow into the chamber through the upper electrode, also referred to as the «shower head». A radio frequency (RF) field with frequency 13.56 MHz is applied, generating plasma between the electrodes, and a vacuum pump ensures low process pressure. Precursor gases for silicon nitride deposition include silane (SiH_4), ammonia (NH_3) and nitrogen (N_2).
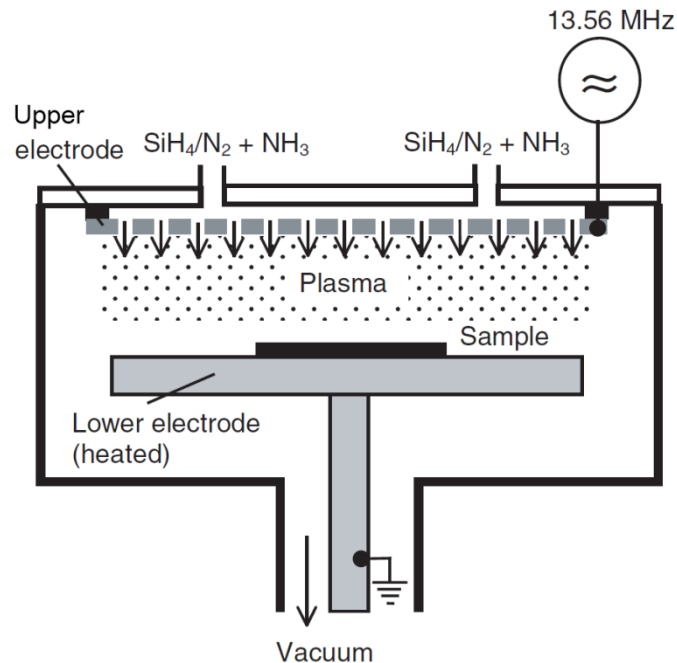

Figure 17: Illustration of the parallel plate direct PECVD reactor [8]. The wafer is placed on the lower electrode, and precursor gases flow into the reactor through the upper electrode. An RF signal of 13.56 MHz is applied to generate plasma.

In the direct PECVD process, ion bombardment can occur due to accelerated ions in the RF-field hitting the sample [4]. This may give rise to an increased density of interface states, leading to poorer passivation, or produce weaker bonds at the interface and within the a-SiN_x:H film, causing low UV stability. The impact of ion bombardment depends on plasma frequency, and is highest using low frequencies, where acceleration periods are long enough for ions to obtain the required energy [4]. At high frequencies, the problem with ion bombardment is assumed to be less significant.

The direct PECVD reactor used was a Plasmalab System 133 from Oxford Instruments. Specifications of the setup include pressures up to 2 Torr, temperatures up to 400 °C and RF power up to 500 W with a fixed frequency of 13.56 MHz and circular electrodes with a diameter of 33 cm.

Four samples, a–d, of each parameter set were deposited. Samples a and b were made for lifetime measurements; hence they had thin films deposited on both sides of the wafer. Samples c and d were for CV measurements and had a thin film on one side only. For some samples, the c samples were split into two smaller samples, where one was fired, instead of deposition on sample d. These samples are referred to as c-1 and c-2 for the as-deposited and fired version, respectively. In order to minimize the effect of possible inhomogeneity in the plasma chamber, samples were placed in the same manner for all depositions, as illustrated in Figure 18. This way, measurements performed on different samples from the same ingot will not be affected by quality differences within each wafer.
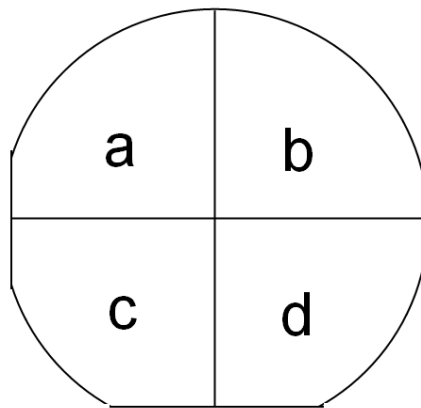

Figure 18: Sample arrangement during PECVD deposition. Samples a and b were placed closest to the load lock, and samples c and d furthest into the chamber.

A total of 45 samples were fabricated using direct PECVD. Two sets of parameter variations were performed, one varying the silane flow in order to adjust film composition and one varying the deposition time to obtain films of different thickness. For Set 1, the silane flow was varied while keeping all other deposition parameters constant, and the deposition time was adjusted to achieve uniform film thickness. A thickness variation (Set 2) was obtained by varying the deposition time while keeping all other parameters fixed. An overview of the deposition parameters is given in Table 5 and the deposition parameters for all samples are summarized in Appendix A.

An a-SiN$_x$:H/a-SiN$_x$:H stack was-deposited by adding an extra step with different gas composition to the normal deposition recipe. The stack consisted of approximately 47 nm of a high-silane-flow nitride with 43 nm of a low-silane-flow nitride on top, as described in Table 6. The approximate film thicknesses were obtained by adjusting deposition time to previously measured deposition rates.

Table 5: **Overview of deposition parameters for direct PECVD a-SiN$_x$:H, Set 1: Silane variation and Set 2: Time variation.**

Parameter	Set 1	Set 2
Temperature	400 °C	400 °C
Plasma power	40 W	40 W
Pressure	800 mTorr	800 mTorr
Silane flow	5—50 sccm	20 sccm
Ammonia flow	20 sccm	20 sccm
Nitrogen flow	980 sccm	980 sccm
Deposition time	5—7 min	3—11 min

Table 6: **Overview of deposition parameters for a-SiN$_x$:H /a-SiN$_x$:H stack.**

	Layer 1	Layer 2
Temperature	400 °C	400 °C
Plasma power	40 W	40 W
Pressure	800 mTorr	800 mTorr
Silane flow	50 sccm	10 sccm
Ammonia flow	20 sccm	20 sccm
Nitrogen flow	980 sccm	980 sccm
Deposition time	2.7 min	3.4 min

Some extra samples were deposited in addition to the samples in Set 1 and Set 2, and the deposition parameters for these are given in Appendix A. These include

- Sample 26d and sample 33c from the specialization project work [43]
- Sample 31d, which was used in the laser-contact experiment
- Sample 28c, deposited on *n*-type silicon
- Sample 45c—d, deposited on FZ silicon

Remote expanding thermal plasma (ETP) PECVD

The remote ETP system used in this work is an industrial in-line system, designed for high deposition rates and high throughput. Being a remote type reactor, the main difference from the direct reactor is that the plasma is located distant to the wafers. The three DC powered ETP plasma sources ionize argon atoms outside the deposition chamber, and process gases are added to the expanding plasma at the top of the chamber. A schematic of the operation principle of the remote ETP system is given in Figure 19. The samples are heated prior to deposition, and the system is operated under vacuum. Silane (SiH_4) and ammonia (NH_3) are the precursor gases for silicon nitride deposition in this system.
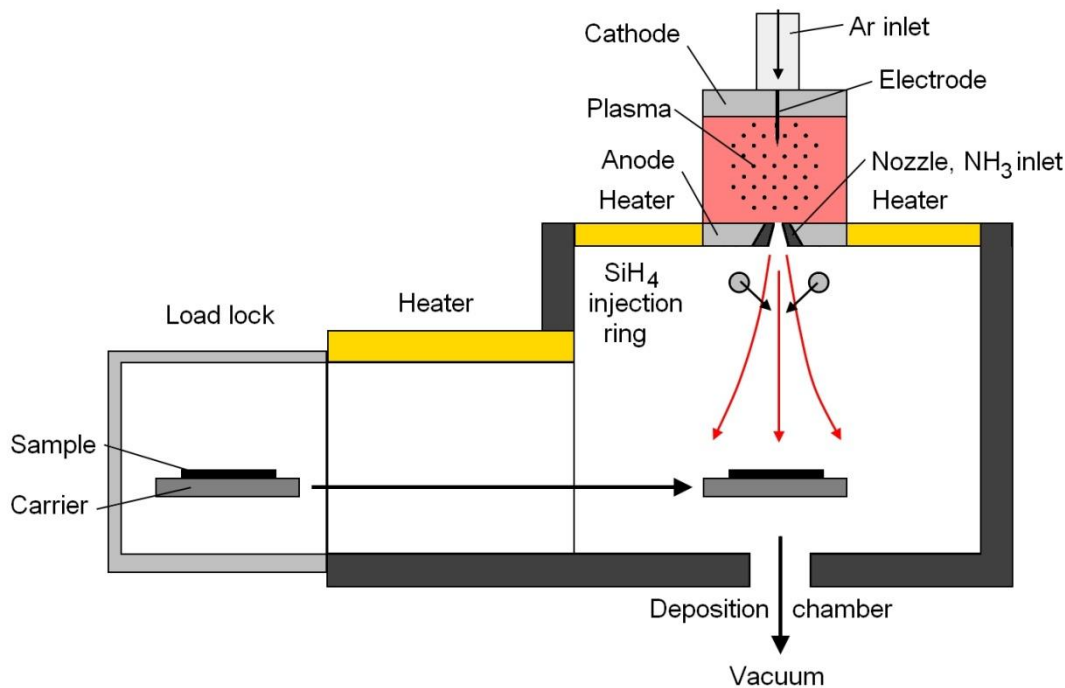

Figure 19: Schematic of the remote expanding thermal plasma (ETP) deposition system, designed for industrial in-line processing, with a load lock, heating section and the deposition chamber. The plasma is generated outside the deposition chamber, where argon is ionized by the electrode. NH_3 is injected through a nozzle, and the plasma expands. SiH_4 is added through an injection ring near the top of the chamber. For simplicity, only one of the three ETP sources is included in the schematic.

The remote PECVD reactor used was an OTB DEPx 2400 system with a vacuum carrier transport system for in-line processing. Deposition rates >6 nm/s can be obtained. Wafers were heated using IR lamps, and temperatures above 500 °C can be reached. The deposition chamber had three plasma sources with their own gas supplies. Each plasma source was an Ar-NH_3-SiH_4 system, with argon inlet pressure 200—500 mbar, arc current 40—100 A, arc voltage 40—60 V, ionization efficiency 10—40 %, ion energy 0.5 eV and electron energy 0.2 eV.

A total of 12 samples were fabricated using remote PECVD. A third set of parameter variations was deposited, where the gas flow ratio was varied in order to adjust the film composition. An overview of the deposition parameters is given in Table 5, and here the range of gas flows are the total range of the three different plasma sources in the system. For detailed deposition conditions for each sample, and gas flows of all three plasma sources, see Appendix A.

Table 7:   **Overview of deposition parameters for a-SiN$_x$:H, Set 3: Gas flow ratio variation in remote PECVD.**

Parameter	Set 3
Average temperature	407 ± 7 °C
Arc current	80 A
Arc voltage	44.2 V
Pressure	185 mTorr
Silane flow	0.047—0.147 slm
Ammonia flow	0.25—0.68 slm
Argon flow	2 slm
Deposition time	29.7 s

3.1.3   Heat treatment

In order to investigate the effect of a heat treatment corresponding to that used in industrial screen printing, samples b and d received a rapid anneal. A Radiant Technology corporation LA-309 belt furnace was used. In Figure 20, the temperature profile of the process is given. The total annealing time was less than 1 minute and the maximum temperature was ~780 °C.
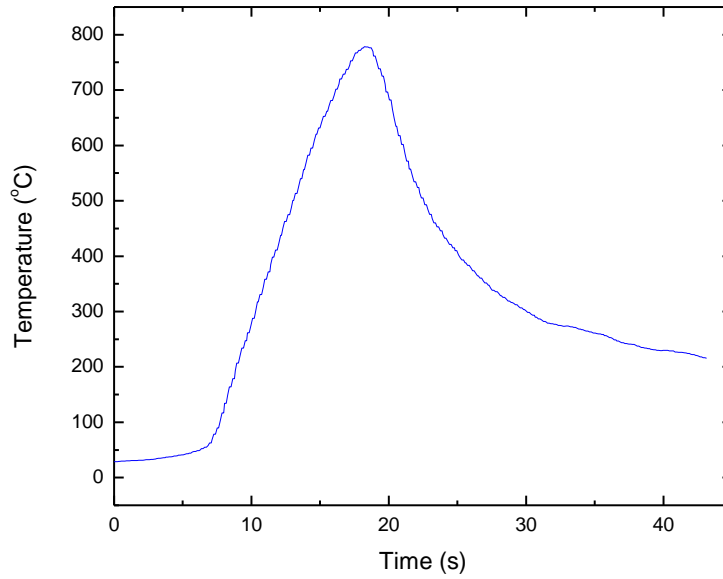

Figure 20:   Temperature profile for post deposition heat treatment carried out in a belt furnace.

3.1.4   Contact metallization

For electrical characterization of the a-SiN$_x$:H thin films, aluminium top electrodes were thermally evaporated onto the samples in order to create MIS structures. A square lattice of circular electrodes with thickness ~200 nm and diameter ~1 mm was obtained using a shadow mask. The electrode spacing was ~1 mm.

A Nano36 thermal evaporator system from Kurt J. Lesker Company was used to make the contacts, and a schematic of the technique is given in Figure 21. The process takes place in a vacuum chamber with a rotating sample holder. Aluminium pellets are placed in a crucible, which is heated using electricity. A thin metallic film is formed as metal atoms evaporate and deposit on the sample, and the film thickness is controlled by a quartz crystal detector.
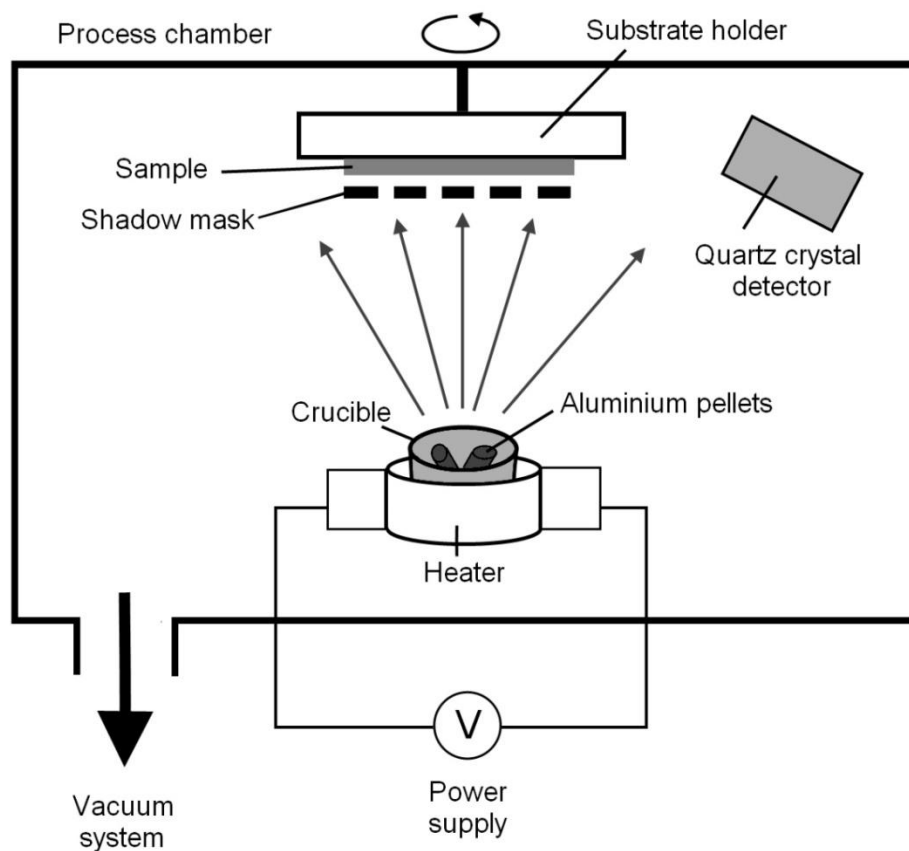

Figure 21:   Schematic of the thermal evaporator system with aluminium pellets placed in a crucible, a heater powered by electricity, a rotating substrate holder, a quartz crystal detector measuring film thickness, and a vacuum pump system.

3.1.5   Laser treatment of contacts

Isolated MIS structures were made by removing silicon nitride around metal contacts using a laser, as illustrated in Figure 22. A J-1030-515-343 FS industrial system from Oxford Lasers with a s-Pulse HP laser from Amplitude Systems was used. The laser beam had a pulse length of 4 ps and a wavelength of 1030 nm. The spot size was 40 μm, referring to the full width in the intensity distribution, where the intensity is reduced to $1/e^2$ of the peak intensity. Processing was performed using a power of ~40 mW and a pulse repetition frequency of 10 kHz. A groove around the contact was made by sweeping the laser beam in concentric circles, using a scan speed of 5 mm/s and an increase in the circle radius of 5 μm for each circular sweep. 4 repetitions were performed in order to make a groove deep enough to remove all silicon nitride and some of the silicon underneath. In order to ensure no silicon nitride was left outside the contact area, the inner circle was smaller than the original electrode, reducing the diameter of the aluminium electrode from ~1 mm to 0.8 mm. The outer circle had a diameter of 2.5 mm, giving a groove width of approximately 0.85 mm.
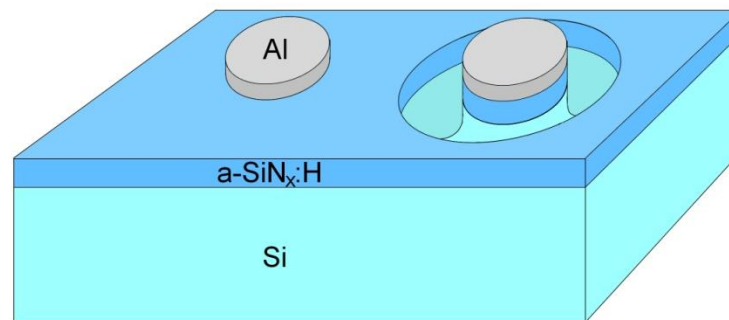

Figure 22:   Original MIS structure to the left and a laser isolated MIS structure to the right.

3.2 Characterization
3.2.1 Spectroscopic ellipsometry

Spectroscopic ellipsometry was used to measure the film thickness and optical properties of the thin films. Ellipsometry is a technique where polarized light interacts with the dielectric film, and the change in polarization is measured. The name ellipsometry originates from the fact that reflected light often becomes elliptically polarized, which is the most general form of polarization [44], and the experimental setup is sketched in Figure 23. In spectroscopic ellipsometry, electromagnetic radiation of different wavelengths is generated in the light source and sent through a polarizer, giving linearly polarized waves. The light then irradiates the sample at an angle Φ, and the reflected beam goes through the analyzer, which is another polarizer. Finally, the detector measures the change in polarization in the reflected beam.
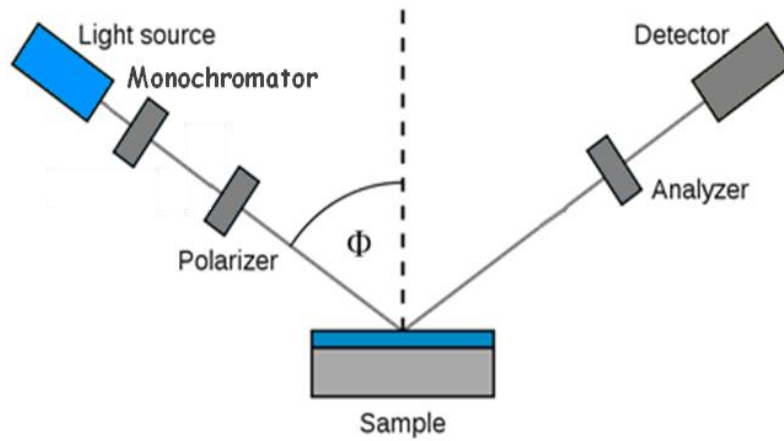
Figure 23: **Schematic of the ellipsometry setup.**

Polarization of the electromagnetic waves is described by two components, relative to the plane of the incident and reflected beam and to the plane of the sample. Waves polarized parallel to the plane of incident and reflected beams are p-polarized. s-polarization is parallel to the sample plane and orthogonal to the light beam plane. The complex reflectance ratio ρ is measured. ρ is the ratio of the normalized amplitudes of the two components of the reflected beam, R_p and R_s:

$$\rho = \frac{R_p}{R_s} = \tan(\Psi)\,e^{i\Delta}$$

(32)

where Ψ is the amplitude ratio of the reflected beam and Δ is the phase shift [44]. Ellipsometry is an indirect method. A spectroscopic scan results in graphs of Ψ and Δ as functions of wavelength. These have to be fitted to a model in order to calculate the thickness, refractive index and absorption coefficients.

The tool used was a Variable Angle Spectroscopic Ellipsometer (VASE) instrument from J. A. Woollam Co. Inc. with a VB-400 Control Module and an HS-190 Monochromator.

Measurements were performed using spectroscopic scans with wavelengths ranging from 300 to 1000 nm and incident angles of 65°, 70°, and 75°. The results were fitted to a model consisting of a 300 µm thick silicon substrate with a transparent Cauchy layer on top, representing the a-SiN$_x$:H film. The optical properties of matter are described by the complex refractive index, given by

$$n = n + i\kappa$$

<div align="right">(33)</div>

where n is the real part of the refractive index, and κ is the extinction coefficient. κ is a measure of the absorption in the material, and is neglected in the Cauchy model. By fitting the measured ellipsometry data to the model, the film thickness and the real part of the refractive index as a function of wavelength were extracted. An example of experimental data for Ψ and Δ, and resulting fits to the model are given in Figure 24. For simplicity, the refractive index at 630 nm is used as a representative value of the refractive index in the rest of this work.
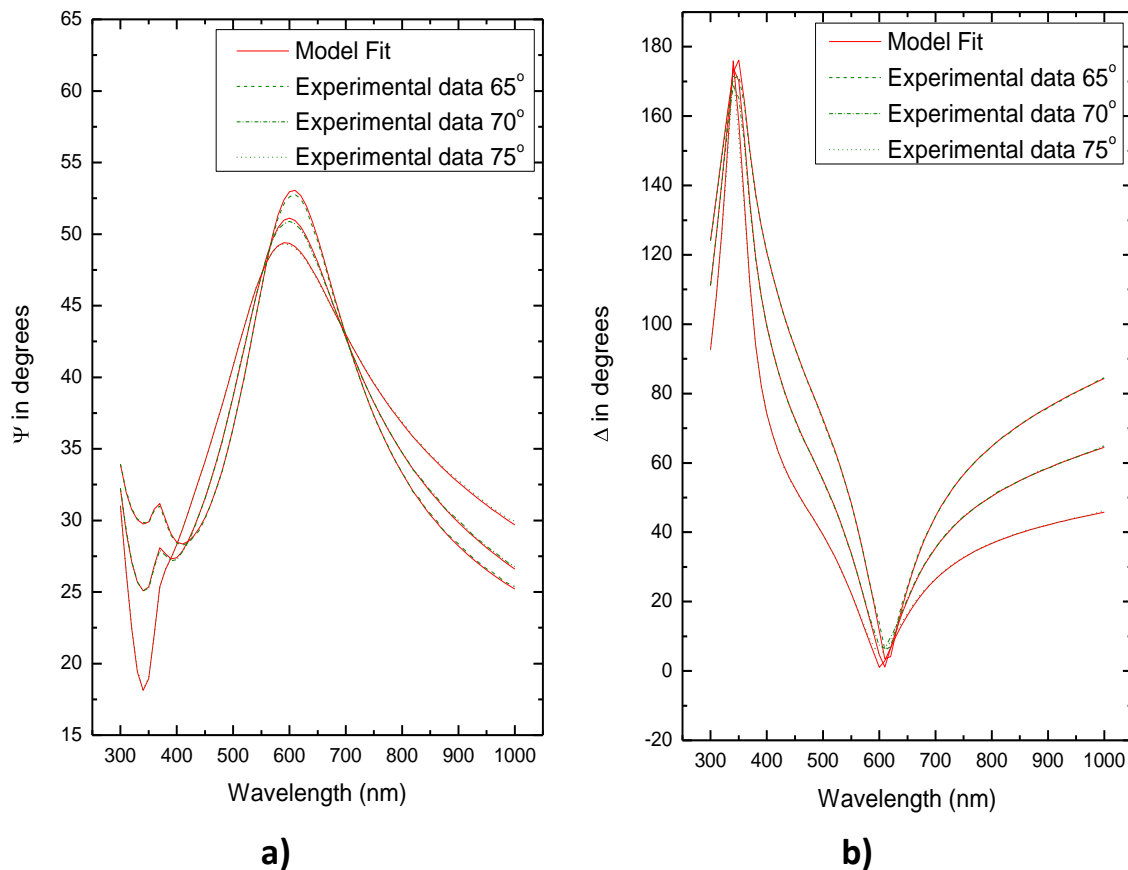

a) **b)**

Figure 24: **Example of experimental data and model fit for ellipsometry analysis of a-SiN$_x$:H thin films: Experimental data for a) Ψ and b) Δ at angles of 65°, 70°, and 75° combined with the resulting fit to the model for sample 52a.**

3.2.2   Quasi-steady-state photoconductance

Lifetime measurements were carried out using the quasi-steady-state photoconductance (QSSPC) method, giving the effective minority carrier lifetime as a function of injection level. The photoconductance is measured under steady-state illumination, and the increase in wafer conductivity is given by [45]

$$\sigma_L = q\Delta n(\mu_n + \mu_p)W \;,$$

(34)

where W is the wafer thickness and μ_p and μ_n are the hole and electron mobilities, respectively. Assuming steady state conditions, the photogeneration and recombination rates are equal. The rates can be expressed as current densities depending effective minority carrier lifetime,

$$J_{ph} = J_{recomb} = \frac{\Delta nqW}{\tau_{eff}}\,.$$

(35)

Combining equations (34) and (35) give an expression for the effective lifetime:

$$\tau_{eff} = \frac{\sigma_L}{J_{ph}(\mu_n + \mu_p)}$$

(36)

The conductance is measured using an inductive coil connected to an RF bridge and the photogeneration is measured relative to a calibrated photo diode [45]. In this work, a WCT-120 Photoconductance Lifetime Tester from Sinton Instruments was used. The experimental setup is sketched in Figure 25.

Due to different surface reflectance of the samples, the value of the photogenerated current had to be adjusted relative to the current induced in the reference photo diode (38 mA/cm^2 at 1 sun). The optical constant in the lifetime spreadsheet was adjusted for different film thicknesses, and values in the range 0.85—1.05 were used [46].

In order to map the lifetime over the largest possible range of injection levels, measurements were performed using two different diffusers. Using the diffuser with the largest reduction of light intensity resulted in low injection curves. Correspondingly, the curves obtained at the highest light intensity are referred to as high injection curves.

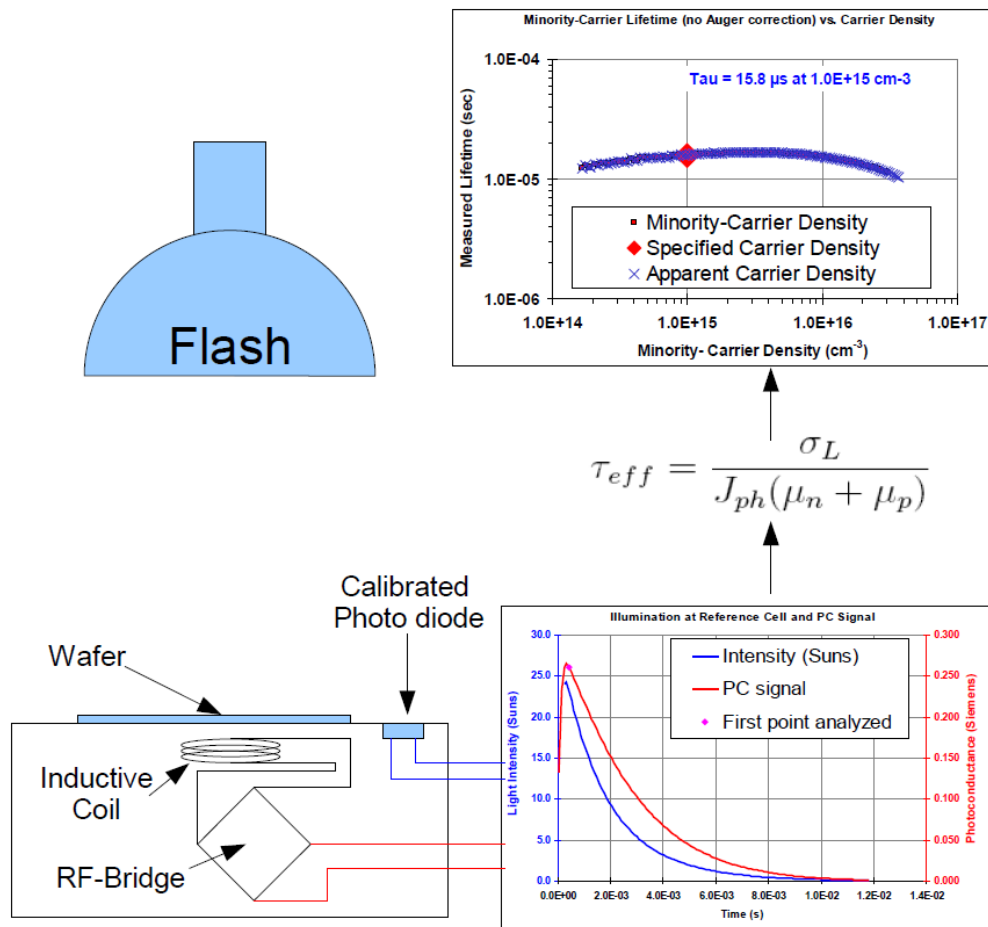$$\tau_{eff} = \frac{\sigma_L}{J_{ph}(\mu_n + \mu_p)}$$

Figure 25: **Schematic of the QSSPC setup [47]. The flash generates minority charge carriers in the wafer and the photo diode. Typical output graphs of the measured photoconductance and light intensity are shown in the bottom left corner. A typical calculated lifetime vs. injection level curve calculated by the software is given in the top left corner.**

3.2.3   Stability measurements

The stability of the passivation layers with respect to solar irradiation was investigated by illuminating the samples in a solar simulator for a controlled period of time, and measuring lifetime using QSSPC between the exposures to solar irradiation. A total exposure time of 1 hour was conducted during one day, followed by a 2 weeks pause (where the samples were stored in the dark) and the final exposure up to 2 hours. Illumination was performed in a Wacon WXS-150S-10,AM0 solar simulator with a Wacon Xenon short arc lamp KXL-1000F. The irradiance spectrum of the system is given in Figure 26. A Julabo F12 cooling system with temperature control was used to maintain a constant temperature of 30 °C during illumination.
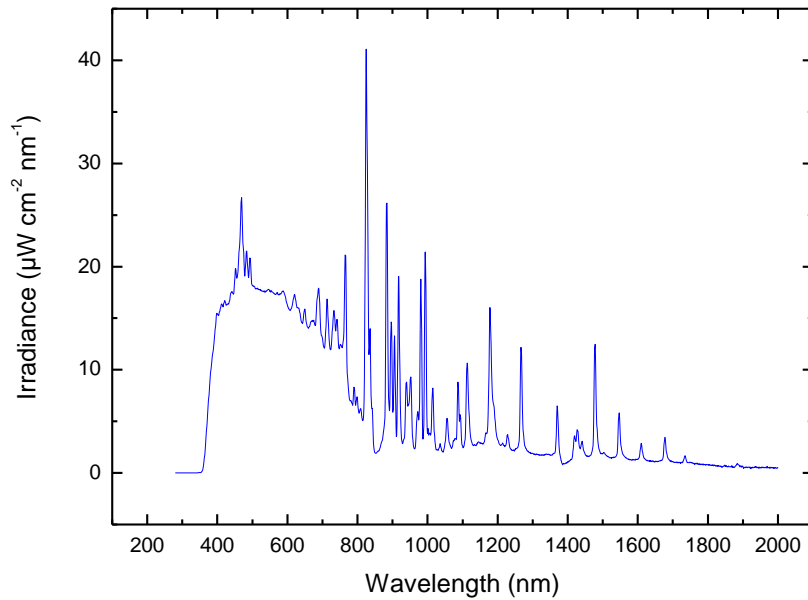

Figure 26:   Spectrum of the Wacon WXS-150S-10,AM0 solar simulator used.

3.2.4   **Electrical characterization**

Capacitance-voltage (C-V), conductance-voltage (G-V), conductance-frequency (G-f), current-voltage (I-V) and current-time (I-t) measurements were performed in order to investigate the electric properties of the silicon nitride film.

All electrical characterization measurements were performed using a Keithley 4200-SCS semiconductor characterization system, shown in Figure 27a. The samples were mounted to a Signatone S-1060R QuieTemp Hot Chuck System, as shown in Figure 27b, using vacuum. High frequency capacitance and conductance measurements were performed using a 4210-CVU Capacitance Voltage Measure Unit. AC signal frequencies were in the range 1 kHz – 10 MHz. Quasi-static C-V and current measurements were performed using two 4200 Medium Power source measure units (SMU).

High frequency C-V and G-V measurements were performed in the dark at room temperature, with voltage sweeps from inversion via accumulation, and back into inversion, for voltages in the range ± 30 V. The step increment was in the range 0.1 – 0.2 V, with a sweep delay of 0.5 s. The applied AC signal had frequencies 10 kHz, 100 kHz and 1 MHz, with 30 mV amplitude.

Quasi-static C-V measurements, as well as I-V and I-t measurements, were performed in the dark at room temperature. The I-V measurements were also carried out at temperatures up to 200 °C. Voltages in the range ± 10 V were applied.
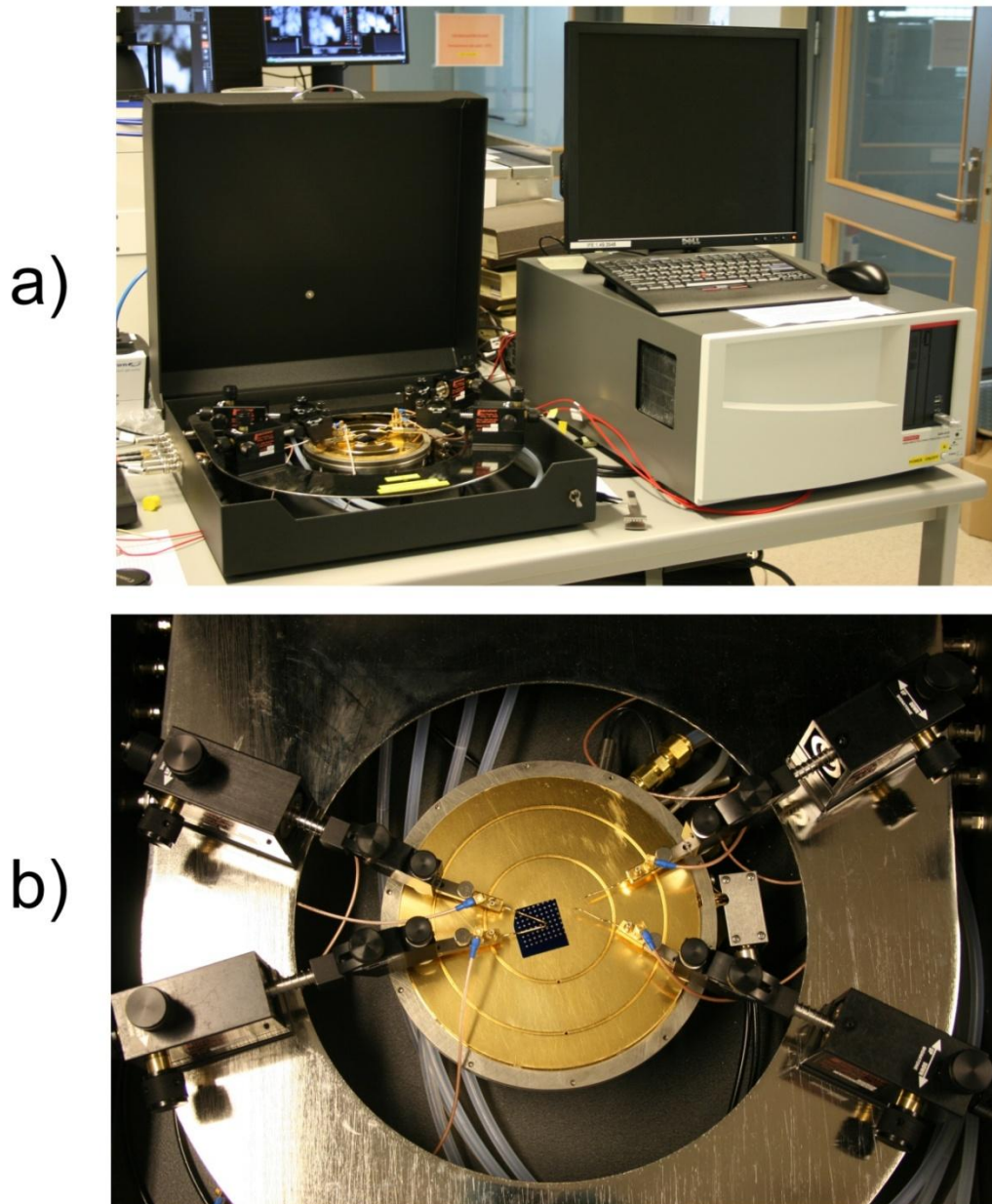
Figure 27: a) Keithley 4200-SCS semiconductor characterization system used for electrical characterization. b) Close-up of Signatone probe station.

3.2.5   Determination of electrode area

In the specialization project, uncertainties in the electrode areas showed a large impact on measurement results [43]. In order to reduce this uncertainty, the electrode areas were estimated using optical microscopy and image processing. An Axioskop 2 MAT optical microscope from Zeiss, with an Alicona ALC13 camera was used. Images were captured at 2.5x magnification, and further manipulated using the image processing software ImageJ.

A typical microscopy image of a sample with contacts is given in Figure 28 a. The «Set scale» function was used to set the scale bar. Adjusting contrast and using the «Make binary» function resulted in the black-and-white image shown in Figure 28b. The built in «Analyze particles» function was used to determine the number of particles and their individual size. An illustration of the result of the particle analysis is shown in Figure 28 c, with outlines of the electrodes.

3.2.6   3D optical microscopy imaging

3D images mapping surface structure were captured using an optical microscope with a 3D mapping function. An Axioskop 2 MAT optical microscope from Zeiss was used, equipped with an Alicona ALC13 camera and dedicated 3D mapping software. Images were captured using a lens with 50x magnification.
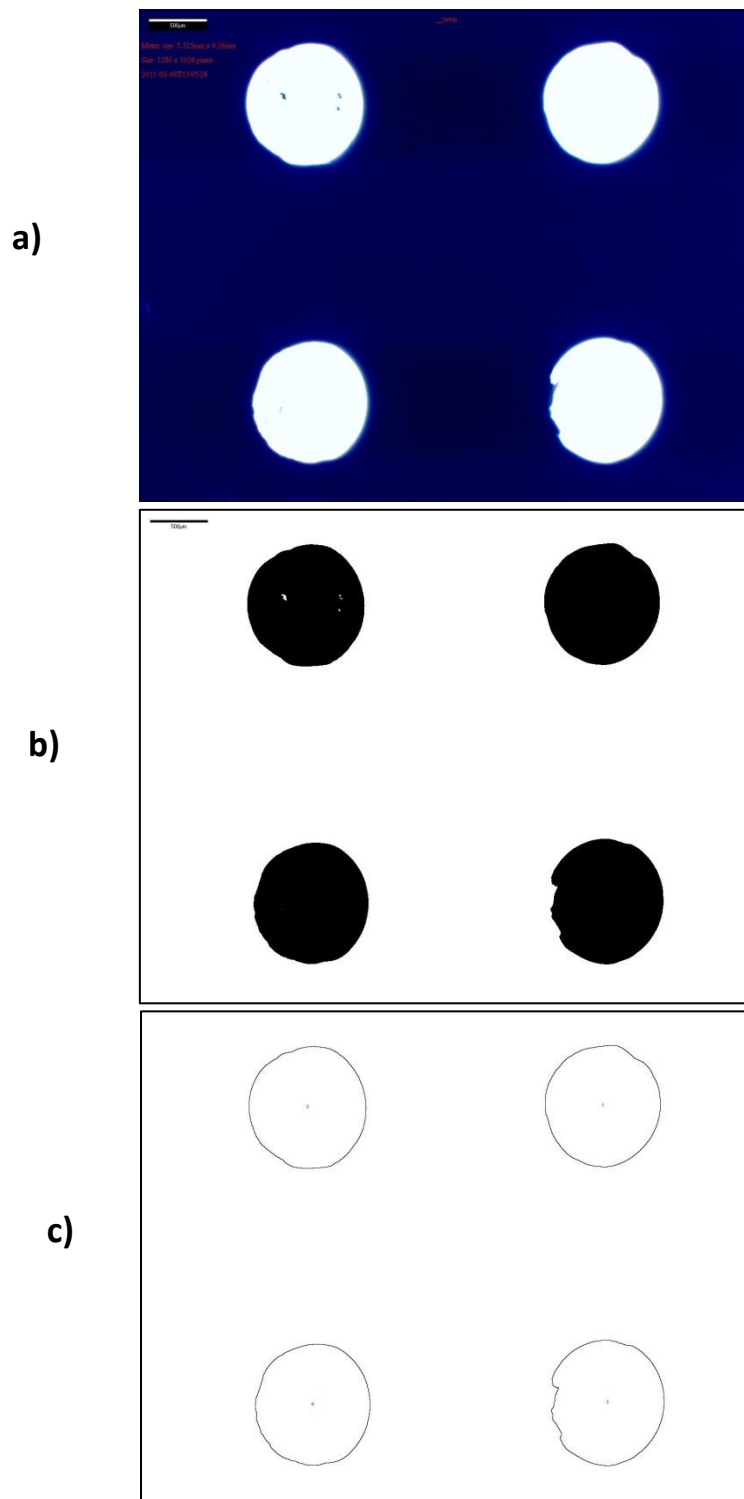
Figure 28: **Illustration of procedure for measuring electrode area: a) Microscopy image of aluminium contacts on a-SiN$_x$:H, the scale bar is 500 µm, b) Image after contrast adjustment and binary conversion, c) outlines of contacts found by the «Analyze particles» function.**

3 Experimental

4 Results and discussion

In this chapter, the results of this work are presented and discussed, and the chapter is divided into subchapters according to topic. A general description of the prepared samples is given in Section 4.1, along with an analysis of the sample uniformity. In Section 4.2, some aspects regarding electrical characterization of a-SiN$_x$:H thin films are presented. The results from the investigations of the properties of a-SiN$_x$:H films deposited by the two different reactor systems are given and discussed in Section 1.1 (direct PECVD) and Section 1.1 (remote PECVD). Finally, carrier transport and charging phenomena in a-SiN$_x$:H are studied in more detail in Section 1.1.

4.1 General examination of samples

Visual inspection showed that the manufactured samples in this work were uniform and without visible defects. The a-SiN$_x$:H thin films had different colors, depending on film thickness and refractive index, and the surface had a higher specular reflectivity than conventional silicon nitride covered solar cells. This is due to the lack of texturing, as the films are deposited on polished wafers. The color of the samples did not change during heat treatment, light exposure or storage, and blistering was not observed. A typical sample for lifetime measurements is given in Figure 29a, and the corresponding sample with contacts for electrical characterization is given in Figure 29b.

An ellipsometry analysis of 9 points on sample 52a was performed in order to investigate the uniformity of the thin film. The resulting film thickness of 92.62 ± 0.09 nm and refractive index of 1.8854 ± 0.0003 at wavelength 630 nm confirm the homogeneity of the a-SiN$_x$:H film with respect to film thickness and refractive index.
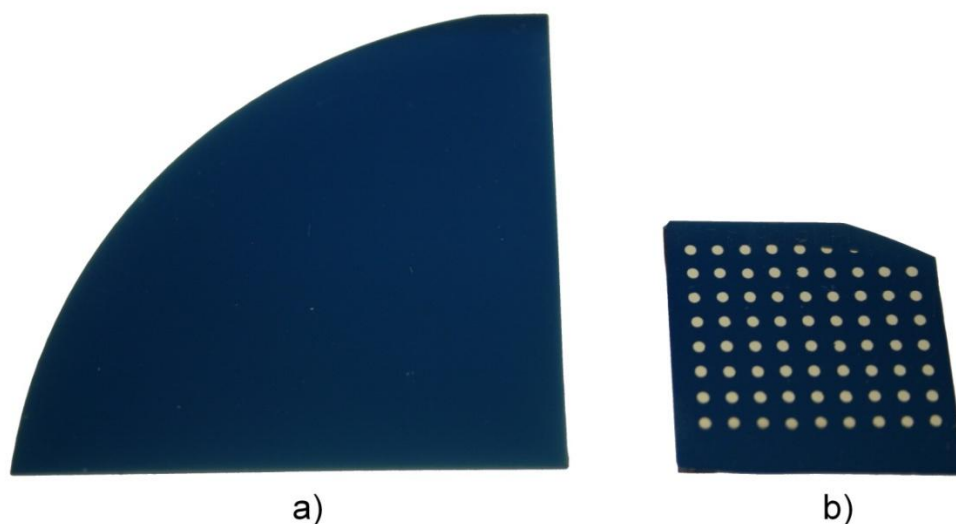

a)   b)

Figure 29: **Typical a-SiN$_x$:H samples: a) Sample 52a for lifetime measurements, with refractive index 1.88 and film thickness 93 nm giving blue color, b) Sample 52c with contacts for electrical characterization.**

4.2 Electrical characterization of a-SiN$_x$:H thin films

In this section, methodology and general results from electrical characterization of a-SiN$_x$:H MIS structures are presented and discussed, with emphasis on high frequency C-V measurements, the conductance method and quasi-static C-V measurements. The parts concerning hysteresis effects and positive charges are summaries of the results obtained in the specialization project conducted during fall 2010 [43].

4.2.1 High frequency C-V measurements

The high frequency C-V curve for sample 52c-2 is given in Figure 30. A frequency of 1 MHz for the applied AC signal was used, and similar behavior is observed for all a-SiN$_x$:H films on *p*-type substrate in this work. The C-V curve shows the expected transition between low capacitance in the inversion region and high capacitance in accumulation, and the shape of the curve corresponds well to previously reported results for a-SiN$_x$:H MIS capacitors [16, 24, 29].

Figure 30: **C-V curve at 1 MHz for sample 52c-2, showing a curve shape typical for samples of a-SiN$_x$:H capacitors. The voltage sweep started in inversion, and the sweep direction is indicated by the arrows. In the graph, the accumulation, depletion and inversion regions are indicated.**

The high frequency C-V behavior of the a-SiN$_x$:H capacitors in this work show some deviations from the ideal MIS capacitor. In Figure 31, the C-V characteristic of sample 33c is shown for sweeps at 1 MHz, 100 kHz and 10 kHz. The following features are characteristic for all a-SiN$_x$:H thin films on *p*-type substrate investigated in this work:

- **Positive charges:** The curve is shifted towards negative voltages compared to the ideal MIS characteristic, indicating the presence of fixed positive charges in the a-SiN$_x$:H film
- **Hysteresis effects:** A significantly lower flat band voltage is measured when sweeping from accumulation to inversion than for the opposite direction
- **Inversion region capacitance:** Increasing capacitance with decreasing frequency in the inversion region is measured

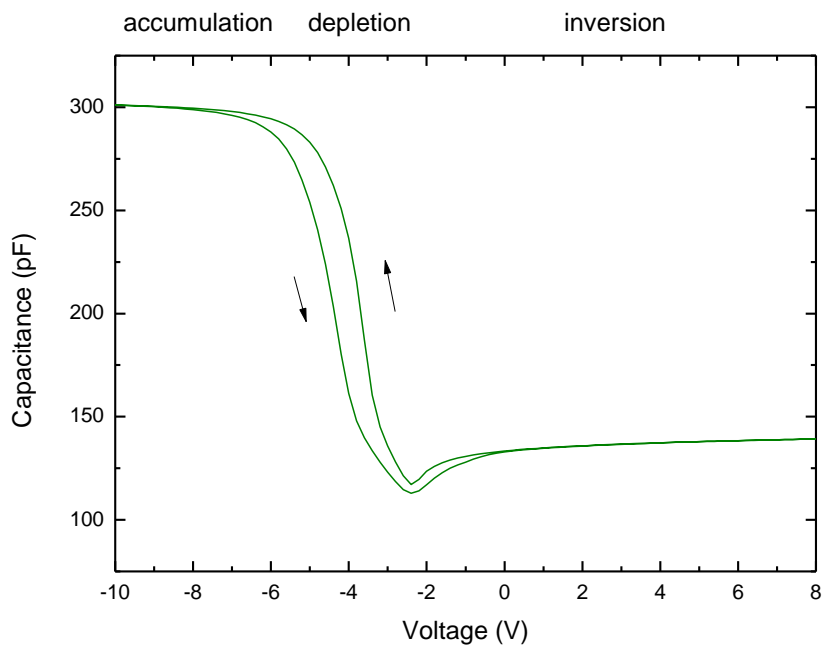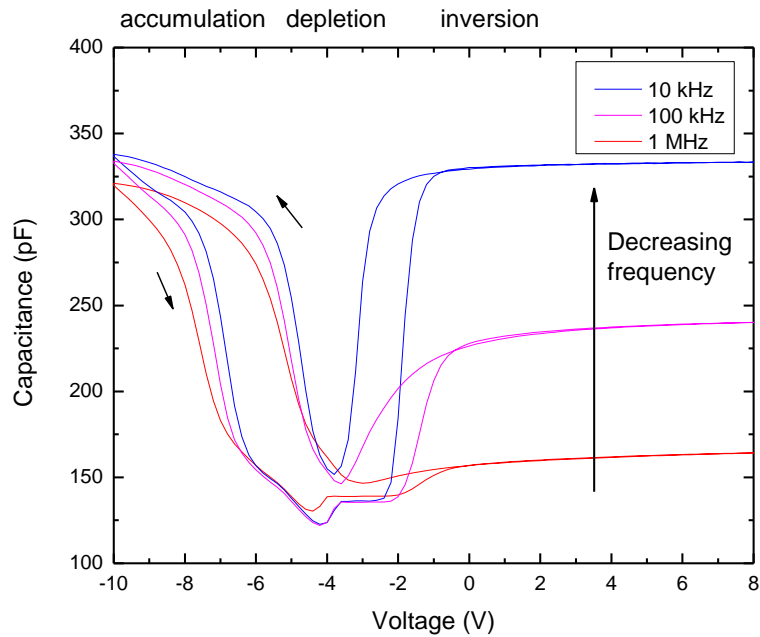**Figure 31: C-V curve for sample 33c, showing a curve shape typical for samples of a-SiN$_x$:H capacitors. The voltage sweep started in inversion, and the sweep direction is indicated by the small arrows. In the graph, the accumulation, depletion and inversion regions for forward sweeps are indicated.**

Positive charges

Analysis of the C-V curves indicate a presence of positive charge in the a-SiN$_x$:H thin films, due to the shift of the C-V curve towards negative voltages. Using equations 13—17, the flat band voltage and the fixed charge density were estimated, and the resulting values obtained were typically in the range from −3 to −6 V for the flat band voltage and 1–9×10^{12} cm^{-2} for the fixed charge density. The values for Q_f correspond well to those found by Aberle [4] and the flat band voltage was observed at approximately 0.8 C_i.

For a positively charged passivation layer on *p*-type silicon, the surface should be in inversion in order to get a large enough difference in carrier concentrations to reduce the surface recombination rate. As described in Section 2.3.1, the work function difference between silicon and aluminium is approximately −0.87 eV. According to Elmiger and Kunst [28], the positive charges are distributed 20 nm into the silicon nitride layer. This gives a minimum Q_f

value of ~10^{11} cm^{-2} required for inversion conditions at the interface. Hence the films deposited in this work should contain large enough quantities of charges for field effect passivation to be present.

Hysteresis effects

Hysteresis effects were observed for all a-SiN$_x$:H samples, with the transition from low to high capacitance occurring at lower voltages for the reverse voltage sweep from accumulation to inversion.

The width of the hysteresis loop varies as a function of the number of measurements performed, and with the starting and ending point of the voltage sweep. Figure 32 illustrates the change in hysteresis for consecutive measurements. For this particular sample, the width of the hysteresis loop was reduced from 5 V to 2 V through 5 measurement cycles. The largest reduction in the hysteresis loop is generally observed for the second measurement, and saturation is observed for repeated cycles.

The origin of these hysteresis effects is not well understood. As mentioned in Section 1.1.1, Aberle states that C-V measurements are inaccurate due to the fact that the samples are not independent of measurement history. The applied bias will cause trapping and emission of carriers in K centers, interface states and other defects.
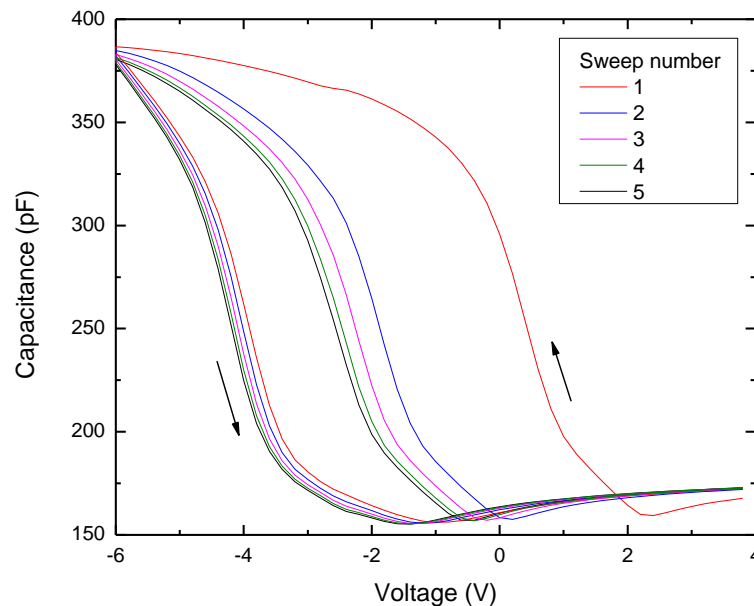

Figure 32:   **Change in hysteresis for successive measurements on sample 26c. The voltage sweep started in inversion, and the sweep direction is indicated by the arrows. A large hysteresis loop is observed in the first measurement, and the width of the hysteresis loop decreased as measurements proceeded, reaching saturation.**

When attempting to analyze the hysteresis effects observed on a-SiN$_x$:H MIS capacitors, it is useful to divide the observed behavior in two:

1. Hysteresis is observed as the voltage is swept from inversion to accumulation and back again.
2. The width of the hysteresis loop decreases towards a saturation value for repeated measurements, giving shifts in flat band voltage for sweeps from inversion to accumulation. The flat band voltages for sweeps in the opposite direction are less affected.

The first effect could be caused by an activation barrier for carriers to go into the accumulation region when the voltage is swept from positive to negative bias. When the direction of the sweep is reversed, the voltage is already supplying an energy that exceeds this barrier. Hence the transition from accumulation to depletion occurs at a lower voltage in this direction, giving rise to a hysteresis loop.

The second effect is probably caused by measurements affecting the sample. A shift in flat band voltage towards more negative values indicates an increase in the positive capacitor charge density. High voltages could inject charges from the metal contact into the nitride layer, or from the semiconductor material outside the MIS capacitor region, since the MIS structure is not confined laterally. Equivalently, charges could be extracted from the MIS structure. Trapping and emission of charge carriers under applied voltage do indeed change the initial charge distribution in a-SiN$_x$:H, and hence affects the field effect passivation. Relaxation was observed when samples were kept at zero bias for a period of time.

For sample 26d, the impact of these two hysteresis effects on flat band voltage and fixed charge density were calculated. The results are summarized in Table 8. Both effects decrease the flat band voltage towards a more negative value, and increase the fixed charge density. The hysteresis in saturation caused the fixed charge density to increase with 60 % when the sweep direction was changed from starting in inversion to starting in accumulation. Additionally, the repeated measurements give a shift in flat band voltage of 1 V, resulting in a 20 % increase in Q_f for measurement number 2 compared to the first sweep.

Table 8:   **Effect of sweep direction and consecutive measurements on flat band voltage and fixed charge density for sample 26d.**

Effect	Measurement	Voltage sweep	V_{FB} (V)	Q_f (cm^{-2})
Direction of sweep	Saturation	8 V → −8 V	− 4.5	1.0×10^{12}
	Saturation	− 8 V → 8 V	−6.6	1.6×10^{12}
Repeated measurements	1st sweep	0 V → −8 V	−4.4	1.0×10^{12}
	2nd sweep	0 V → −8 V	−5.4	1.2×10^{12}

Inversion region capacitance

The increase in inversion capacitance observed for decreasing frequencies, shown in Figure 31, corresponds well to the behaviour found by Beylier et al [15]. Their hypothesis explains the increasing inversion region capacitance by electrons in the inversion layer outside the MIS contact area influencing measurements, as illustrated in Figure 33a. In order to test this hypothesis, the a-SiN$_x$:H outside the contact area was removed using a laser, thereby eliminating the positive charges in the silicon nitride creating the inversion layer in the silicon. The resulting structure is shown in Figure 33b, and a photography of the laser treated sample is given in Figure 34. 3D optical microscopy imaging was used to map the surface structure in the region between the contact and laser groove, as shown in Figure 35. Due to the large difference in reflectance, the metal contact is not visible in the 3D plot, but an outline of the circular contact can be seen. The laser groove has a height difference of ~4 µm, which is much larger than the thickness of the a-SiN$_x$:H film (~100 nm) and the metal contact (~200 nm). This confirms that the laser treatment has removed all silicon nitride and created an isolated MIS structure.
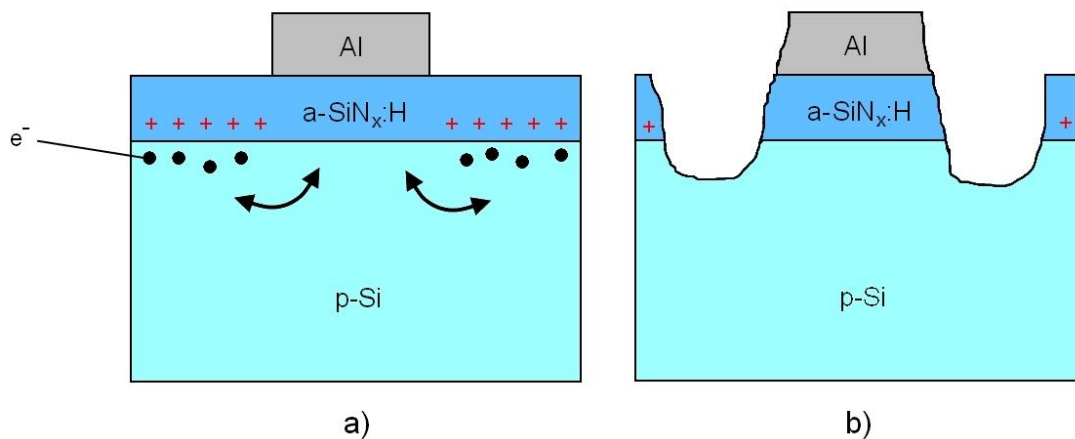
Figure 33: **a) MIS structure where electrons from the inversion region outside the MIS can compensate for applied voltages, b) isolated MIS structure where the inversion layer is removed. The figure is not drawn to scale.**
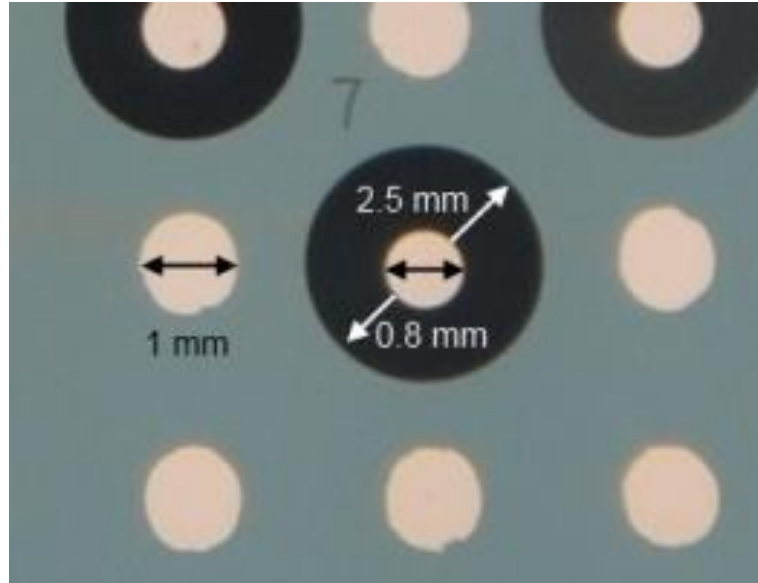
Figure 34: **Photography of laser isolated contacts. The bright spots are the metal contacts, the dark rings are laser grooves into the silicon and the light blue background is the silicon nitride. In the picture, dimensions of the sample are indicated: The diameter of the laser treated area is 2.5 mm, and the electrode size is reduced from 1 mm to 0.8 mm.**
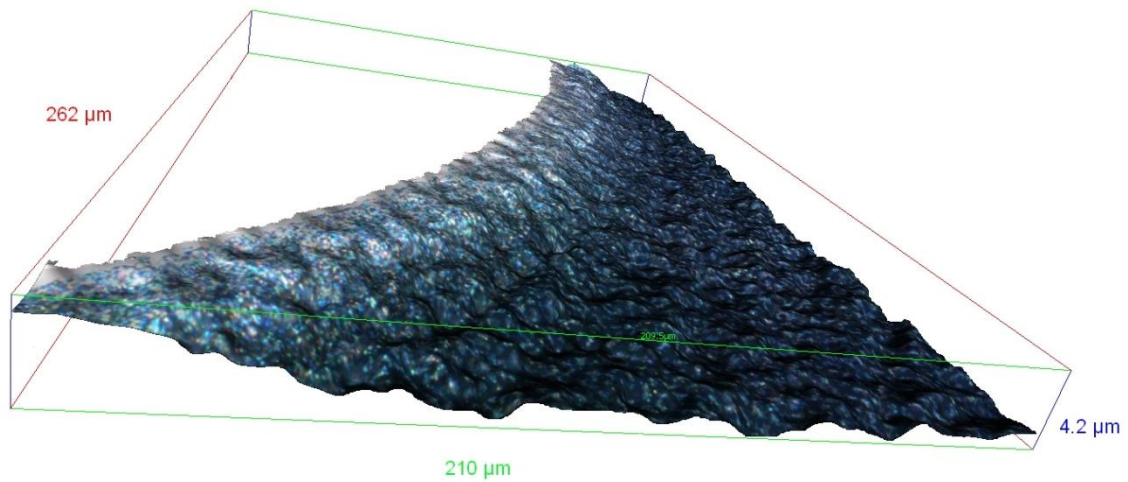
Figure 35: **3D image captured by optical microscopy showing the groove created by the laser around the circular metal contact. The large difference in reflectance of the materials causes the metal contact to appear invisible due to saturation. Due to the 4 µm height variation , the complete removal of a-SiN$_x$:H is confirmed.**

C-V measurements were conducted on a standard contact and a laser isolated contact on sample 31d, with measurement frequencies 1 MHz and 100 kHz. In Figure 36, the resulting C-V curves are shown. The frequency dependence of the inversion region capacitance was not observed for the laser isolated contact. Instead of the increasing capacitance, the laser isolated contact showed decreasing capacitance for positive voltages, with a break in the curve around zero volts. Furthermore, a shift towards smaller capacitances was also observed.

In order to investigate the inversion region capacitance effect further, C-V measurements were performed on n-type a-SiN$_x$:H MIS structure as well. The C-V characteristics of an n-type MIS at frequencies 1 MHz and 100 kHz are given in Figure 37. Due to the change in polarity, the C-V curve is inverted: At zero and positive biases, the semiconductor is in accumulation, and for large negative biases it is in inversion. The increase of capacitance in the inversion regime is not observed for n-type MIS structures. However, a decrease in capacitance and a break in the curve were observed, in a similar manner as for the laser isolated MIS structures.

The fact that the inversion region capacitance effect disappears for isolated MIS structures on p-type substrate, and is absent for n-type MIS structures indicate that the effect is caused by the electron inversion layer outside the MIS area (Figure 33a). Hence the investigations in this work support the hypothesis of Beylier et al. This effect is not observed for the hole inversion layer in the n-type MIS structure, which can be explained by the lower mobility of holes, preventing them from responding to frequencies in the kHz range. The decreased insulator capacitance in the laser isolated MIS can be related to the reduction in electrode area after the laser treatment. Some of the contact area was removed in order to be certain that no nitride was left outside the MIS structure. A reduction in the capacitor area of 36 % should decrease the insulator capacitance with ~85 pF, which agrees well with the experimental data. The breaks in the curves in the inversion region could be caused by DC leakage currents through the insulator, as suggested by Hielscher and Preier [17].
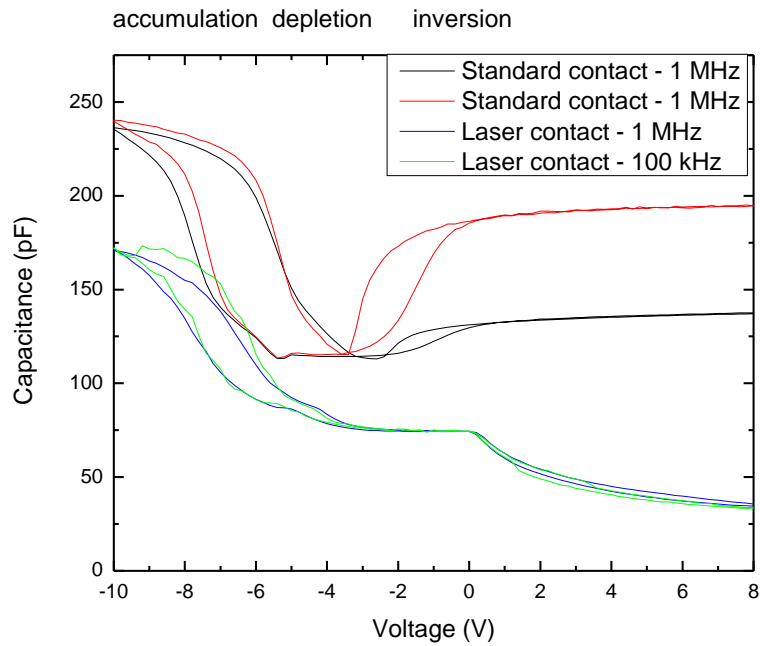
Figure 36: C-V curves for a standard and laser isolated contact, at frequencies 1 MHz and 100 kHz. The measurements were conducted on sample 31d, and the approximate positions of the inversion, depletion and accumulation regions are indicated.
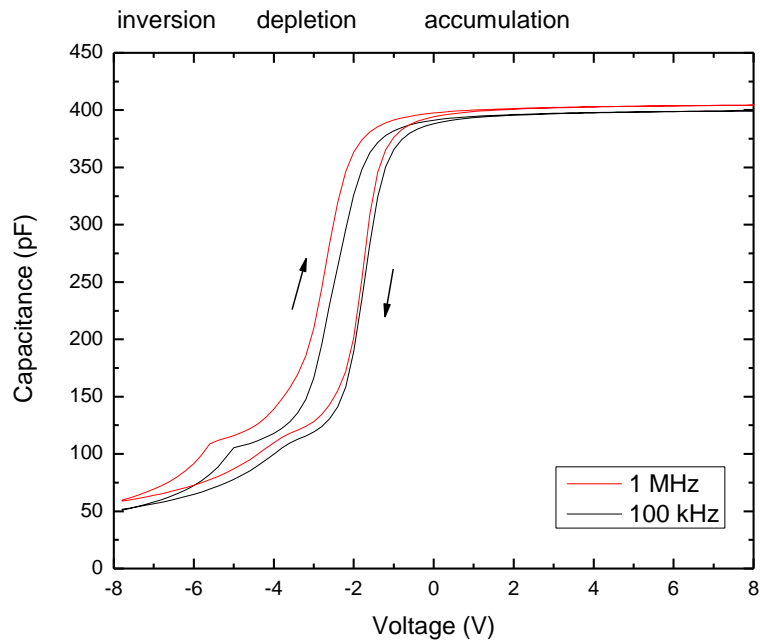
Figure 37: C-V measurement on *n*-type a-SiN$_x$:H MIS structure, sample 28c, with frequencies 1 MHz and 100 kHz. The sweep started in inversion and the approximate positions of the inversion, depletion and accumulation regions for the forward sweep are indicated.

4.2.2   The conductance method

Conductance-voltage (G-V) measurements were performed in order to estimate the density of interface traps D_{it}. The approach is outlined in Section 2.3.2.

A combined C-V and G-V curve for a measurement for sample 29d at 10 kHz is given in Figure 38. The minor conductance peak in the depletion region represents the increase in conductance due to the capture and emission of carriers by interface traps, and the major peak is most likely related to the inversion region capacitance effect.
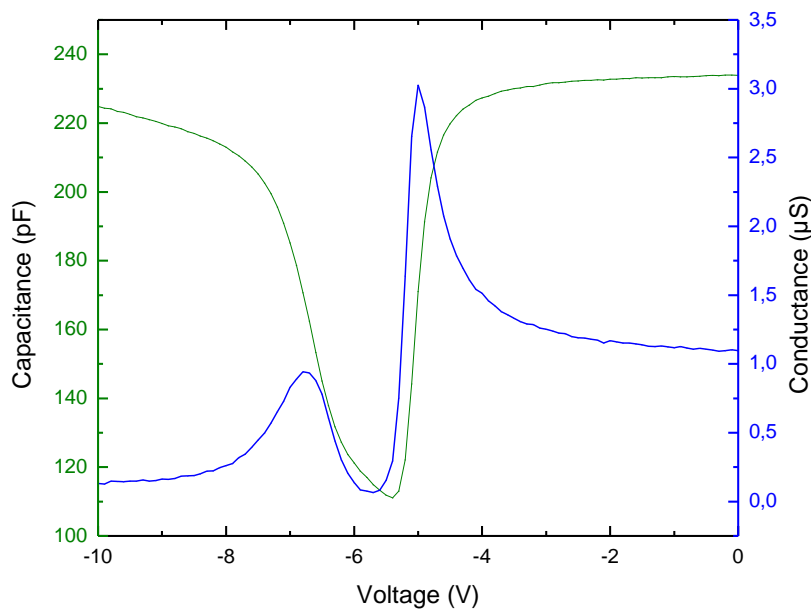
Figure 38:   Combined C-V and G-V curve at 10 kHz for sample 29d. The minor peak is related to D_{it} and the major peak is most likely caused by the inversion region capacitance effect.

Two approaches were used in order to eliminate the contribution from series resistance and extract the peak magnitude: The analytical method and the linear interpolation method, both described in Section 2.3.2. Using the analytical approach resulted in fits of varying quality, as illustrated in Figure 39. For sample 51c-1 in Figure 39a, the estimated series resistance contribution to the conductance (blue curve) fitted well to the bottom of the measured conductance (black curve), giving a corrected curve that approaches zero on both tails (red curve). This is an example of a good fit, where the magnitude of the peak can easily be extracted. In Figure 39b, the fit is poor, because there is an offset between the estimated and measured curve on both sides of the conduction peak. The resulting red curve falls below zero, and hence the maximum value of the corrected peak does not represent the original peak magnitude.
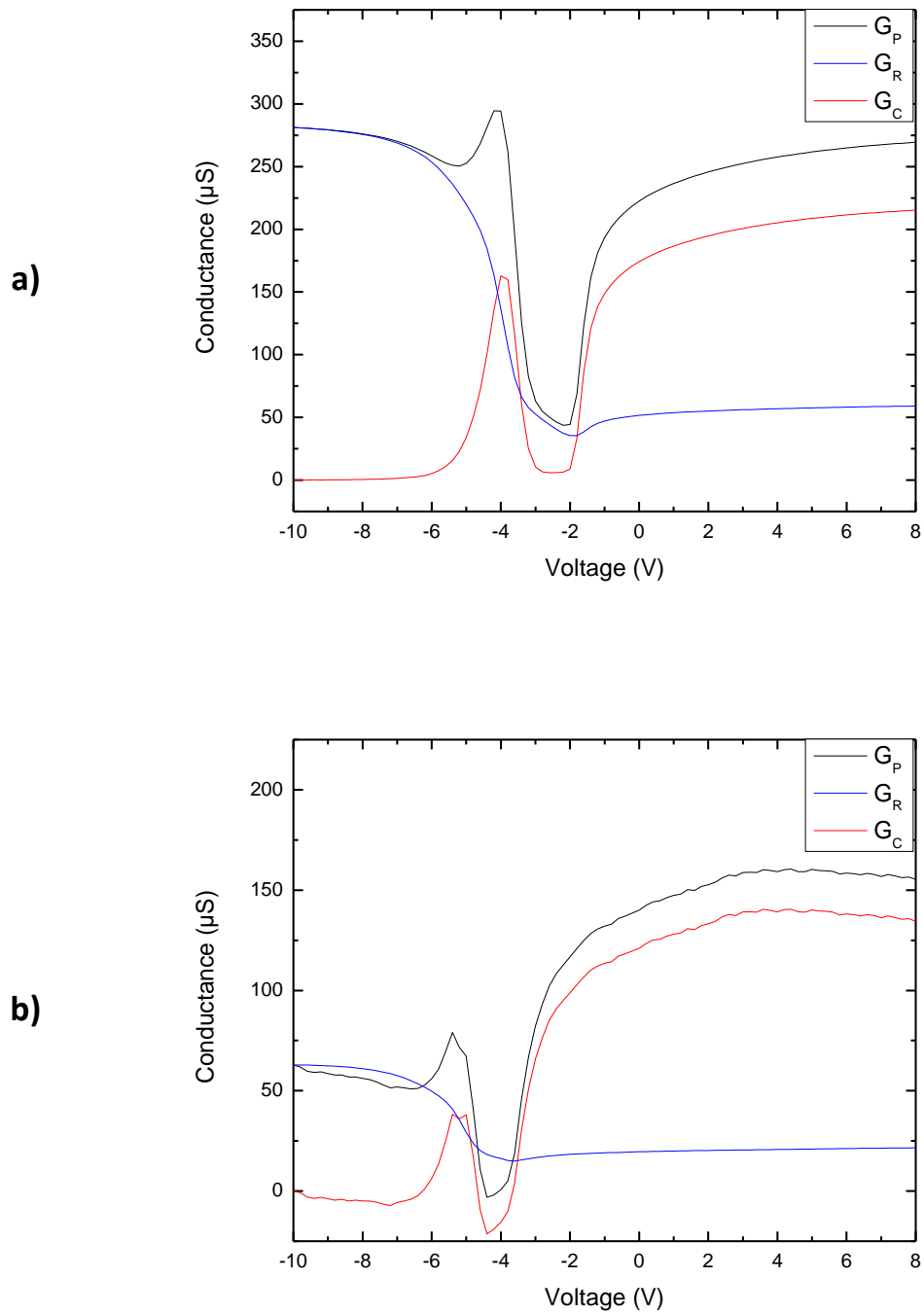
Figure 39: G-V curve showing the result of the analytical method for series resistance correction. G_P is the measured conductance, G_R is the contribution from series resistance and G_C is the corrected conductance. a) sample 51c-1 showing a good fit to the model, and b) sample 54c-2 showing a poor fit to the model.

Due to the insufficient accuracy of the analytical method, the simple linear interpolation was used to determine D_{it}. Uncertainty in the obtained values was determined by detecting maximum and minimum values for the peak magnitude, as illustrated in Figure 40. As can be seen in Figure 38 and Figure 39, for which conductance curves were measured at 10 kHz and 1 MHz, respectively, the measurement frequency influences the shape of the conductance curve. The contribution from series resistance in the accumulation region increases with increasing measurement frequency. When using the linear interpolation method, it is advantageous to have a curve shape similar to the one in Figure 38, because the lower conductance in accumulation makes extraction of the peak magnitude easier. Hence conductance measurements were performed using a frequency of 10 kHz.

For the samples in this work, typical D_{it} values were in the range $1–4×10^{10}$ eV^{-1} cm^{-2}. Compared to the values reported by Aberle, our results are one order of magnitude lower than expected. The values of D_{it} found here suggest an underestimation of the carrier lifetime and a high quality surface. A more probable interpretation is that the conduction method gives underestimated absolute values for D_{it}, but still relative trends should be detectable.
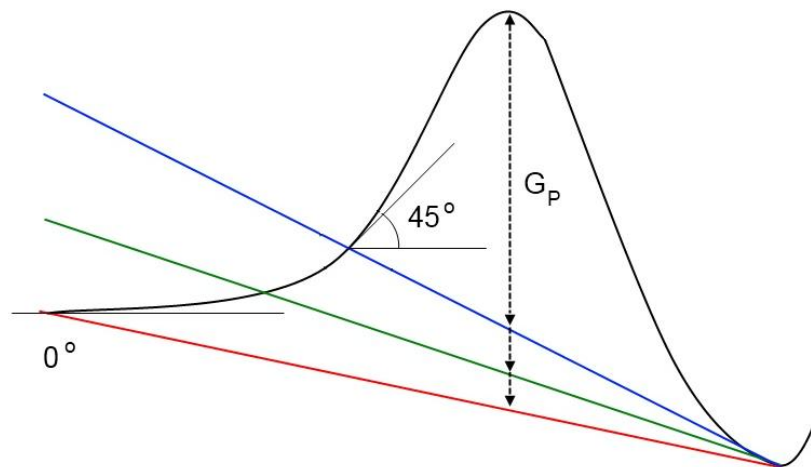
Figure 40: **Uncertainty analysis in the linear interpolation method. The green line is the intermediate value and the blue line intersects the conductance curve where the slope is 45°, giving the lower estimate of the peak conductance. Equivalently, the red line intersects where the conductance curve is flat, giving a higher estimate.**

4.2.3   Quasi-static C-V measurements

Quasi-static C-V measurements were attempted. However, for our samples the recorded curves proved to be difficult to interpret. Measurement noise was a problem for most of the samples, and the shape of the obtained curves did not resemble the expected MIS behavior. However, sample 51c-1 showed some similarity to the idealized case. A combined quasi-static and high frequency C-V plot is given in Figure 41. Although the shape of the quasi-static curve is as expected, some aspects make interpretation and determination of D_{it} difficult. Firstly, the insulator capacitances of the two curves are not identical. The quasi-static curve has $C_i \sim$ 550 pF and the high frequency curve has $C_i \sim$ 350 pF. Secondly, the minimum of the curves are not in the same voltage region. Due to the positive charges in a-SiN$_x$:H, the minimum is expected to be observed for negative voltages, which is the case for the high frequency curve. The quasi-static curve, however, has the minimum at +2.5 V. Hence the curves need to be shifted in both the capacitance and voltage direction for the procedure for determining D_{it} described in Section 2.3.1 to be applicable. Naturally, this would not give accurate estimates of D_{it}, and hence the conductance method is preferred in this work. This offset for the quasi-static C-V measurements compared to the high frequency C-V measurements could be related to errors in the measurement setup or noise.
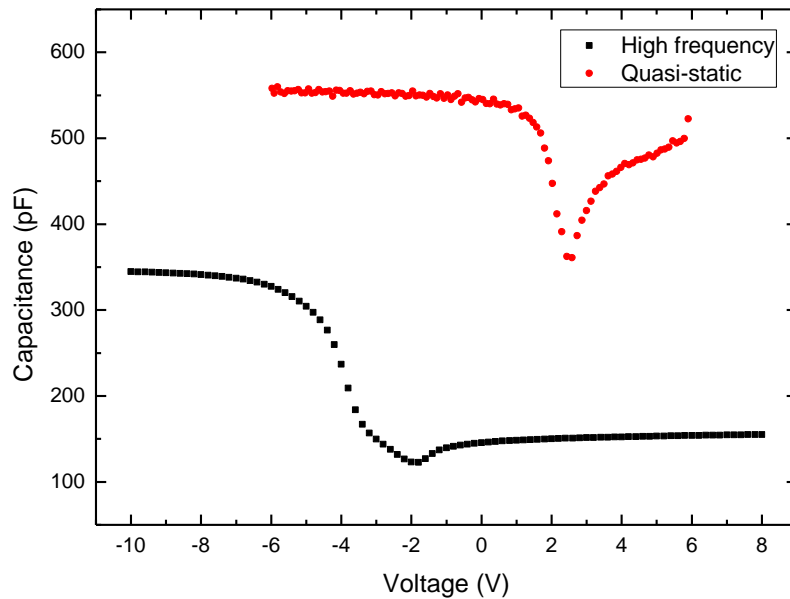
Figure 41:   Combined high frequency and quasi-static C-V curve for sample 52c-1. Both sweeps were conducted from positive to negative voltages. The quasi-static curve is averaged in order to reduce noise.

4.3   Properties of a-SiN$_x$:H by direct PECVD

4.3.1   Optical properties

a-SiN$_x$:H was-deposited on samples 51-57, with varying silane flow, in order to change the gas composition ratio, R = SiH$_4$ / (NH$_3$ + N$_2$). A photography of the resulting thin films on samples 52-57 is given in Figure 42, showing a shift in color from dark blue via turquoise to green with increasing gas flow ratio.
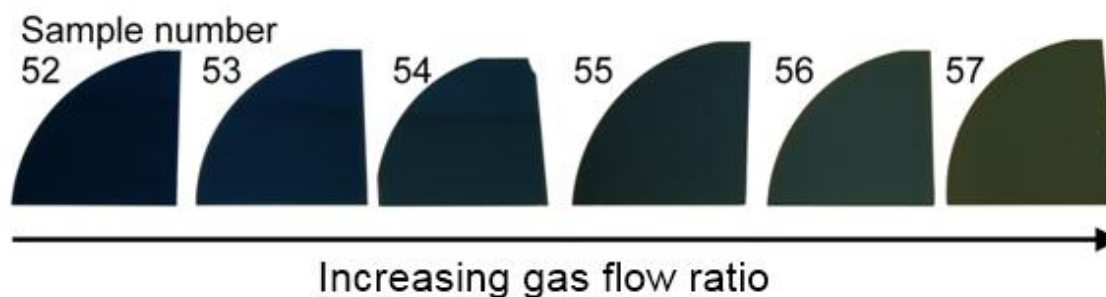
Figure 42:   **Photography of a-SiN$_x$:H thin films deposited with varying gas flow ratio, showing a color shift.**

Film thickness and refractive index were obtained from spectroscopic ellipsometry measurements, and the results are summarized in Table 9. A relatively narrow distribution of film thicknesses in the range 82—98 nm was obtained, by choosing deposition times in accordance with previously measured deposition rates [48]. The films had refractive indices in the range 1.8 to 2.5 at wavelength 630 nm. In Figure 43, the refractive indices are plotted against silane flow and gas flow ratio. Linear regression revealed a linear dependence with a coefficient of determination of 0.998, relating the refractive index n and the gas flow ratio R by the expression

$$n(R) = 1.55 \times 10^{-5} \times R + 1.73 \ .$$

(37)

Table 9:   **Overview of film properties for a-SiN$_x$:H films deposited with varying gas flow ratio.**

Sample number	Silane flow (sccm)	Gas flow ratio SiH$_4$ / (NH$_3$ + N$_2$)	Film thickness (nm)	Refractive index
51	5	0.005	82	1.83
52	10	0.010	93	1.88
53	15	0.015	96	1.95
54	20	0.020	98	2.04
55	30	0.030	95	2.21
56	40	0.040	95	2.36
57	50	0.050	94	2.51

Figure 43: **Refractive index as a function of silane flow and gas flow ratio for a-SiN$_x$:H thin films deposited by direct PECVD. The data are fitted by linear regression.**

The linear dependence of refractive index on gas flow ratio observed here corresponds well to previously obtained results, confirming that refractive index and layer stoichiometry can be controlled by adjusting the gas flows [6, 13, 29-31]. In the rest of this work, refractive index is used as an indication of the layer stoichiometry, and refractive indices in the interval 1.8-1.9 are referred to as N-rich low index films, whereas indices larger than 2.3 are referred to as Si-rich high index films. When depositing a-SiN$_x$:H films of approximately equal thickness, the color of the sample is an indication of its refractive index.

4.3.2 Lifetime measurements

Carrier lifetime measurements conducted by QSSPC resulted in lifetime versus injection level curves, and for simplicity the lifetime extracted at injection level 1×10^{15} cm^{-3} is used as the measure of the effective lifetime. Obtained values for the effective lifetime were in the range 70—350 μs. A previous investigation performed by Haug suggested a bulk lifetime of approximately 800 μs for the silicon wafers used [48]. Calculating the corresponding surface recombination velocities using equation 9 gives estimates of the surface recombination velocity in the range 25—200 cm/s. Since unpassivated silicon has a measured lifetime of ~3 μs, the measured lifetimes of our samples show that the surfaces are well passivated. Comparing the result with the simulated curves in Figure 3, the level of the passivation is very good, corresponding to high cell efficiencies around 22–24 %. The best films deposited here would give a significant improvement in today's industrial solar cells. Still, there is room for further improvements of the passivation properties of the a-SiNx:H deposited in the parallel plate reactor [4].
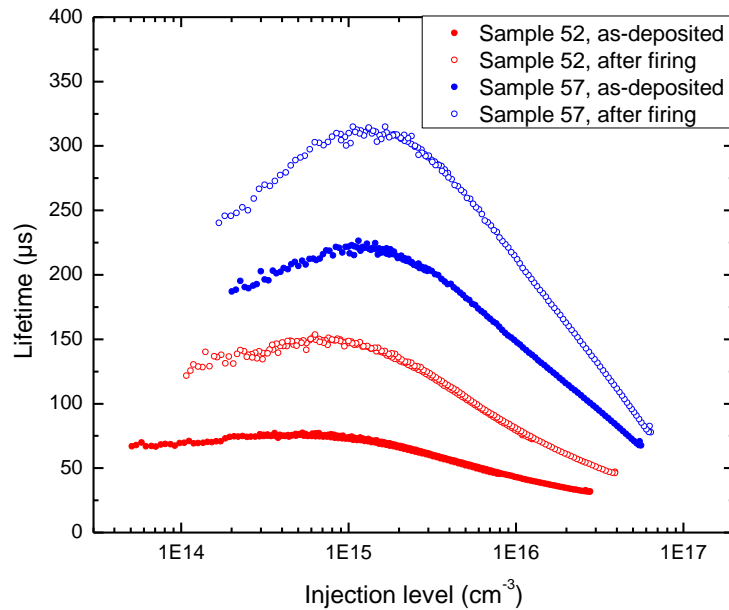
Figure 44: **Lifetime versus injection level curves from QSSPC measurement for samples 52 (*n* = 1.88) and 57 (*n* = 2.51), as-deposited and after firing.**

In Figure 44, the lifetime versus injection level curves of samples 52 (*n* = 1.88) and 57 (*n* = 2.51) are given, for both as-deposited and fired samples. Sample 52 had a lower lifetime than sample 57, and the firing process improved the lifetime of both samples. Extracting the lifetimes at injection level 1×10^{15} cm^{-3} in the high injection curves of samples 52—57 and plotting them against refractive index, reveals a trend where the lifetime increases with refractive index, as shown in Figure 45. For all samples, the lifetime increased after the firing step.

Sample 55 with a refractive index of 2.21 showed a deviation from the trend, with a considerably higher lifetime of 350 µs after firing. Excluding this sample from the linear regression analysis reveals a near linear dependence of lifetime versus refractive index for the other samples, as summarized in Table 10. The observed trend with increasing lifetime with increasing refractive index is in accordance with previous studies of Lauinger et al., Mäckel and Lüdemann and De Wolf et al. [6, 29, 31]. Optimal passivation is achieved for Si-rich films, which is inconsistent with the results of Schmidt and Kerr, who found the optimum surface passivation for films with near stoichiometric composition, with a refractive index of 1.9 [7]. Differences in reactor configuration might be the explanation for this deviation, as Schmidt and Kerr used a remote reactor system.

The increase in lifetime after the heat treatment is in accordance with the observations of Lelièvre et al. [13], except the improvement was observed for all samples in our study, regardless of refractive index. This effect is probably caused by hydrogen passivating dangling bonds, as suggested by Lelièvre et al. [13]. According to Aberle, hydrogen passivation should not be significant in films deposited by high frequency direct PECVD, due to the absence of ion bombardment [4]. The results of this work clearly suggest that both hydrogen passivation and ion bombardment are significant effects for the a-SiNx:H films deposited in our PECVD reactor. A possible explanation of the deterioration of the passivation observed by Aberle, De Wolf et al. and Lenkeit et al. might be that process parameters during deposition or firing inhibit the diffusion of hydrogen to the Si/a-SiN$_x$:H interface and into the Si substrate, and instead cause hydrogen to evaporate [4, 14, 29]. This indicates the importance of optimizing the fabrication process to achieve good passivation. Hong et al. observed a larger improvement in passivation for silicon rich samples [38], whereas our experiments showed equally large increases in lifetime for all refractive indices. The data presented here do indeed display a slightly higher slope for the linear fit of the fired samples, approximately 3 % larger than for as-deposited samples. However, this difference is too small to conclude in accordance with the observations of Hong et al.
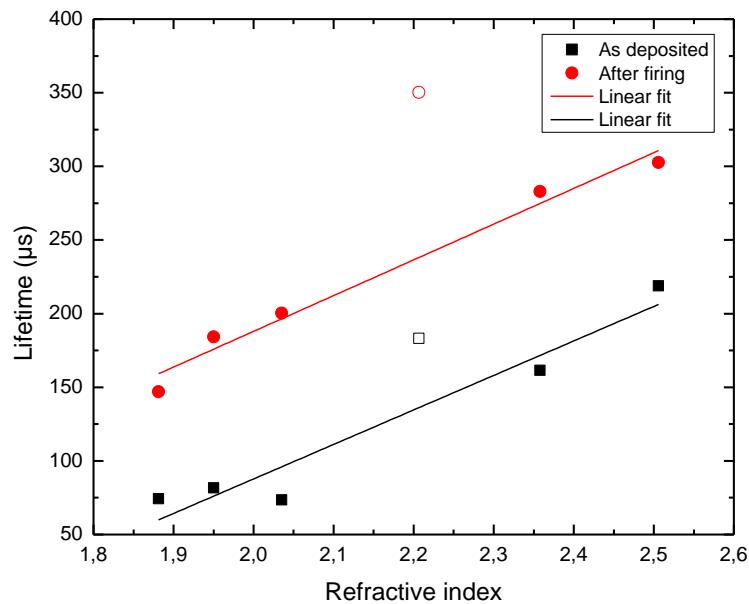
Figure 45: **Lifetime at injection level 1×10^{15} cm^{-3} for high injection measurement versus refractive index for samples 52—57 for as-deposited and fired samples. Sample 55 (n = 2.21, open symbols) showed a deviation from the linear trend observed for the other samples, and is not included in the linear fit.**

Table 10: **Result from linear regression of lifetime versus refractive index for samples 52-54 and 56-57, y=ax+b.**

	Slope, a (µs)	Intercept, b (µs)	Coefficient of determination, r^2
As-deposited	234	-381	0.923
After firing	242	-297	0.972

In order to investigate whether the high lifetime of sample 55 was due to the wafer or an actual improvement in the passivating layer, the same recipe was repeated two weeks later on the same wafer (sample 55d) and a control wafer (sample 56d) simultaneously. These had been cleaned with RCA-1 and RCA-2 two weeks before, and received a HF dip prior to deposition. The measured lifetimes at injection level 1×10^{15} cm^{-3} are given in Table 11. The lifetime of both sample 55d and 56d was lower than the original (Sample 55a), which indicates that the cleaned surfaces degrade after cleaning when stored. Still, the lifetime of sample 56d was 11 µs lower than for sample 55d. Because the films were deposited simultaneously, they should be identical, and the experiment indicates a higher quality of the 55 substrate compared to 56. Originating from the same batch of wafers, it is more likely that the difference in substrate quality is caused by variances in the substrate preparation than material quality. One possible explanation of the higher quality of sample 55 is the stacking of wafers in the cleaning cassette. If wafer 55 was placed at the edge of the cassette, it would be exposed to larger volumes of chemicals during cleaning than the wafers stacked in the middle of the cassette.

Table 11: **Lifetimes of as-deposited a-SiN$_x$:H samples with gas flow ratio 0.030, repeated on different wafers.**

Deposition	Sample number	Lifetime (µs)
Original sample	55a	183
Repeated at the same wafer	55d	101
Repeated at control wafer	56d	90

4.3.3　　Fixed charge densities

Capacitance-voltage curves at 1 MHz were recorded in order to estimate fixed charge density of the a-SiN$_x$:H films with different refractive indices. However, the differences in film composition were reflected in C-V curves, showing several deviations from the idealized MIS capacitor characteristics. 3 voltage sweeps were performed on each sample. Sweep 1 started at zero in order to estimate the initial charge distribution in the film, and sweep 2 was done to check the effect of the previous sweep on the sample. Sweep 3 was conducted to investigate whether soaking had an effect on the measurement.

C-V curves of samples with three different refractive indices are given in Figure 46a-c. The C-V curve for the as-deposited version of sample 51 with a refractive index of 1.83 is given in Figure 46a. Similar behavior was observed for the other samples with low refractive indices, in the range 1.83—1.95, for both as-deposited and fired films. Experiments showed that measurement history had little effect on capacitance, as only a very small shift in the curve was observed for the different sweeps. In Figure 46b the C-V characteristic of sample 55 after firing (n = 2.21) is given. A shift in the curve is observed for consecutive measurements, as well as for the measurement starting with a soaking at 8 V. This effect was observed for samples with intermediate to high refractive index, both as-deposited and after firing. Figure 46c shows the C-V curve of the as-deposited version of sample 57 (n = 2.51) exhibiting a slightly smaller capacitance shift, in addition to a tilt which indicates leakage currents preventing capacitance saturation.
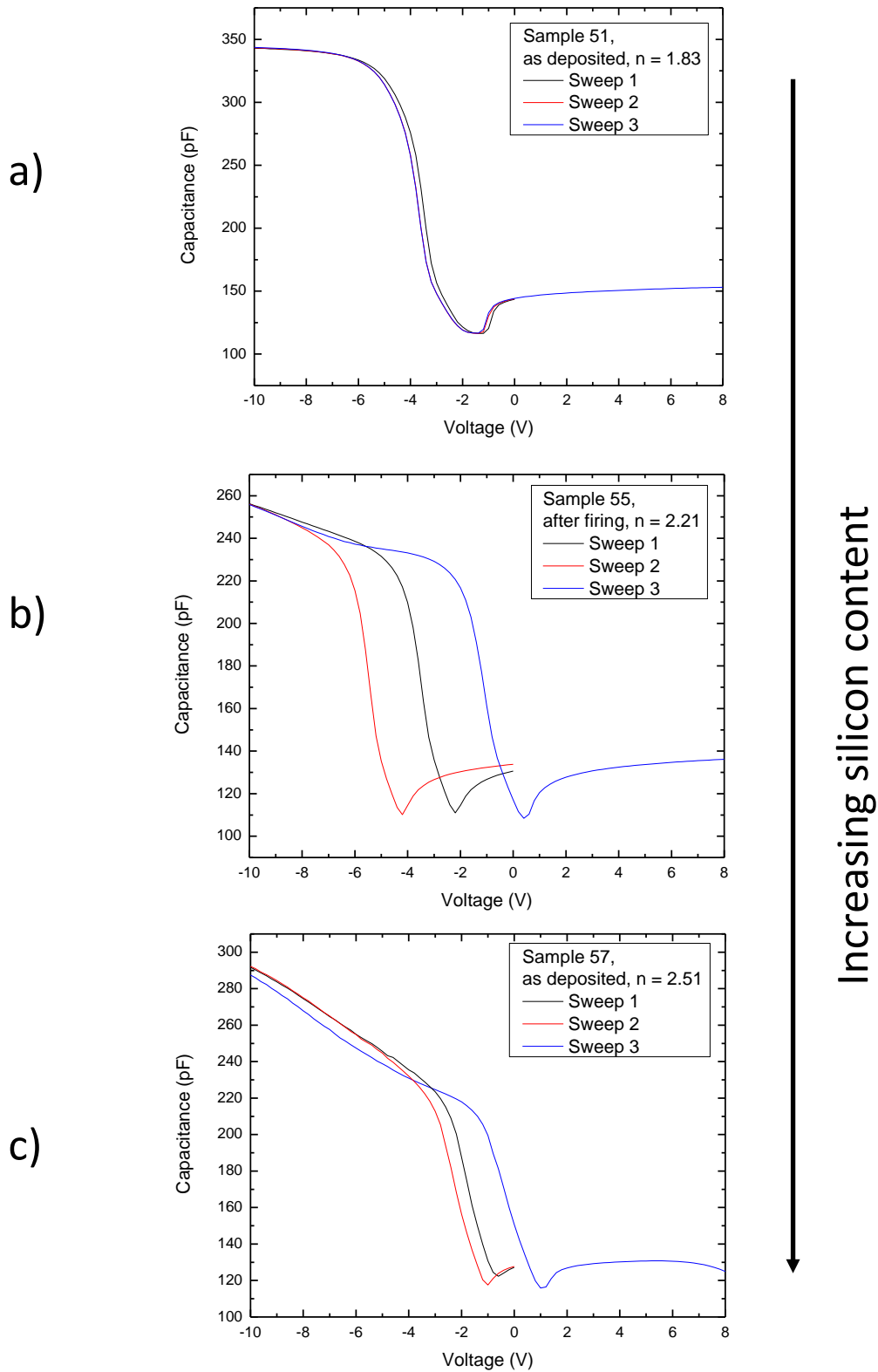
Figure 46: **C-V curves at 1 MHz for samples with increasing refractive index and silicon content: a) as-deposited version of sample 51 with *n* = 1.83, b) Fired version of sample 55 with *n* = 2.21 and c) as-deposited version of sample 57 with *n* = 2.51. Sweep 1 and Sweep 2 were from 0 V to -10 V, and Sweep 3 was from 8 V to -10 V.**

Further analysis of the C-V curves gives estimates of flat band voltage and fixed charge density, using equations 13—17. The non-ideal effects complicate the determination of these parameters, as flat band voltage is shifted with the C-V curve, and the insulator capacitance is difficult to determine in presence of large leakage currents. Calculating the shifts in flat band voltage for samples of varying refractive index gives an indication of the impact of measurement history on the C-V characteristic of the sample. Shifts in flat band voltage are interpreted as changes in the fixed charge distribution in the film, caused by charging of K-centers. In Figure 47, the absolute values of the shifts in flat band voltage obtained by C-V measurements on samples 51-57 are given, averaged over both as-deposited and fired samples. Experiments show that the samples with intermediate refractive index show the largest dependence of measurement history. Hence the concentration of chargeable K-centers is larger in these a-SiN$_x$:H films. A summary of the non-ideal effects observed in C-V measurements for samples with different refractive indices, and their impact on further analysis is given in Table 12.
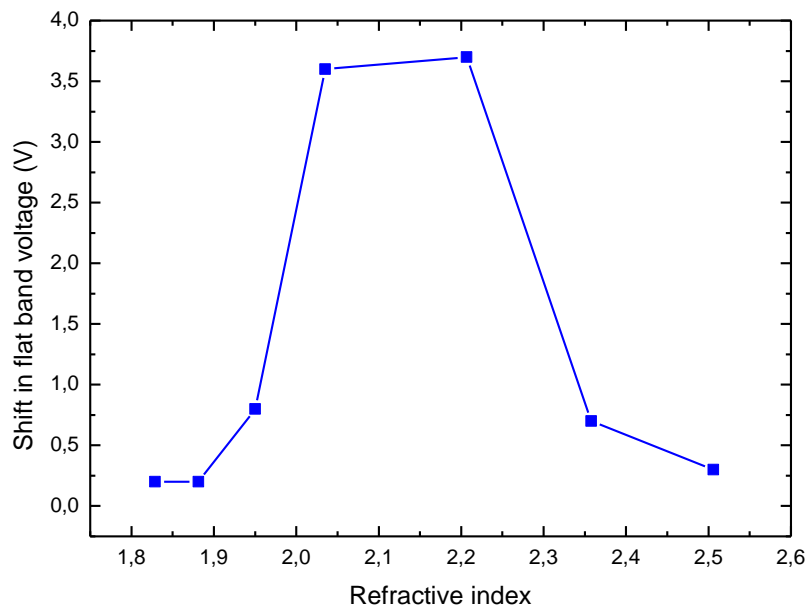
Figure 47: **Absolute value of the shift in flat band voltage, representing the shifts in the C-V curve with measurement history, as a function of refractive index. The obtained values are averaged over one fired and one as-deposited sample.**

Compared to the observations of Beylier et al. and De Wolf et al., our observations are in accordance with the observed decrease of hysteresis effects and voltage shifts with increasing refractive index in the intermediate to high refractive index region [15, 29]. Additionally, the decrease in flat band voltage shifts observed for lower refractive indices is in accordance with the observations of Lau et al.[35]. This emphasizes that the nature of hysteresis effects and curve shifts greatly depend on Si/N stoichiometry, hydrogen content and refractive index,

which again vary with deposition method. Nevertheless, our experiments suggest that it is probable that hysteresis effects and measurement history dependence are more dominating for intermediate refractive index and stoichiometry.

The leakage currents observed for higher refractive indices correspond well to the effects reported by of Beylier and De Wolf [15, 29]. This is as expected, because the band gap decreases as the nitrogen content decreases, from stoichiometric silicon nitride to amorphous silicon. As the refractive index increases, the band gap decreases, and hence the leakage current increases.

Table 12:   Overview of non-ideal effects in C-V measurements on Al/a-SiN$_x$:H/Si structures

Effect	Observed for	Affects determination of
Shifts in C-V curve with measurement history	2.0 < n < 2.3	Flat band voltage
Leakage currents	n > 2.3	Insulator capacitance in accumulation

A plot of the obtained values for Q_f as a function of refractive index, for the three different sweeps is given in Figure 48. The obtained values for Q_f are in the range $1–9\times10^{11}$ cm^{-2}, which is high compared to literature [4]. This can be explained by the fact that the obtained values are not only from the first sweeps, and as measurements proceed, the flat band voltage is shifted towards more negative values resulting in higher values of Q_f. No trend with respect to refractive index, firing treatment or sweep number is observed, due to the non-ideal effects. Hence using C-V measurements on a series of samples with such different electric properties to determine the fixed charge density is difficult.

In order to explore the origin of the non-ideal response in the C-V measurements on nitrides with intermediate to high refractive index, a stack of high index – low index silicon nitride was-deposited using high (0.050) and low (0.010) gas flow ratio. According to the results presented in Figure 43, the stack should consist of high index a-SiN$_x$:H (n ~2.5, thickness ~50 nm) bottom layer and low index a-SiN$_x$:H (n ~1.9, thickness ~50 nm) top layer. A C-V curve from this sample is given in Figure 49, where the shift with measurement history is still observed and the leakage current is eliminated. This indicates that the origin of the shifts is connected to charging in the interface between silicon and a-SiN$_x$:H, and confirms that leakage current is a feature of Si-rich films.
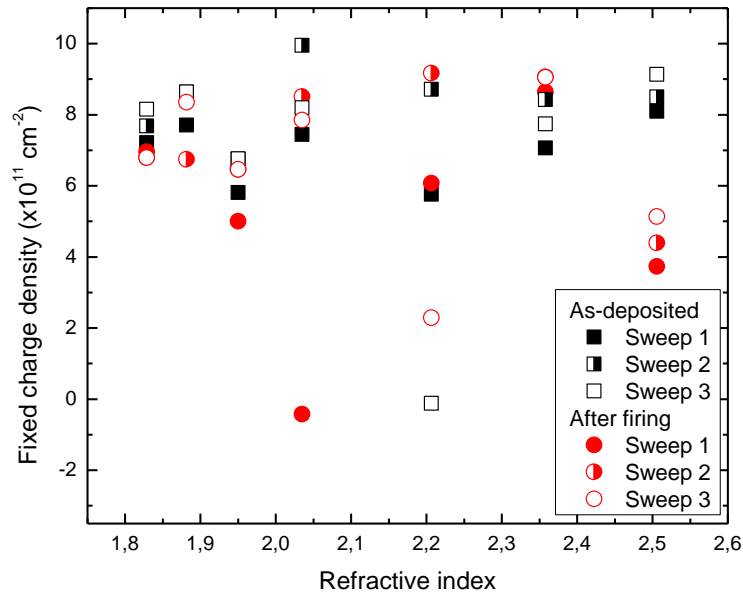
Figure 48: **Fixed charge density versus refractive index for samples 51-57, showing data from three voltage sweeps: Sweep 1 from 0 V to -10 V, Sweep 2 from 0 V to -10 V and Sweep 3 from 8 V to -10 V. Data for both as-deposited and fired samples are included.**
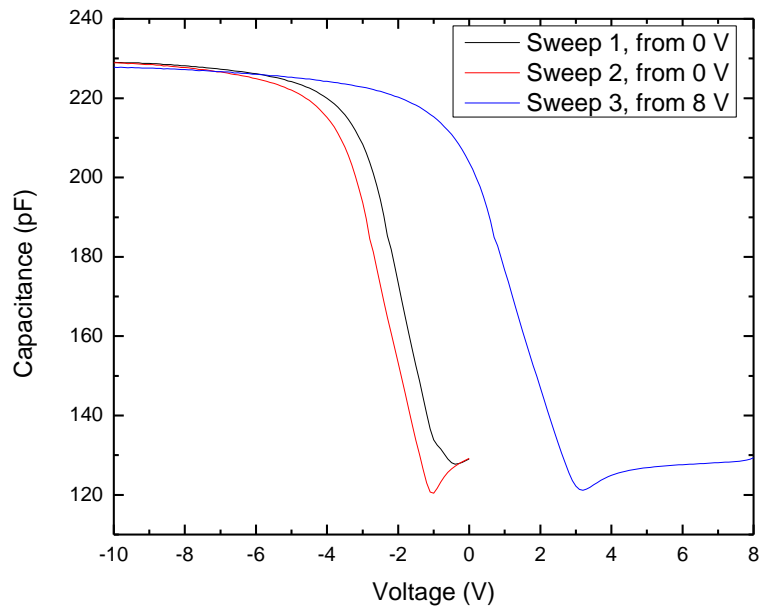
Figure 49: **C-V curve of a-SiN$_x$:H /a-SiN$_x$:H stack with refractive indices 2.5 and 1.9 at the bottom and top layer, respectively. The shift with measurement history is still present, but the leakage current tilt is not observed in the C-V characteristics.**

4.3.4   Density of interface traps

Two methods were attempted in order to determine the density of interface traps of the a-SiN$_x$:H samples: Conductance-voltage (G-V) and conductance-frequency (G-f) measurements.

G-V measurements were performed successfully on all samples in the silane variation series (Set 1), both as-deposited and fired. The magnitude of the conductance peak was found by the linear interpolation method, and the obtained values were in the range 1—4×10^{10} eV^{-1}cm^{-2}. In Figure 50, the obtained values are plotted against refractive index. Error bars were obtained by performing 3 linear interpolations per curve, as described in Section 4.2.2. A decrease in D_{it} with increasing refractive index is observed, which indicates that the chemical passivation is better for silicon rich films. This could be caused by a higher concentration of hydrogen which saturates dangling bonds. Additionally, D_{it} decreases after firing, which supports the hypothesis that diffusing hydrogen passivates recombination centers during firing.
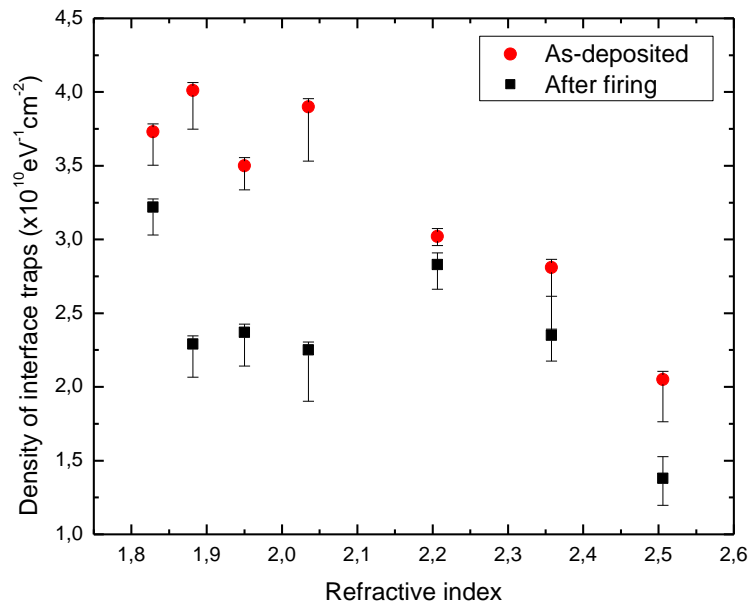
Figure 50: **D_{it} for different refractive indices, for as-deposited and fired films. The conductance method with linear interpolation is used, and the error bars are obtained by the approach outlined in Figure 40.**

G-f measurements were successfully performed on samples 51-53, with low refractive indices. For the samples with higher refractive indices, the position of the depletion region was difficult to locate due to shifting of the curve with measurement history, and hence measurement attempts were unsuccessful. Graphs showing the obtained curves for as-deposited versions of sample 51-53 are given in Figure 51. The peak conductance was used to determine D_{it}, using equation 23. In Table 13, the applied voltages and calculated densities of interface states are summarized, together with the corresponding values from the G-V analysis. D_{it} values in the

range 3.9—4.8×10^{10} eV^{-1}cm^{-2} were found, which is slightly higher than the values found by G-V measurements. This is caused by the fact that the chosen frequency for the G-V measurements was 10 kHz, whereas the peak conductance is found in the interval 20—50 kHz, as shown in Figure 51.
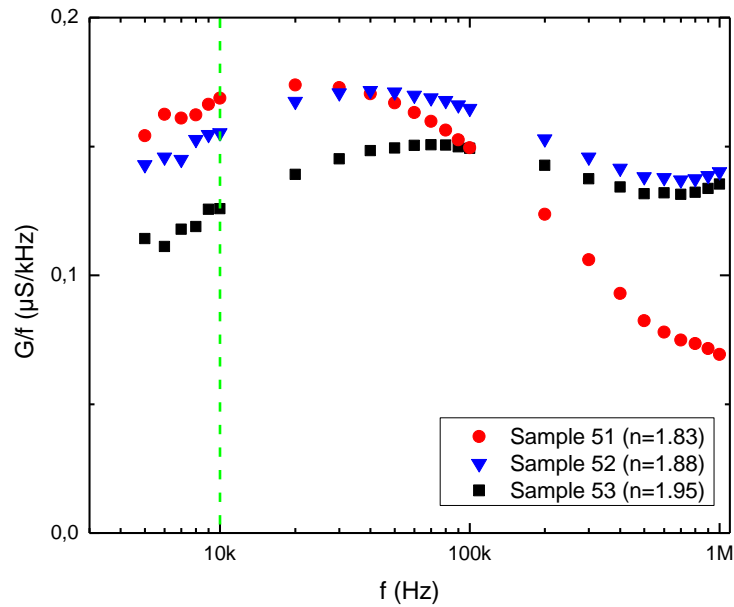
Figure 51: Normalized conductance versus frequency for as-deposited samples 51-53 with low refractive indices. The green line at 10 kHz indicates the chosen frequency for G-V measurements.

Table 13: Values for refractive index, depletion voltage and density of interface traps for as-deposited samples 51-53.

Sample	Refractive index	Voltage (V)	D_{it} from G-f (eV^{-1} cm^{-2})	D_{it} from G-V (eV^{-1} cm^{-2})
51	1.83	-3.0	4.8×10^{10}	3.2×10^{10}
52	1.88	-3.5	3.9×10^{10}	2.3×10^{10}
53	1.95	-4.0	4.4×10^{10}	2.4×10^{10}

4.3.6   Stability
Degradation of a-SiNx:H deposited on float zone silicon substrate

The stability of the a-SiN$_x$:H thin films towards solar irradiation was tested by illuminating samples using a solar simulator. Float zone silicon is known to be stable towards illumination, and hence any degradation observed would be related to degradation of the a-SiNx:H passivation layer. The stability test was conducted on sample 45 (n = 2.04 and d = 98 nm), both for the as-deposited thin film and after firing. Lifetimes at injection level 1×10^{15} cm^{-3} from high injection curves are plotted against illumination time in Figure 52.
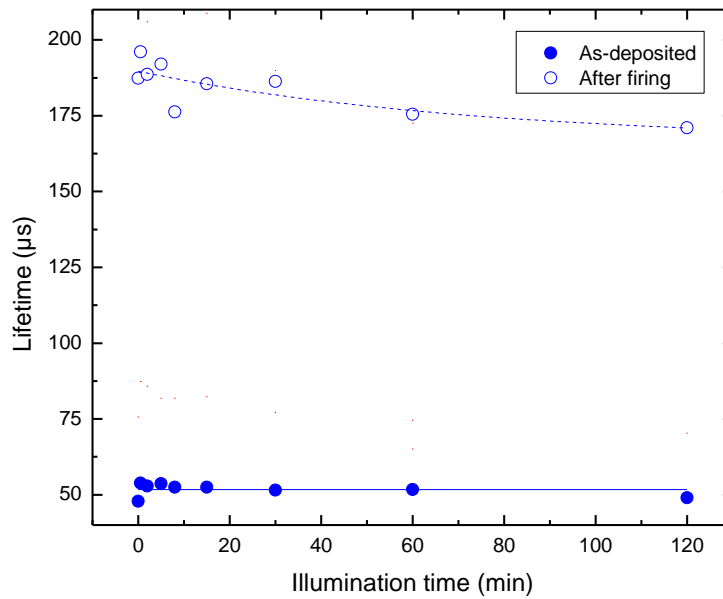
Figure 52:   Lifetime at injection level 1×10^{15} cm^{-3} versus illumination time for sample 45 on FZ silicon (n = 2.04 and d = 98 nm), both for the as-deposited thin film and after firing.

Lifetime degradation was observed, and the reduction in lifetime was larger after firing. The trend is less distinct for the as-deposited sample, as the measurement uncertainties become more significant with lower lifetime.

The data were fitted to an exponential decay model on the form

$$\tau(t) = \tau_\infty + A e^{-t/T}$$

(38)

where τ *(t)* is the illumination time dependent lifetime, *A* is a constant, *T* represent the decay rate and τ_∞ is the saturation lifetime. The initial effective measured lifetime, τ_0 is given by

$$\tau_0 = \tau_\infty + A$$

(39)

The coefficients are given in Table 14, and the obtained functions are plotted along with the experimental data in Figure 52. The model fits well with the data obtained for the fired sample and is affected by measurement uncertainties for the as-deposited sample with lower lifetime, giving a time constant approaching infinity.

Table 14: **Coefficients from exponential decay data fit of lifetime versus illumination time data for a-SiN$_x$:H deposited on FZ substrate (sample 45). *A* is a constant, *T* is the decay rate and τ_∞ is the saturation lifetime.**

As-deposited			After firing		
τ_∞ (μs)	A (μs)	T (min^{-1})	τ_∞ (μs)	A (μs)	T (min^{-1})
51	0.85	∞	166	23	73

In order to estimate the degree of degradation in the passivation layer, the fired sample is used. From equation 9, the initial effective measured lifetime is given by the contributions from bulk and surface recombination according to

$$\frac{1}{\tau_0} \approx \frac{1}{\tau_{bulk}} + \frac{2S_0}{W} \tag{40}$$

where S_0 is the initial SRV. By assuming a bulk lifetime of 2 ms and using the coefficients in Table 14, S_0 = 72 cm/s is found. Since there is negligible lifetime degradation for FZ silicon, the bulk lifetime is constant and the relative degradation of the passivation properties is given by the increase in SRV, *x*. Hence, the saturation lifetime and degradation is described by the relation

$$\frac{1}{\tau_\infty} \approx \frac{1}{\tau_{bulk}} + \frac{2xS_0}{W}. \tag{41}$$

For sample 45 after firing, an *x*-value of 1.15 is found, representing an increase in the SRV of 15 % for the a-SiN$_x$:H film after illumination. This corresponds to a relative decrease in the effective measured lifetime of 12 %.

Degradation of a-SiNx:H deposited on Czochralski silicon substrate

Samples 52-57 with varying refractive index were deposited on Czochralski (Cz) material, and when performing stability experiments on these samples, bulk degradation must also be taken into account. Light induced degradation is a known phenomenon in boron doped Czochralski silicon, where the bulk lifetime is reduced when the material is exposed to radiation [49].

For samples 52-57, both as-deposited and fired, the stability towards solar irradiation was tested. Lifetimes at injection level 1×10^{15} cm^{-3} from high injection curves are plotted against illumination time for as-deposited and fired samples of different refractive indices in Figure 53. In Figure 54, lifetime versus refractive index is plotted for illumination times of 0 and 120 minutes. Some degradation was observed for all samples, and the degradation increased with increasing refractive index and after firing. The degradation trends showed a rapid decrease in lifetime from 0 to 30 minutes, and saturation was observed after 2 hours. The trends were less distinct for samples with low refractive index, as the measurement uncertainties become more significant with lower degradation. From Figure 54 it can be seen that the trend of linearly increasing lifetime with refractive index is still valid after 2 hours illumination.

a)   **b)**
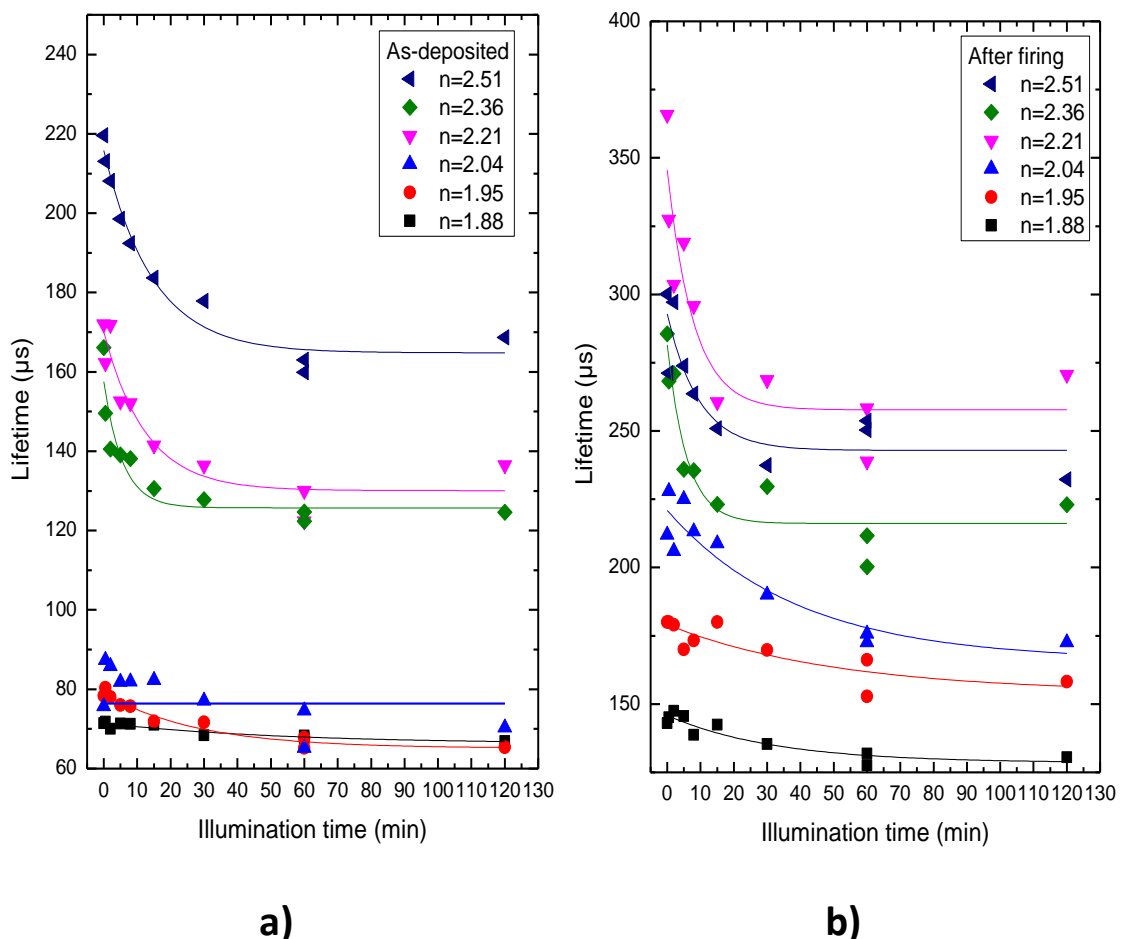
Figure 53: **Lifetime at injection level 1×10^{15} cm^{-3} versus illumination time for a) as-deposited and b) fired samples of varying refractive index. The lines are obtained by fitting the data to an exponential decay model.**

The data were fitted to the exponential decay model, and the resulting coefficients are given in Table 15. In Figure 53, the obtained functions are plotted together with the experimental data. The model fits well with the high refractive index samples, and is affected by uncertainties of the measurements for low refractive index samples with lower lifetimes. Especially sample 54 shows an improbable improvement in lifetime for the as-deposited film due to scattered data.

Table 15: **Coefficients from exponential decay data fit of lifetime versus illumination time data. *A* represents the decay size, *T* is the decay rate and τ_∞ is the saturation lifetime.**

Sample number	Refractive index	As-deposited			After firing		
		τ_∞ (μs)	A (μs)	T (min^{-1})	τ_∞ (μs)	A (μs)	T (min^{-1})
52	1.88	66	5.2	53	129	17	32
53	1.95	65	14	28	154	25	51
54	2.04	76	-0.58	0.0026	166	55	39
55	2.21	130	40	12	258	88	7.9
56	2.36	126	32	5.6	216	65	5.9
57	2.51	165	51	15	243	50	9.5

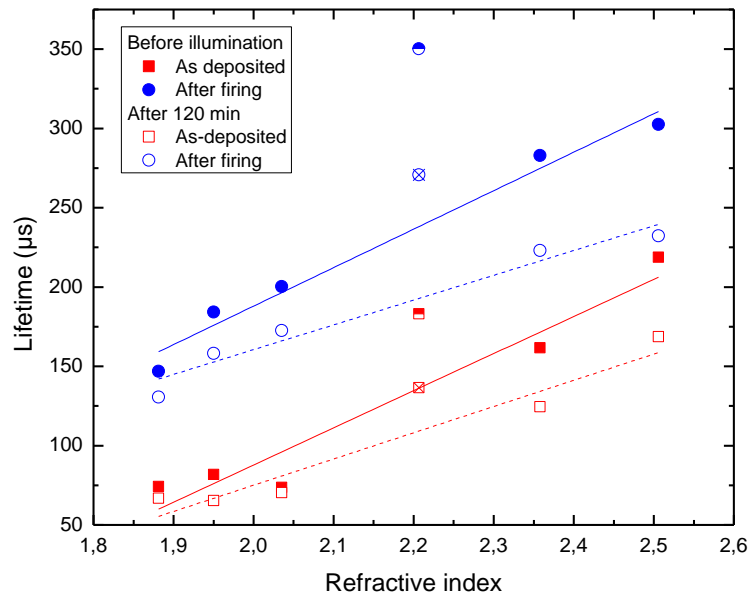**Figure 54:** **Lifetimes at injection level 1×10^{15} cm^{-3} versus refractive index for as-deposited and fired samples before illumination and after 2 hours under the solar simulator. The lines represent linear fits, and the data points for *n* = 2.2, marked by crossed and half-filled symbols, are left out from the determination of the linear trend.**

Experiments showed that even though Si-rich samples have the best passivation properties, they also have a larger reduction in lifetime when exposed to light. A smaller time constant observed for Si-rich films demonstrates a more rapid degradation as well. Furthermore, the increased lifetime gained by firing is to some extent lost again when the sample is exposed to light. Even though heat treated Si-rich films have the largest loss in lifetime, their passivation properties are still better than for N-rich films, as can be seen in Figure 54.

In order to interpret these results, it is necessary to separate the degradation of the passivation layer from degradation in bulk silicon. Samples 54 and 45 have the same deposition parameters, and hence the passivation film should be identical for the two samples. By assuming an identical increase in the SRV for the two samples, an estimate of the bulk degradation in CZ silicon can be made. The initial surface recombination velocity of sample 54 of S_0 = 49 cm/s is found using equations 39—40, the coefficients from the fitted data and a bulk lifetime of 800 μs [48]. Modifying equation 41 by including a relative bulk degradation, y, gives an expression for the saturation lifetime in Cz samples:

$$\frac{1}{\tau_\infty} \approx \frac{1}{y\tau_{bulk}} + \frac{2xS_0}{W}.$$

(42)

A bulk degradation of 0.55 is found, indicating a reduction of 45 % of the bulk lifetime in the Czochralski substrate, which is equivalent to a reduction in bulk lifetime from 800 μs to 440 μs.

By using this value for the bulk degradation, and assuming an equal degradation for all CZ samples, the relative increase in SRV can be found. For samples 52-57, both as-deposited and fired, the degradation in the passivation layer is given in Figure 55a. The resulting values give a change in SRV in the interval from -8 % to +17 %. It is clear that these results are non-physical, as an improvement in the passivation properties, reflected in a decrease in SRV, is not likely.

One possible explanation is an underestimation of the bulk lifetime in the CZ material. As an upper limit, an initial bulk lifetime of 2 ms and a degraded lifetime of 1.1 ms are assumed. The resulting values for the degradation in the passivation layer are given in Figure 55, and a change in SRV ranging from -0.4 % to +25 % is found. If the degradation stabilizes after 2 hours of illumination, the quality of the passivation layer still is satisfactory for use in solar cells.

A larger degradation for films with intermediate to high refractive index is observed from the plots in Figure 55b, and the fired films appear to be more stable than the as-deposited films. The as-deposited version of sample 54 (n = 2.04) did not fit well to the exponential decay model, explaining the negative value of the change in SRV in Figure 53.
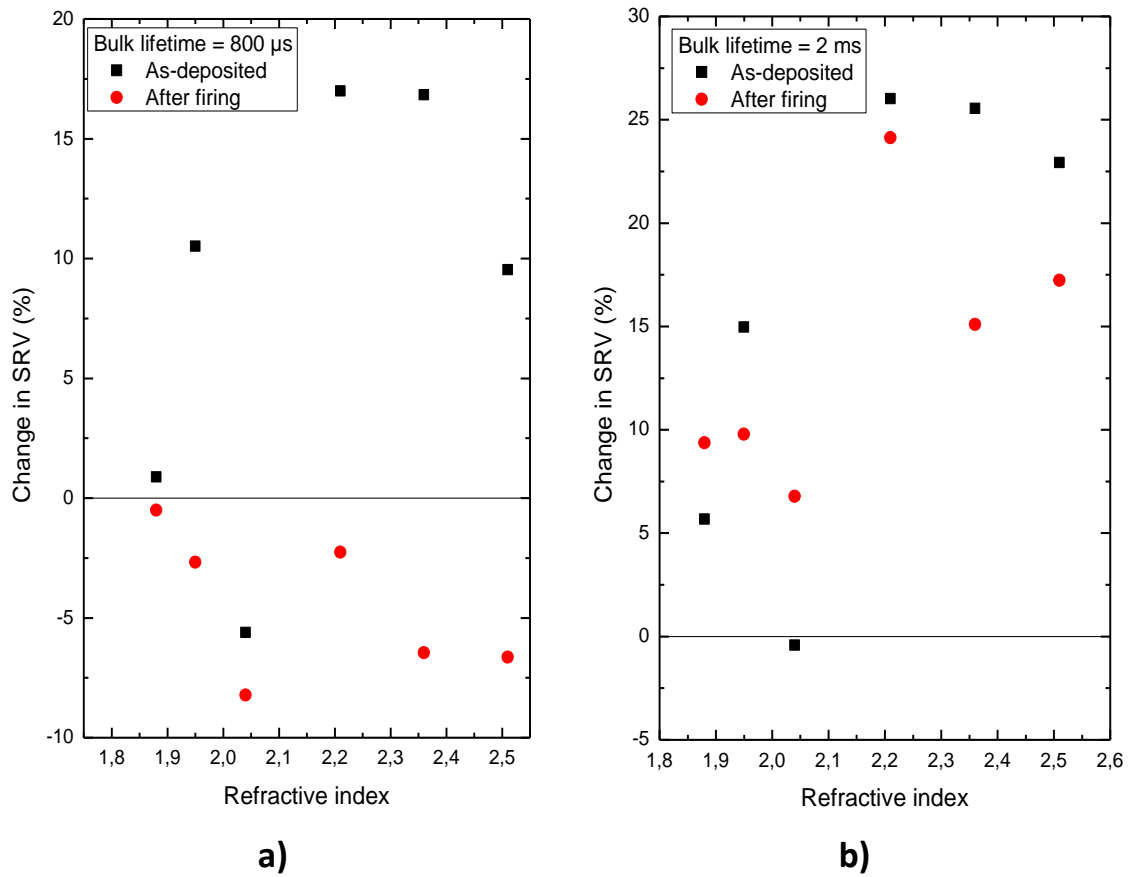
Figure 55: **Change in SRV (in %) after 2 hours of illumination for Cz samples with bulk lifetimes of a) 800 µs and b) 2 ms.**

4.3.7   Summary direct PECVD a-SiN$_x$:H

Experiments revealed some trends with respect to the properties of a-SiN$_x$:H layers of varying stoichiometry, and the key properties of samples 51-57 are summarized in Table 16.

Adjusting gas flow ratios proved to be an effective way of controlling layer stoichiometry. The refractive index of the film and hence the silicon content increased linearly with increasing gas flow of silane. Increasing effective measured lifetimes with increasing refractive index indicated that the overall passivation properties were best for Si-rich films. Firing improved the lifetime of all samples, and the increase in lifetime after firing was largest for Si-rich films.

Electrical characterization of the samples was attempted in order to separate the contributions from chemical and field-effect passivation on the lifetime trends. A decrease in D_{it} with increasing refractive index, as well as a significant reduction in D_{it} after firing show that the degree of chemical passivation is highest for Si-rich films, and that firing caused an improvement in the chemical passivation for all samples. These observations can be related to the diffusion of hydrogen, saturating dangling bonds and decreasing D_{it}, and suggest a larger hydrogen concentration in Si-rich films. Large quantities of positive fixed charges in the a-SiN$_x$:H films were detected by C-V measurements. However, estimating the contribution from field-effect passivation on the films of varying stoichiometry, proved to be difficult due to non-ideal effects in C-V characteristics. Leakage currents were most pronounced for Si-rich films. Shifts in the C-V characteristics, indicating charging of K-centers in the film, were most dominating for films of intermediate composition (2.0 < n < 2.3).

Based on the results of these investigations, Si-rich films should be used for surface passivation due to their superior passivation properties. For use as front side passivation in a solar cell, the layer also has to function as an effective anti-reflection coating. Hence there is a trade-off between excellent surface passivation and an optimum anti-reflection coating with low absorption and reflection. Additionally, our experiments suggest that the Si-rich films are more unstable towards illumination, and accordingly, some of the passivation properties will degrade with time.

Table 16: Summary of properties of a-SiN$_x$:H deposited by direct PECVD. *d* is the film thickness, *n* is the refractive index, τ_{eff} is the effective measured lifetime, Q_f the fixed charge density, D_{it} the density of interface traps, and x_{max} the maximum increase in SRV after light exposure. The films are categorized by composition according to refractive index.

Sample number	*d* (nm)	*n*	*Comp.*	τ_{eff} (µs) As-dep.	τ_{eff} (µs) Fired	Q_f (×10^{11} cm^{-2})	D_{it} (×10^{10} eV^{-1}cm^{-2}) As-dep.	D_{it} (×10^{10} eV^{-1}cm^{-2}) Fired	x_{max} (%)
51	82	1.83	N-rich	—	—	6.8—8.2	3.5—3.8	3.0—3.3	—
52	93	1.88	N-rich	74	147	6.7—8.6	3.7—4.1	2.1—2.3	9
53	96	1.95	N-rich	82	184	5.0—6.8	3.3—3.6	2.1—2.4	15
54	98	2.04	Inter-mediate	74	200	-4.3—10	3.5—4.0	1.9—2.3	7
55	95	2.21	Inter-mediate	183	350	-1.1—9.2	3.0—3.1	2.7—2.9	26
56	95	2.36	Si-rich	162	283	7.1—9.1	2.4—2.9	2.2—2.6	26
57	94	2.51	Si-rich	219	303	3.7—9.1	1.8—2.1	1.2—1.5	23

4.4   Properties of a-SiN$_x$:H by remote PECVD

4.4.1   Optical properties

a-SiN$_x$:H was-deposited on samples 1-4, using a remote expanding thermal plasma system. The gas composition ratio, R = SiH$_4$/NH$_3$ was varied in order to obtain films of different composition. A picture of the resulting thin films is given in Figure 56, showing a shift in color from purple via blue to brown as the gas flow ratio increased.

Increasing gas flow ratio (SiH$_4$/NH$_3$)
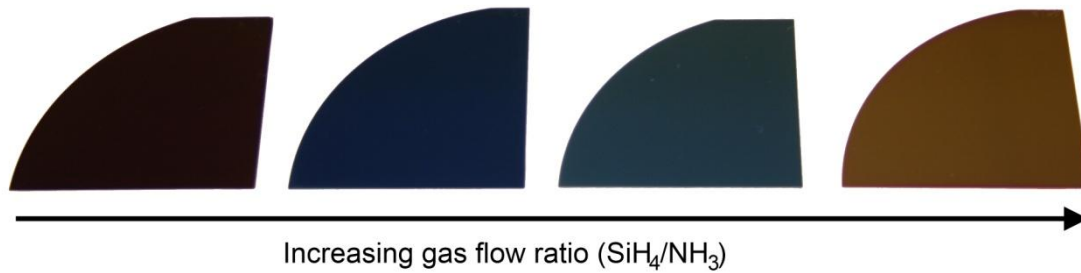
Figure 56:   Photography of a-SiN$_x$:H thin films deposited with varying gas flow ratio, showing a color shift.

In Table 17, the gas flow ratio (averaged over the three plasma sources), measured refractive indices, film thicknesses and calculated deposition rates are summarized. The films had refractive indices in the range 1.9—2.5 at wavelength 630 nm, and the refractive indices are plotted against gas flow ratio in Figure 43. Linear regression revealed a linear dependence with a coefficient of determination of 0.942, relating the refractive index n and the gas flow ratio R according to

$$n(R) = 1.96 \times R + 1.66 \ .$$

(43)

Table 17:   Overview of film properties for a-SiN$_x$:H films deposited by remote PECVD with varying gas flow ratio.

Sample number	Gas flow ratio (SiH$_4$/NH$_3$)	Film thickness (nm)	Deposition rate (nm/s)	Refractive index
1	0.108	68	2.30	1.92
2	0.181	85	2.86	1.98
3	0.301	89	2.99	2.19
4	0.421	135	4.53	2.53

The linear dependence of refractive index on gas flow ratio observed here corresponds well to the findings in Section 4.4.1 for direct PECVD and results reported in literature [6, 13, 29-31]. Hence adjusting the gas flow ratio in remote PECVD is a method for controlling the layer stoichiometry.
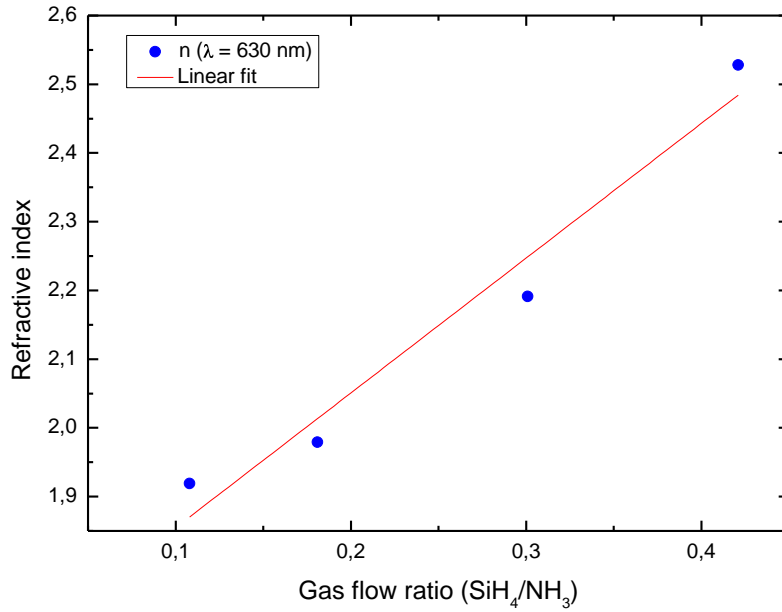
Figure 57: **Refractive index as a function of gas flow ratio for a-SiNₓ:H thin films deposited by remote PECVD. The data are fitted by linear regression.**

In Figure 58, the film thicknesses and corresponding deposition rates are given, and thicknesses ranging from 68 to 135 nm were found. In the deposition system used, adjusting the deposition time is not possible, and adjusting the gas flow ratio will affect the deposition rate. Hence, more work is needed in order to investigate the effect of individual gas flows and total pressure, in order to control film composition and deposition rates in the system.
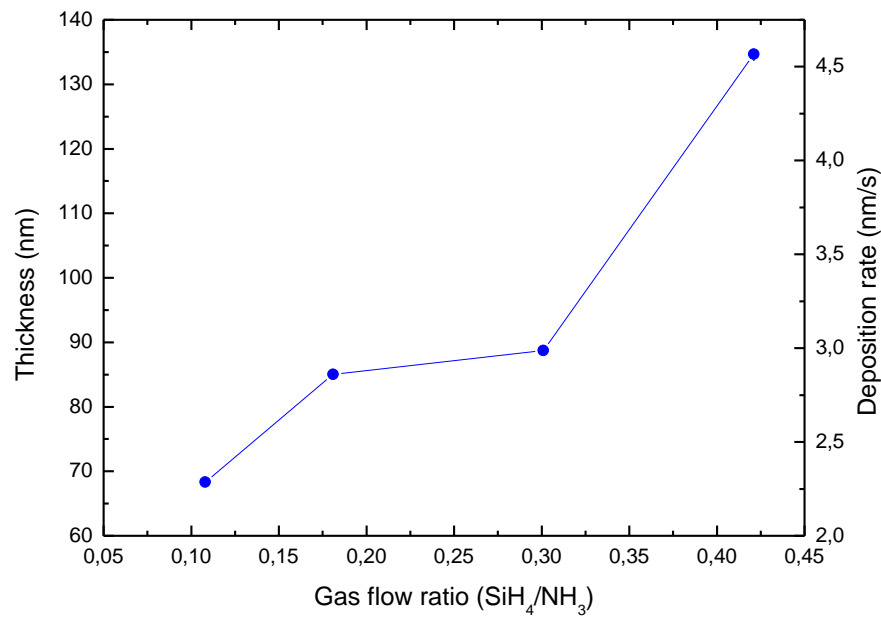
Figure 58: **Film thickness and corresponding deposition rate for different gas flow ratios in the remote PECVD system used.**

The highest deposition rate, 4.5 nm/s for sample 4, is slightly lower than the deposition rates >6 nm/s given in the OTB DEPx 2400 system specifications. In the specialization project, deposition rates for films deposited by the Plasmalab System 133 from Oxford Instruments were estimated, and the obtained values are in the range 0.25—0.35 nm/s [43]. Hence the films deposited by remote PECVD have a considerably larger deposition rate than films deposited by direct PECVD, emphasizing the advantage of using remote systems industrially. However, more work is needed in order to optimize the process for higher deposition rate.

4.4.2 Lifetime measurements

Lifetime measurements by QSSPC were conducted for as-deposited and fired samples, and the lifetime at injection level 1×10^{15} cm^{-3} is plotted against gas flow ratio in Figure 59. The measured lifetimes were in the range 12—67 µs, corresponding to SVRs in the range 205—1230 cm/s. Compared to the results reported in literature [4] and the lifetimes measured for the direct PECVD samples, the measured values for remote PECVD are much lower. This is as expected, because the deposition process in the remote PECVD system has not yet been optimized for surface passivation. For the as-deposited samples, an increase in lifetime with refractive index is observed, resembling the trend found in Section 4.3.2 for the thin films deposited by direct PECVD.
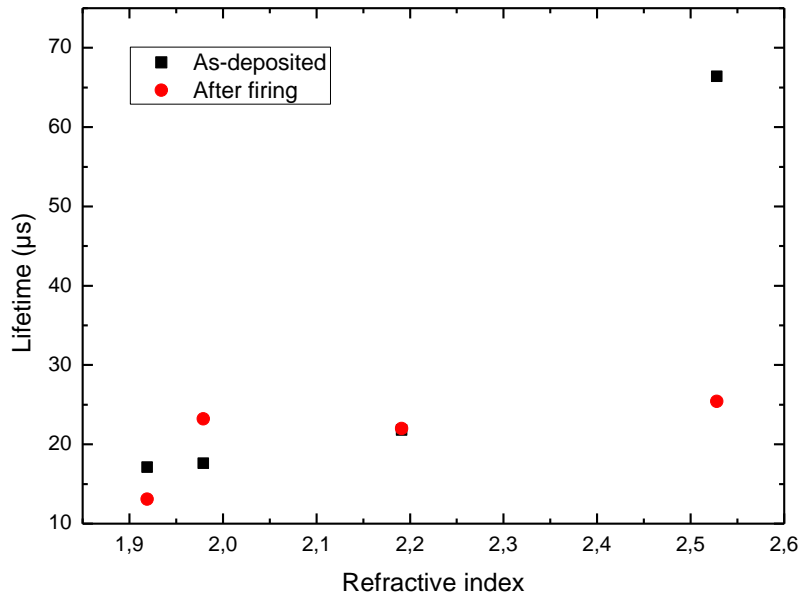
Figure 59:   Lifetime at injection level 1×10^{15} cm^{-3} versus refractive index for as-deposited and fired versions of sample 1—4, deposited using remote PECVD.

Firing did not consistently affect the lifetime of the samples, indicating an absence of hydrogen diffusing into the silicon. Several explanations for this observation are possible [4, 38]:

- The hydrogen concentration in the film is low
- The hydrogen in the film is loosely bound, and evaporates during firing
- The hydrogen in the film is tightly bound and does not diffuse during firing

Further investigations are needed to determine the cause of the poor passivation properties and improve the effect of firing, and accordingly a detailed analysis of the chemical composition and bond densities would be useful.

4.4.3   Fixed charge densities

In order to estimate fixed charge density and investigate charging and leakage currents, C-V measurements were conducted at the a-SiN$_x$:H films deposited by remote PECVD. 3 voltage sweeps at 1 MHz were performed on each sample. Sweep 1 started at 0 V in order to estimate the initial charge distribution in the film, and sweep 2 was done to check the effect of the previous sweep on the sample. Sweep 3 was conducted to investigate whether soaking had an effect on the measurement.

C-V curves of samples with three different refractive indices are given in Figure 60a-c. The C-V curve for sample 2 (n = 1.98, d = 85 nm) is given in Figure 60a. Similar behavior was observed for Sample 1 (n = 1.92, d = 68 nm). Experiments showed that measurement history had little

effect on capacitance, as only a very small shift in the curve was observed for the different sweeps. In Figure 60b the C-V characteristic of sample 3 (n = 2.19, d = 89 nm) is given. A shift in the curve is observed for consecutive measurements, as well as for the measurement starting with a soaking at 8 V. Figure 60c shows the C-V curve of sample 4 (n = 2.53, d = 135 nm), and here the size of the capacitance shift has decreased. No leakage currents were observed for samples 1-4.

Further analysis of the C-V curves gives estimates of flat band voltage and fixed charge density, using equations 13—17. The resulting estimates for fixed charge density are given in Figure 61, together with the absolute value of the shifts in flat band voltage. The obtained values for Q_f are in the range 2.1–3.2×10^{12} cm^{-2} and the larges shift in flat band voltage is found for sample 3 with refractive index 2.19. These results agree with the observations in Section 4.3.3 for a-SiN$_x$:H deposited by direct PECVD, where the estimated values for Q_f were in the range 1—9×10^{11} cm^{-2} and the maximum shift in flat band voltage of ~3.5 V was observed at n = 2.2. However, for the remote PECVD films the fixed charge density is slightly higher and the effect of charging was smaller and limited to the sample with refractive index 2.19. No charging was observed for sample 2 with n = 1.97. This observation combined with the absence of leakage currents, suggest stronger bonds for a-SiN$_x$:H deposited by remote PECVD compared to direct PECVD. Electrons and holes cannot travel as easily in the insulating thin film, and hence the effect of charging and leakage currents is reduced. The absence of leakage currents observed for sample 4, with the highest refractive index, can be explained by the large film thickness counteracting the effect of band gap narrowing.
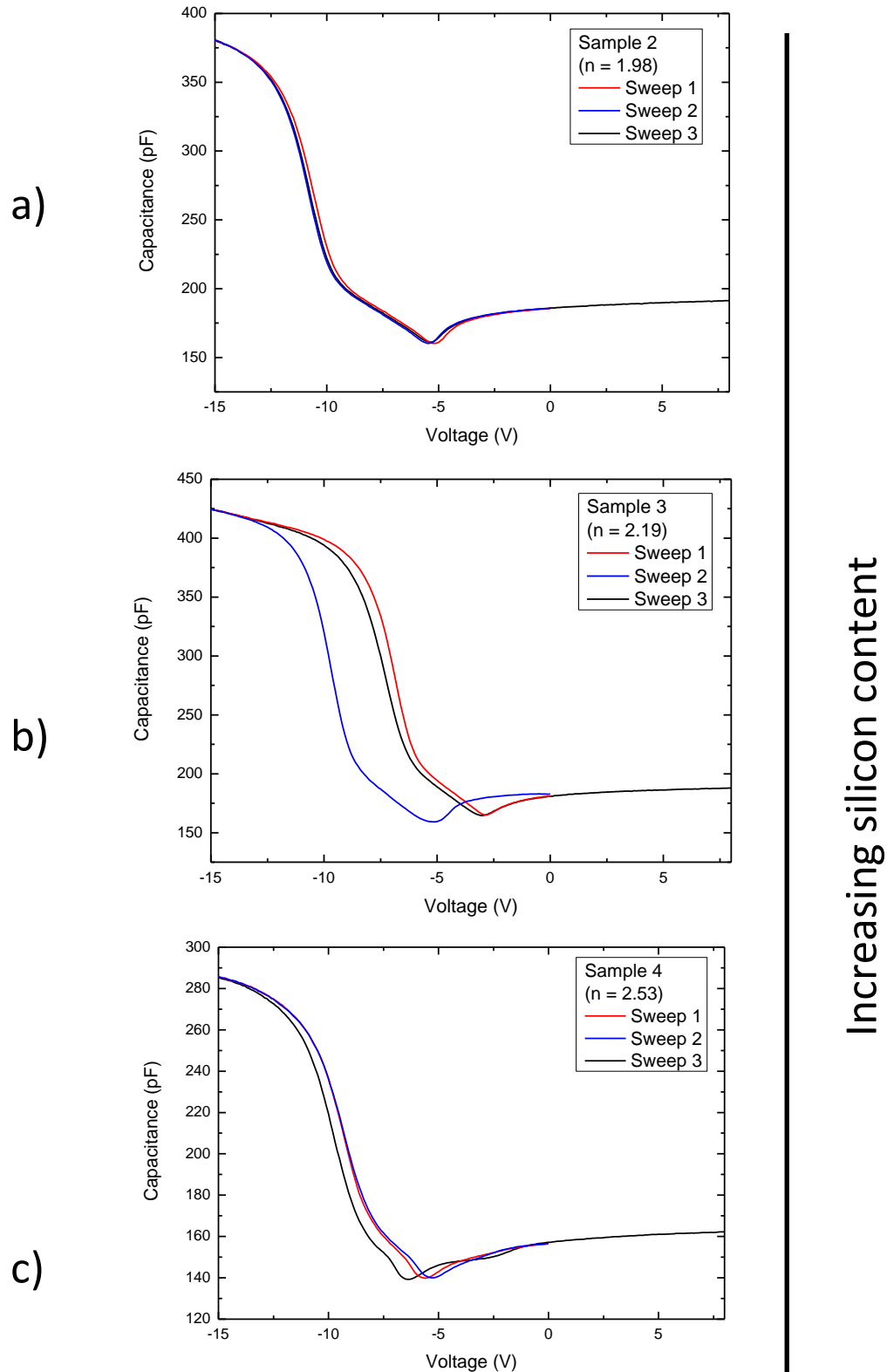
Figure 60: **C-V curves at 1 MHz for samples with increasing refractive index and silicon content: a) sample 2 with *n* = 1.98 and *d* = 85 nm b) sample 3 with *n* = 2.19 and *d* = 89 nm c) sample 4 with *n* = 2.53 and *d* = 135 nm. Sweep 1 and Sweep 2 were from 0 V to -10 V, and Sweep 3 was from 8 V to -10 V.**
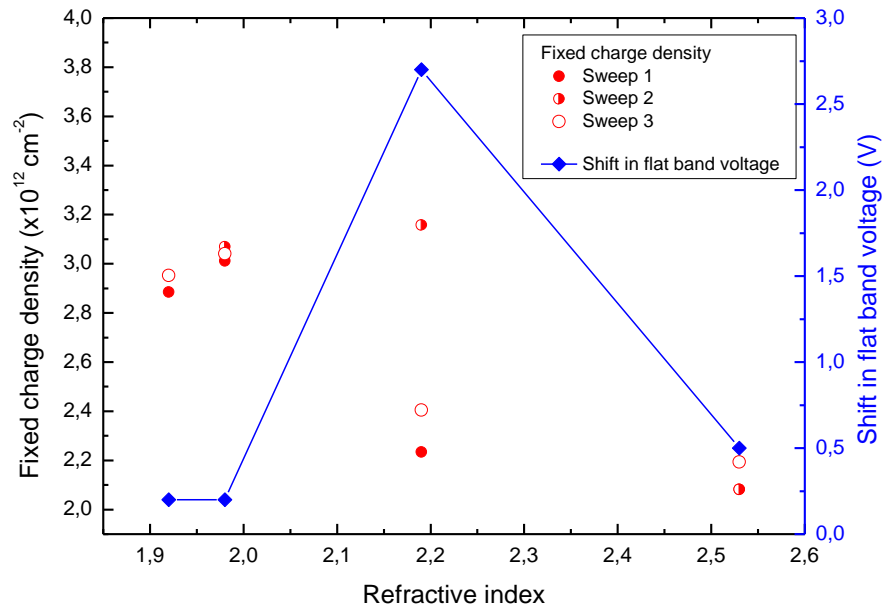
Figure 61: **Fixed charge density versus refractive index for samples 1-4, showing data from three voltage sweeps: Sweep 1 from 0 V to -10 V, Sweep 2 from 0 V to -10 V and Sweep 3 from 8 V to -10 V. The blue curve is the absolute value of the shift in flat band voltage, representing the shifts in the C-V curve with measurement history.**

4.4.4 Density of interface traps

The conductance method with G-V and G-f measurements was used to determine D_{it}. Due to measurement noise, G-V measurements were performed at 30 kHz instead of 10 kHz. The analytical method was preferred for determining the peak magnitude because of a relatively large contribution from series resistance in accumulation, and resulted in fits of good quality for all samples. In Figure 62, the measured G-V curve for sample 2 is given, together with the calculated contributions from series resistance and the corrected curve. Normalized G-f curves for samples 1-4 are given in Figure 63.
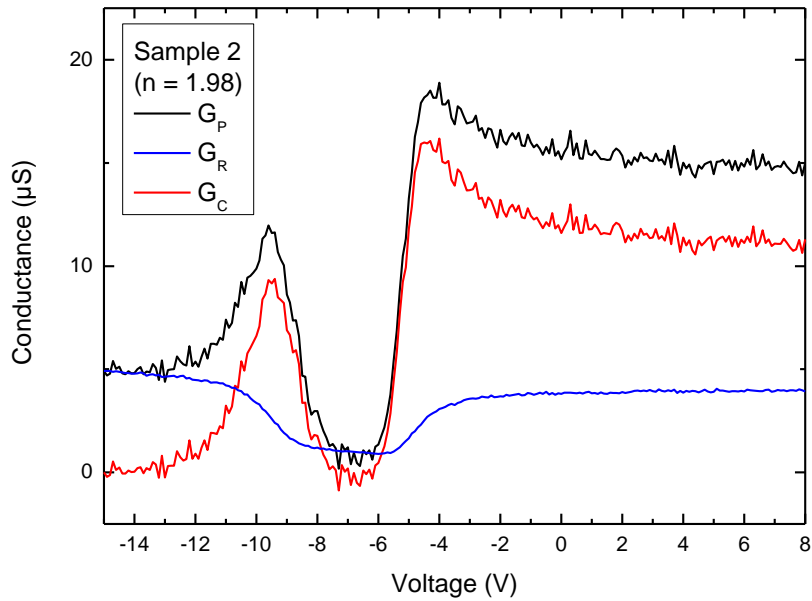
Figure 62: G-V curve for sample 2 showing the result of the analytical method for series resistance correction. *G$_P$* is the measured conductance, *G$_R$* is the contribution from series resistance and *G$_C$* is the corrected conductance.
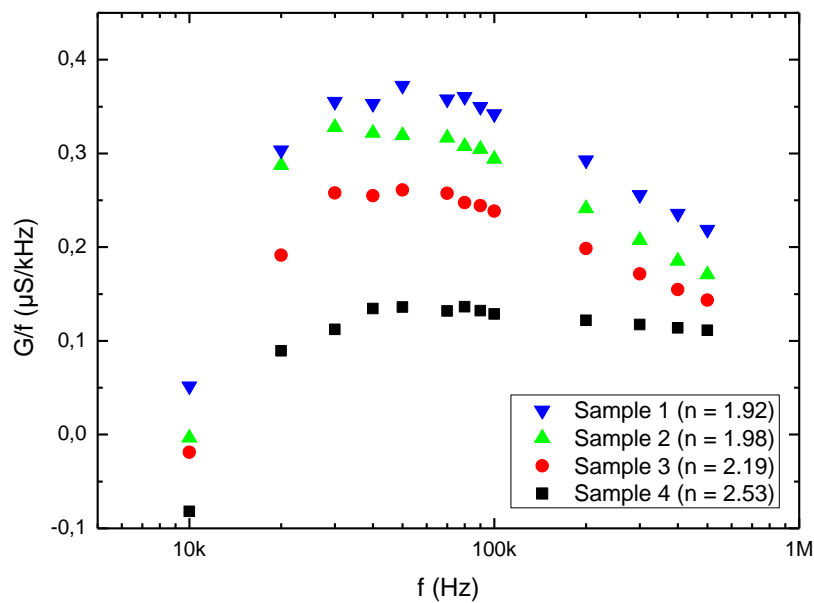
Figure 63: Normalized conductance versus frequency for as-deposited samples 1-4 deposited by remote PECVD.

Obtained values for the density of interface traps were in the range 4.2×10^{10}—1.07×10^{11} $eV^{-1}cm^{-2}$ for both methods and D_{it} is plotted against refractive index in Figure 64. G-f and G-V measurements resulted in similar values for D_{it}, with a small deviation for sample 3. A trend with decreasing D_{it} for increasing refractive index is observed. The investigations of samples 51-57 deposited by direct PECVD, resulted in D_{it} values in the range 1—4×10^{10} $eV^{-1}cm^{-2}$ from G-V and 3.9—4.8×10^{10} $eV^{-1}cm^{-2}$ from G-f measurements. Comparing the obtained values for sample 1-4 to these results, shows that the films deposited by remote PECVD have a higher density of interface traps. This corresponds well to the low measured lifetimes, indicating that the poor surface passivation is caused by a large density of interface traps and a low degree of chemical passivation. The decreasing density of interface traps with increasing refractive index agrees with the trend with increasing lifetime with increasing refractive index shown in Figure 59.
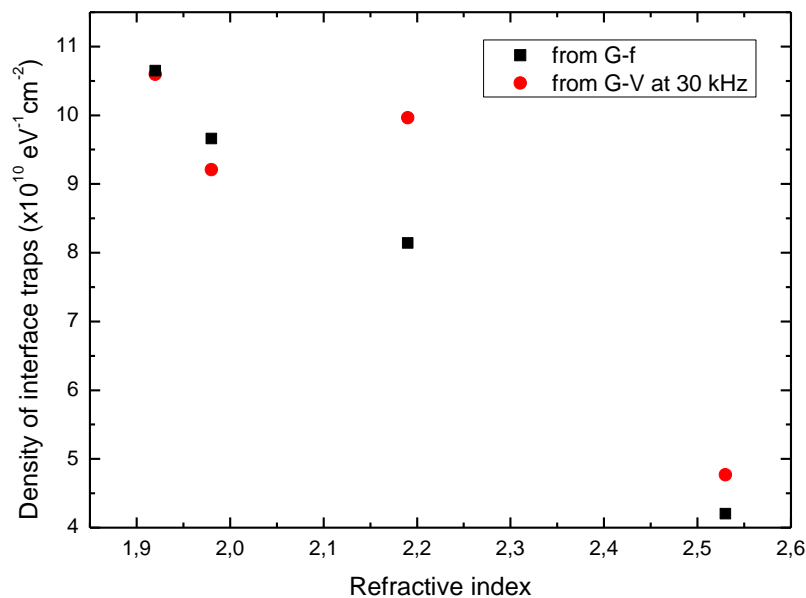
Figure 64: ***D_{it}* for different refractive indices, for films deposited by remote PECVD. Two methods for extracting *D_{it}* were performed: G-f and G-V measurements. The analytical approach to series resistance correction was used to determine *D_{it}* from G-V measurements at 30 kHz.**

4.4.5   Summary remote PECVD a-SiNx:H

Results from characterization of samples 1-4 with a-SiNx:H films deposited by remote PECVD are summarized in Table 18.

Adjusting gas flow ratio in the remote PECVD system resulted in films of varying stoichiometry and the refractive index of the film, and hence the silicon content, increased linearly with increasing gas flow ratio. However, changing the gas flows also affected the deposition rate. As the deposition time is constant, more work is needed in order to control film thickness.

A low measured lifetime and high density of interface traps revealed poor passivation properties, and firing had no effect on the measured lifetime. A slight increase in lifetime with increasing refractive index is explained by an improvement in the chemical passivation due to a decreasing D_{it}. No trend with respect to fixed charge density was observed, even though the non-ideal effects in the C-V characteristics were less pronounced than for samples deposited by direct PECVD. Charging, reflected in shifts in flat band voltage, was observed for sample 3 only, and leakage currents were not detected for any of the samples deposited by remote PECVD.

For the present, the a-SiNx:H films deposited by the OTB DEPx 2400 system can serve as decent anti-reflection coatings, as the refractive index and thickness can be controlled. Particularly sample 2 has the optical properties required for an ARC on a solar cell [32-34]. However, the investigations performed here strongly suggest that optimization of the deposition process is needed in order to achieve good surface passivation properties, and for the a-SiNx:H film to function as a combined ARC and surface passivation layer.

Table 18:   Summary of properties of a-SiNx:H deposited by remote PECVD. *d* is the film thickness, *n* is the refractive index, τ_{eff} is the effective measured lifetime, Q_f the fixed charge density, and D_{it} the density of interface traps. The films are categorized by composition according to refractive index.

Sample number	*d* (nm)	*n*	*Composition*	τ_{eff} (µs)		Q_f (×10¹² cm⁻²)	D_{it} (×10¹⁰ eV⁻¹cm⁻²)
				As-dep.	Fired		
1	68	1.92	N-rich	17	13	2.9—3.0	10.6—10.7
2	85	1.98		18	23	3.0—3.1	9.2—9.7
3	89	2.19	Intermediate	22	22	2.2—3.2	8.1—10.0
4	135	2.53	Si-rich	66	25	2.1—2.2	4.2—4.8

4.5 Carrier transport and charging in a-SiN$_x$:H

4.5.1 Investigation of leakage currents by I-V measurements

Current-voltage measurements were performed on samples with varying silicon content, and the resulting curves for refractive indices 2.04, 2.36 and 2.51 are given in Figure 65. As expected, the leakage currents increase with increasing refractive index, due to band gap narrowing with increasing silicon content.
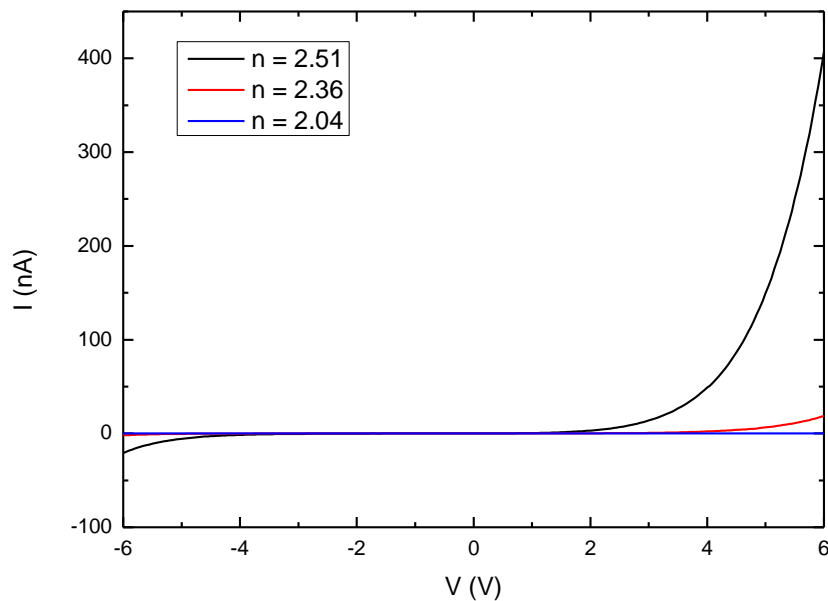
Figure 65:   I-V characteristics of samples 54c-1, 56c-1 and 57c-1, with refractive indices 2.04, 2.36 and 2.51, respectively.

Further investigations were carried out on sample 57 with *n* = 2.51, and I-V characteristics for temperatures from room temperature to 200 °C are given in Figure 66a-b. The shape of the I-V curve resemble previously reported I-V characteristics for PECVD a-SiN$_x$:H [10]. Due to the increase in leakage currents with increasing temperature, tunneling can be eliminated as the dominating transport mechanism. From the logarithmic plot in Figure 66b, it is clear that the I-V curve is not symmetric, as the current is almost a decade larger for positive biases than for negative. This favors a Schottky type of conduction [20, 40].

Figure 66: I-V characteristics for sample 57c-1 with refractive index 2.51 at temperatures in the interval 295—473 K: a) normal I-V curve, b) I-V curve with logarithmic current axis.

In order to investigate the linearity of the experimental data with respect to Schottky and Poole-Frenkel models, ln (I) vs. $V^{1/2}$ and ln (I/V) vs. $V^{1/2}$ plots were made for different temperatures, and the resulting graphs are given for positive and negative biases in Figure 67a-d. Similarly, ln (I/T^2) vs. T^{-1} and ln (I) vs. T^{-1} plots for different applied biases are given in Figure 68. The average coefficients of determination (r^2) for the linear fits are given in Table 19.

Table 19: **Coefficients of determination from linear fits to Schottky and Poole-Frenkel models. Current-voltage values are averaged over measurements on 5 different temperatures, and current-temperature values are averaged over measurements on 4 different biases.**

Model	Bias	Current-voltage	Current-temperature
Schottky	Positive	0.973	0.998
	Negative	0.978	0.991
Poole-Frenkel	Positive	0.982	0.998
	Negative	0.898	0.994
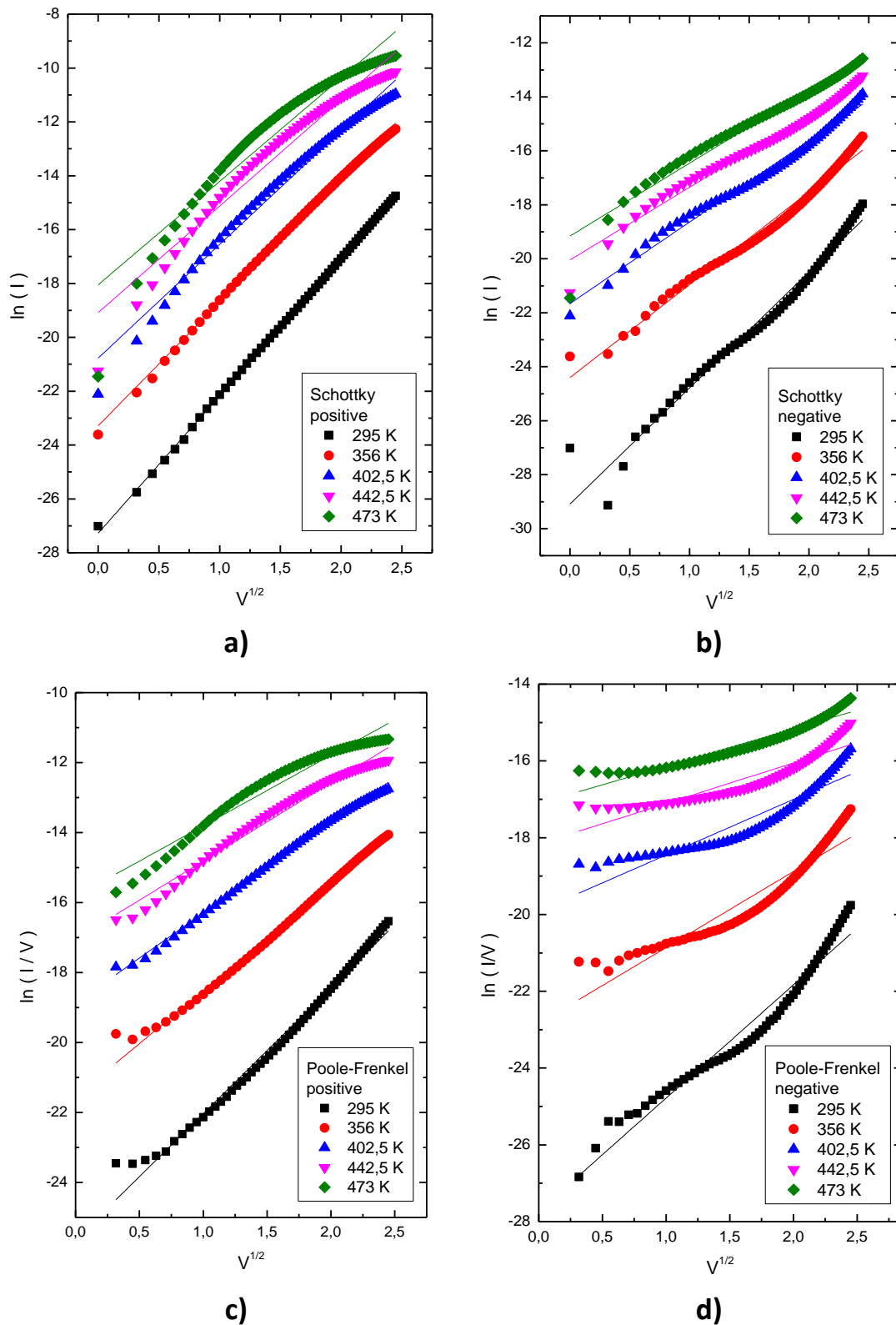
Figure 67: Plots of I-V data with linear fits to Schottky and Poole-Frenkel models for different temperatures: a) Schottky model ln (*I*) vs. $V^{1/2}$ for a) positive and b) negative biases, Poole-Frenkel model ln (*I/V*) vs. $V^{1/2}$ for c) positive and d) negative biases.
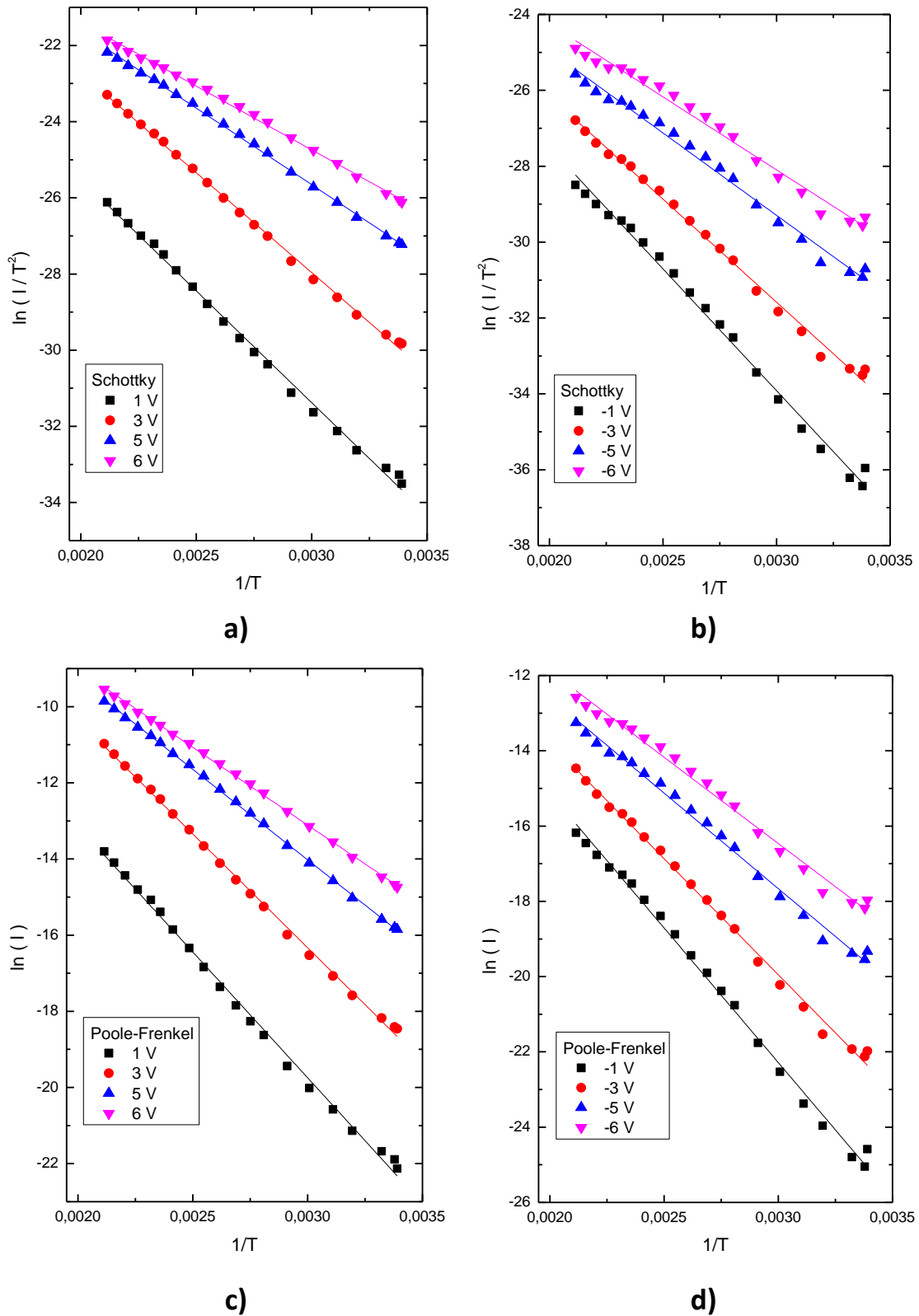
Figure 68: Plots of I-T data with linear fits to Schottky and Poole-Frenkel models for different voltages: a) Schottky model ln (I/T^2) vs. T^{-1} for a) positive and b) negative biases, Poole-Frenkel model ln (I) vs. T^{-1} for c) positive and d) negative biases.

Near linear behavior was observed for both models, however it is not possible to distinguish between the Schottky and Poole-Frenkel models with respect the coefficients of determination. This is as expected, and in accordance with the observations of Yeargan and Taylor [40]. Additionally some aspects of the linearized plots are worth noting:

- The I-T plots were more linear than the I-V plots
- Positive biases showed higher linearity than negative biases
- The I-V plots were more linear for larger voltages

Higher degree of linearity for I-T plots could be caused by the smaller amount of data points, or the small temperature interval used. The lower degree of linearity observed for negative bias and the poorer fits for lower applied voltages suggest a more complex conduction mechanism in the region with lower currents. These observations combined with the smaller temperature dependence in this region shows a contribution from tunneling to be probable, as observed by Jeon et al. and Sinha and [18, 19]. Alternatively, the deviations from the linear trends at lower applied fields could be explained by the voltage drop over the depletion region in the silicon. Hence, the assumption that the applied electric field is given by the applied voltage and the insulator thickness, $E = V/d$, is not valid.

Estimates of the dynamic permittivity and barrier height were extracted from the slopes of the graphs in Figure 67 and Figure 68 according to the equations in Table 2, and are summarized in Table 20. Both the Schottky and Poole-Frenkel models give larger permittivities for negative bias. And over all, the Poole-Frenkel model results in values for the permittivity one order of magnitude higher than the Schottky model. Compared to the values found in literature, for a permittivity in the range 1.8—6.5 [19, 20, 22], the Poole-Frenkel model gives the closest values for positive bias, and the Schottky model gives the best fit for negative bias. Since the refractive index of the sample is 2.51, a dynamic permittivity $\epsilon_i = n^2 \approx 6.3$ is expected, indicating a Poole-Frenkel mechanism. The obtained values for the barrier height correspond well to the values reported in literature, around 0.6 —1.7 eV [19-22], and do not favor either conduction mechanism.

Table 20: **Estimated dynamic permittivities and barrier heights from linear fits to Schottky and Poole-Frenkel models. The obtained permittivities are average values with standard deviations from I-V measurements on 5 different temperatures, and barrier heights are average values with standard deviations from I-T plots on 4 different biases.**

Model	Bias	ε_i	φ_B (eV)
Schottky	Positive	0.74 ± 0.10	0.67 ± 0.02
	Negative	1.35 ± 0.07	0.63 ± 0.03
Poole-Frenkel	Positive	7.9 ± 0.7	1.01 ± 0.09
	Negative	26 ± 11	0.60 ± 0.06

Results from literature show a general agreement that the Poole-Frenkel mechanism is dominating. From our experiments, however, it is not possible to conclude with one conduction mechanism for the leakage currents in our a-SiN$_x$:H thin films. The analysis of I-V and I-T plots do show that tunneling is unlikely, but further analysis do not succeed in distinguishing between Schottky and Poole-Frenkel transport. However, the asymmetry in the measurements with respect to measurement polarity does indicate that a Schottky type of transport is present. Additionally, the poorer fits to Schottky and Poole-Frenkel models for smaller currents suggest a contribution from another mechanism, for instance tunneling, at lower applied bias.

Another reason as to why no model fits the data perfectly is that the I-V measurements were not performed in steady state. The current is time dependent, as shown in a current-time measurement performed at sample 57c-1 in Figure 69. Charging in the insulator could explain this effect, as trapping and detrapping of electrons or holes in the a-SiN$_x$:H thin film would contribute to the leakage current.
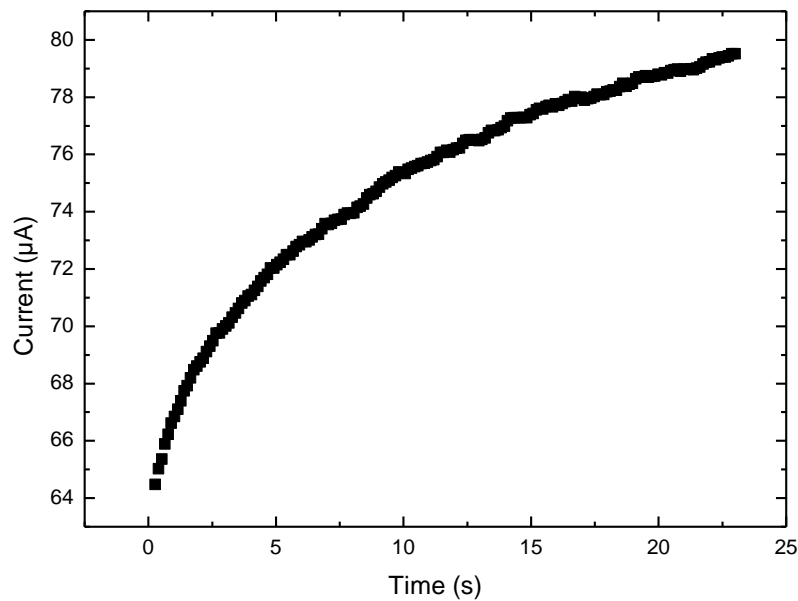
Figure 69: **Leakage current as a function of time, for an applied bias of 10 V. The measurement is performed on sample 57c-1.**

4.5.2   Investigation of charging by C-V measurements

In order to investigate the nature of the non-ideal dependence of V_{fb} and Q_f on measurement history, C-V measurements were performed on a series of samples with varying thickness. a-SiN$_x$:H was-deposited on samples 32a-h with varying deposition times, in order to create films of different thicknesses. From previously determined deposition rates, the thicknesses of the samples were calculated, and the values are summarized in Table 21.

Table 21:   Overview of estimated film thicknesses for a-SiN$_x$:H films deposited with varying deposition time.

Sample number	32a	32b	32c	32d	32e	32f	32g	32h
Film thickness (nm)	43	59	75	91	107	123	139	155

As described in Section 4.2.1 and Section 4.4.3, shifts in flat band voltage with measurement history is interpreted as changes in the fixed charge distribution Q_f caused by charging and decharging of K-centers. Samples 32a-h were exposed to a series of measurements to study the maximum amount of both positive and negative charging in the a-SiNx:H capacitors. A total of 15 sweeps were performed on each sample, and the full C-V measurement procedure is given in Appendix B. Sweep 1 is the initial sweep, and should give the initial charge distribution in the film. Sweeps 2-10 were performed to obtain a shift in the C-V curve towards negative voltages, and sweep 10 gives the largest shift and the most negative flat band voltage. Sweeps 11-15 were performed to obtain a shift towards positive voltages, and sweep 15 gives the largest shift in the positive direction. In Figure 70, the C-V curves of sample 32c are given for sweeps 1, 10 and 15, together with the obtained initial, most positive and most negative flat band voltages.
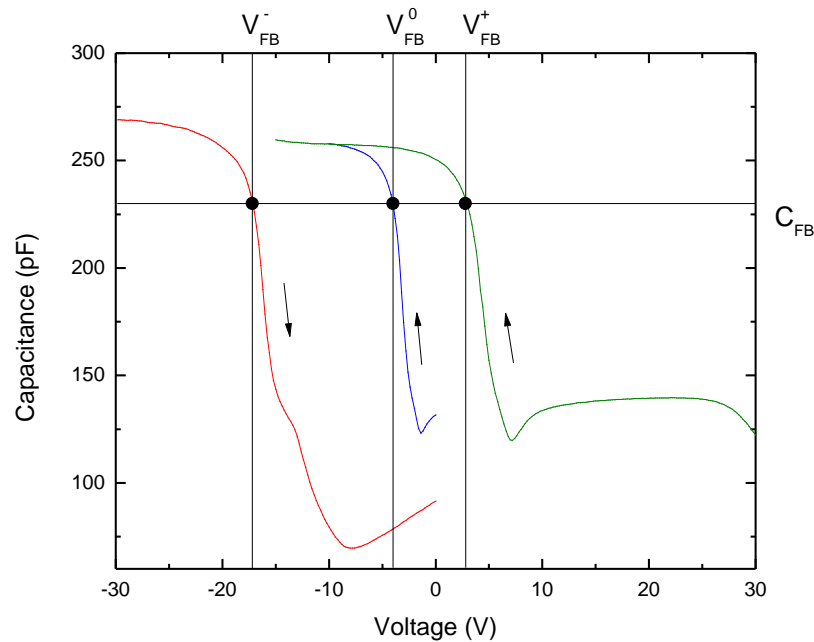
Figure 70: C-V curves for sweeps 1, 10 and 15, showing shifts in the curve depending on measurement history. Sweep directions are indicated, together with the flat band capacitance and – voltages. V$_{FB}^0$ is the initial flat band voltage, V$_{FB}^-$ the most negative and V$_{FB}^+$ the most positive flat band voltage observed during the measurement procedure. These measurements were performed on sample 32c, and the data from the reverse sweep of sweeps 1 and 15 are left out for clarity.

The resulting C-V curves were analyzed, extracting V_{fb} and Q_f for sweeps 1, 10 and 15. For samples 32a-b, the structure did not sustain the positive bias, and suffered from break down. The obtained values were taken from sweep 13 for sample 32a and 12 for sample 32b, before break down of the structure. In Figure 71a, V_{fb} is plotted against film thickness. For sweep 1, the flat band voltage is decreasing towards more negative values for increasing thickness. The negative soak causes a larger and more rapid decrease in V_{fb}. Reversing the soak direction causes V_{fb} to increase to positive values. In Figure 71b, the corresponding values for Q_f are shown. The initial concentration of positive charges in the films were in the interval 0.2—0.8×10^{12} cm^{-2}, whereas for sweep 10 the concentrations had increased to 1.8—5.0×10^{12} cm^{-2}. Positive soaking of the samples effectively removed the large amount of positive charge, and resulted in negatively charged films for the films thicker than 50 nm. For sweep 15, Q_f values from +0.1×10^{12} cm^{-2} to −1.7×10^{12} cm^{-2} were found.

Saturation of flat band voltage and fixed charge density for increasing film thicknesses was not observed. This suggests that the most common model for a-SiN$_x$:H thin films on silicon substrates, with the fixed charges distributed ~20 nm into the a-SiN$_x$:H film, is incorrect. According to the model, the initial charge distribution should be independent of film thickness. Additionally, the amount of introduced charges should saturate for higher film thickness when

exposed to the positive and negative soak indicating that all available defects are charged. Our observations, on the other hand, strongly suggest an increasing initial charge distribution with increasing film thickness (black squares in Figure 71) and a strong increase in $|Q_f|$ with increasing film thickness when exposed to positive and negative soaking (red circles and blue triangles). These experiments show that the formation of positive or negative charges in a-SiN$_x$:H is not limited to the 20 nm interface region towards silicon, on the contrary they seem to be distributed through the entire film and the applied bias determines the formation of fixed charges. Because the increase in Q_f is larger for negative soaking, the formation of positive charges appear to have a smaller activation energy than the formation of negative charges. The observed formation of positive and negative charges in the a-SiN$_x$:H films can be related to the charging and decharging of K-centers, and our experiments show that the concentration of available K-centers depends on the film thickness and on the applied bias.
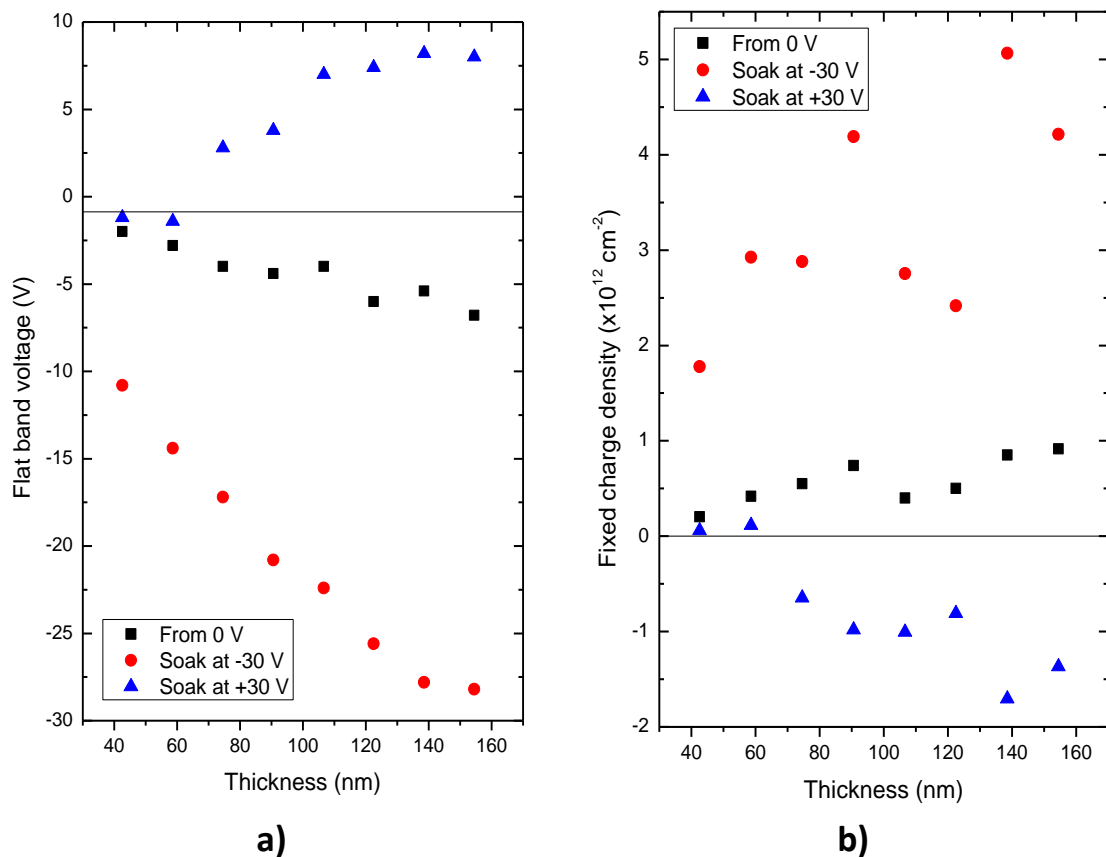
Figure 71: **a) Flat band voltage and b) fixed charge density versus film thickness for Sweep 1 from 0 V, Sweep 10 from -30 V and Sweep 15 from 30 V. The line in a) at -0.87 V represents a system with zero fixed charge.**

5 Conclusion

In this work, the passivation properties of amorphous silicon nitride thin films for crystalline silicon solar cell applications were investigated, with emphasis on electrical characterization. Based on the findings from the experimental investigations, the following is concluded:

- Electrical characterization can be used to determine the density of interface traps and fixed charge density in the interface region between silicon nitride and silicon
    - Values for the fixed charge density were estimated in the range $0.1–3.0\times10^{12}$ cm^{-2} as derived from by C-V measurements in the dark at room temperature
    - Values for the density of interface states were estimated in the range $0.1–1.1\times10^{11}$ eV^{-1} cm^{-2} as derived from G-V and G-f measurements in the dark at room temperature
- Chemical passivation was successfully linked to the measured effective lifetime through the density of interface traps, as high values of D_{it} were found for samples with low effective lifetime, and vice versa
- Field-effect passivation was not successfully linked to the measured effective lifetime, mainly because the fixed charge density proved to be difficult to determine due to charging and leakage currents
- Increasing inversion region capacitance with decreasing measurement frequency was related to the contribution from inversion layer electrons outside the MIS area
- Electrical characterization, in addition to lifetime measurements and spectroscopic ellipsometry, was used to determine the film properties of a-SiN$_x$:H deposited by two different PECVD systems
    - Varying the gas flow ratio resulted in films of varying stoichiometry for both deposition methods
    - A heat treatment corresponding to the screen printing firing process was found to have a positive effect on the passivation properties of films deposited by direct PECVD, but did not consistently affect films deposited by remote PECVD
    - For thin films deposited by direct PECVD, lifetimes of 300 µs, corresponding to surface recombination velocities of 30 cm/s were obtained for Si-rich films after the heat treatment
    - For thin films deposited by remote PECVD, lifetimes of 70 µs, corresponding to surface recombination velocities of 210 cm/s were obtained for Si-rich films
    - A maximum increase of 25 % in the surface recombination velocity after illumination was found for films deposited by direct PECVD, and light induced degradation of the Czochralski substrate made interpretation of data challenging
    - Leakage currents were observed for films deposited by direct PECVD only, and were most pronounced for Si-rich films.

- Charging caused by trapping and detrapping of carriers at K-centers was found to be most dominating for a-SiN$_x$:H films with refractive index ~2.2
- The fixed charge density increased with increasing film thickness, proving that the present model, with fixed charges located ~20 nm into the a-SiN$_x$:H layer, is an oversimplification
- The transport mechanism for leakage currents through the insulating a-SiN$_x$:H layer was found to be asymmetric, favoring a Schottky mechanism

5.1 Further work

Additional improvement of the passivation properties of a-SiN$_x$:H thin films may be obtained by further investigations of the relation between process parameters and material properties. The electrical characterization techniques adopted in this work are well suited to investigation of the interface properties. Suggestions for further work may include:

- Testing the influence of other deposition parameters, such as pressure, deposition rate and plasma power on electrical interface properties for both deposition systems
- Optimizing the deposition parameters for the OTB DEPx 2400 system, in order to improve the passivation quality
- Investigate the degradation of passivation layers deposited on float zone substrate, in order to avoid contributions from light induced degradation
- Investigate the effects of charging on leakage currents by applying voltage pulses to current-time measurements
- Investigate the effect of temperature on the thin film electrical properties like capacitance and conductance
- Implementing the deposition recipes giving the best passivation properties to crystalline silicon solar cells in order to investigate the effect of the a-SiN$_x$:H layer on the cell efficiency and stability

6 References

1. Thomas, M.G., H.N. Post, and R. Deblasio, *Photovoltaic systems: an end-of-millennium review.* Progress in Photovoltaics: Research and Applications, 1999. **7**(1), pp. 1-19.

2. Kazmerski, L.L., *Photovoltaics: A review of cell and module technologies.* Renewable and Sustainable Energy Reviews, 1997. **1**(1-2), pp. 71-170.

3. Aberle, A.G., *Surface passivation of crystalline silicon solar cells: a review.* Progress in Photovoltaics: Research and Applications, 2000. **8**(5), pp. 473-487.

4. Aberle, A.G., *Crystalline silicon solar cells: advanced surface passivation and analysis.* 1999, Sydney: University of New South Wales. Centre for Photovoltaic Engineering.

5. Tucci, M., et al., *Laser fired back contact for silicon solar cells.* Thin Solid Films, 2008. **516**(20), pp. 6767-6770.

6. Lauinger, T., et al., *Optimization and characterization of remote plasma-enhanced chemical vapor deposition silicon nitride for the passivation of p-type crystalline silicon surfaces.* Journal of Vacuum Science & Technology A: Vacuum, Surfaces, and Films, 1998. **16**(2), pp. 530-543.

7. Schmidt, J. and M. Kerr, *Highest-quality surface passivation of low-resistivity p-type silicon using stoichiometric PECVD silicon nitride.* Solar Energy Materials and Solar Cells, 2001. **65**(1-4), pp. 585-591.

8. Schmidt, J., M. Kerr, and A. Cuevas, *Surface passivation of silicon solar cells using plasma-enhanced chemical-vapour-deposited SiN films and thin thermal SiO 2 /plasma SiN stacks.* Semiconductor Science and Technology, 2001. **16**(3), p. 164.

9. Lee, K.R., K.B. Sundaram, and D.C. Malocha, *Deposition parameters studies of silicon nitride films prepared by plasma-enhanced CVD process using silane-ammonia.* Journal of Materials Science: Materials in Electronics, 1993. **4**(4), pp. 283-287.

10. Yoo, J., et al., *Study on hydrogenated silicon nitride for application of high efficiency crystalline silicon solar cells.* Solar Energy Materials and Solar Cells, 2011. **95**(1), pp. 7-10.

11. Moschner, J.D., et al., *High-quality surface passivation of silicon solar cells in an industrial-type inline plasma silicon nitride deposition system.* Progress in Photovoltaics, 2004. **12**(1), pp. 21-31.

12. Soppe, W., H. Rieffe, and A. Weeber, *Bulk and surface passivation of silicon solar cells accomplished by silicon nitride deposited on industrial scale by microwave PECVD.* Progress in Photovoltaics, 2005. **13**(7), pp. 551-569.

13. Lelièvre, J.F., et al., *Study of the composition of hydrogenated silicon nitride SiNx:H for efficient surface and bulk passivation of silicon.* Solar Energy Materials and Solar Cells, 2009. **93**(8), pp. 1281-1289.

14. Lenkeit, B., et al., *Excellent thermal stability of remote plasma-enhanced chemical vapour deposited silicon nitride films for the rear of screen-printed bifacial silicon solar cells.* Solar Energy Materials and Solar Cells, 2001. **65**(1-4), pp. 317-323.

15. Beylier, G., et al., *Refined electrical analysis of two charge states transition characteristic of "borderless" silicon nitride.* Microelectronics Reliability, 2007. **47**(4-5), pp. 743-747.

16. Beylier, G., et al., *New Characterization Methodology of Borderless Silicon Nitride Charge Kinetics Using C-V Hysteresis Loops.* Journal of The Electrochemical Society, 2008. **155**(5), pp. H273-H279.

17.   Hielscher, F.H. and H.M. Preier, *Non-equilibrium C-V and I-V characteristics of metal-insulator-semiconductor capacitors.* Solid-State Electronics, 1969. **12**(7), pp. 527-538.

18.   Jeon, Y.-C., H.-Y. Lee, and S.-K. Joo, *I-V characteristics of electron-cyclotron-resonance plasma-enhanced chemical-vapor-deposition silicon nitride thin films.* Journal of Applied Physics, 1994. **75**(2), pp. 979-984.

19.   Sinha, A.K. and T.E. Smith, *Electrical properties of Si-N films deposited on silicon from reactive plasma.* Journal of Applied Physics, 1978. **49**(5), pp. 2756-2760.

20.   Sze, S.M., *Current Transport and Maximum Dielectric Strength of Silicon Nitride Films.* Journal of Applied Physics, 1967. **38**(7), pp. 2951-2956.

21.   Lowe, A.J., M.J. Powell, and S.R. Elliott, *The electronic properties of plasma-deposited films of hydrogenated amorphous SiN$_x$ (0<x<1.2).* Journal of Applied Physics, 1986. **59**(4), pp. 1251-1258.

22.   Maeda, M. and Y. Arita, *Electrical properties and their thermal stability for silicon nitride films prepared by plasma-enhanced deposition.* Journal of Applied Physics, 1982. **53**(10), pp. 6852-6856.

23.   Makino, T., *Composition and Structure Control by Source Gas Ratio in LPCVD SiN[sub x].* Journal of The Electrochemical Society, 1983. **130**(2), pp. 450-455.

24.   Dauwe, S., *Low-Temperature Surface Passivation of Crystalline Silicon and its Application to the Rear Side of Solar Cells*. 2004, Hannover.

25.   Streetman, B.G. and S. Banerjee, *Solid state electronic devices*. 2000, Upper Saddle River, N.J.: Prentice-Hall.

26.   Nicollian, E.H. and J.R. Brews, *MOS (metal oxide semiconductor) physics and technology*. 2003, Hoboken, N.J.: Wiley-Interscience.

27.   Schroder, D.K., *Semiconductor material and device characterization*. 3rd ed. 2006, Hoboken, N.J.: Wiley.

28.   Elmiger, J.R. and M. Kunst, *Investigation of charge carrier injection in silicon nitride silicon junctions.* Applied Physics Letters, 1996. **69**(4), pp. 517-519.

29.   De Wolf, S., et al., *Influence of stoichiometry of direct plasma-enhanced chemical vapor deposited SiNx films and silicon substrate surface roughness on surface passivation.* Journal of Applied Physics, 2005. **97**(6), pp. 1-8.

30.   Claassen, W.A.P., et al., *Characterization of Plasma Silicon Nitride Layers.* Journal of The Electrochemical Society, 1983. **130**(12), pp. 2419-2423.

31.   Mäckel, H. and R. Lüdemann, *Detailed study of the composition of hydrogenated SiN$_x$ layers for high-quality silicon surface passivation.* Journal of Applied Physics, 2002. **92**(5), p. 2602.

32.   Wright, D.N., E.S. Marstein, and A. Holt. *Double layer anti-reflective coatings for silicon solar cells*. in *Photovoltaic Specialists Conference, 2005. Conference Record of the Thirty-first IEEE*. 2005.

33.   Junghänel, M., et al. *Black Multicrystalline Solar Modules Using Novel Multilayer Antireflection Stacks*. in *25th European Photovoltaic Solar Energy Conference and Exhibition / 5th World Conference on Photovoltaic Energy Conversion*. 2010. Valencia, Spain.

34.   Abade, K.A., et al. *PECVD single-layer (SiN:H) and double-layer (SiN:H/SiO$_2$) ARC on mono and multicrystalline silicon solar cells*. in *Photovoltaic Specialists Conference, 2000. Conference Record of the Twenty-Eighth IEEE*. 2000.

35.   Lau, W.S., S.J. Fonash, and J. Kanicki, *Stability of electrical properties of nitrogen-rich, silicon-rich, and stoichiometric silicon nitride films.* Journal of Applied Physics, 1989. **66**(6), pp. 2765-2767.

36.   Hezel, R. and R. Schörner, *Plasma Si nitride - A promising dielectric to achieve high quality silicon MIS/IL solar cells.* Journal of Applied Physics, 1981. **54**, pp. 3076-3079.

37. Aberle, A.G. and R. Hezel, *Progress in Low-temperature Surface Passivation of Silicon Solar Cells using Remote-plasma Silicon Nitride.* Progress in Photovoltaics: Research and Applications, 1997. **5**(1), pp. 29-50.

38. Hong, J., et al., *Influence of the high-temperature "firing" step on high-rate plasma deposited silicon nitride films used as bulk passivating antireflection coatings on silicon solar cells.* Journal of Vacuum Science & Technology B: Microelectronics and Nanometer Structures, 2003. **21**(5), pp. 2123-2132.

39. Sze, S.M. and K.K. Ng, *Physics of semiconductor devices*. 1969, Hoboken, N.J.: Wiley-Interscience.

40. Yeargan, J.R. and H.L. Taylor, *The Poole-Frenkel Effect with Compensation Present.* Journal of Applied Physics, 1968. **39**(12), pp. 5600-5604.

41. Jeon, M., S. Yoshiba, and K. Kamisako, *Hydrogenated amorphous silicon film as intrinsic passivation layer deposited at various temperatures using RF remote-PECVD technique.* Current Applied Physics, 2010. **10**(2, Supplement 1), pp. S237-S240.

42. Quirk, M. and J. Serda, *Semiconductor manufacturing technology*. 2001, Upper Saddle River, N.J.: Prentice Hall.

43. Helland, S., *Surface passivation using silicon nitride (a-SiN$_x$:H) for silicon based solar cells*. 2010, Norwegian University of Science and Technology: Trondheim.

44. Fujiwara, H., *Spectroscopic ellipsometry : principles and applications*. 2007, Chichester, England; Hoboken, NJ: John Wiley & Sons.

45. Sinton, R.A., A. Cuevas, and M. Stuckings. *Quasi-steady-state photoconductance, a new method for solar cell material and device characterization*. in *Photovoltaic Specialists Conference, 1996., Conference Record of the Twenty Fifth IEEE*. 1996.

46. Sinton Consulting, I., *WCT-120 Photoconductance Lifetime Tester and optional Suns-V$_{OC}$ Stage, User Manual*. 2006.

47. Wright, D.N., *Optical and passivating properties of hydrogenated amorphous silicon nitride deposited by plasma enhanced chemical vapour deposition for application on silicon solar cells*. 2008, University of Oslo: Oslo.

48. Haug, H., *Personal communication*. 2010: Department of Solar Energy, Institute for Energy Technology.

49. Schmidt, J. and A. Cuevas, *Electronic properties of light-induced recombination centers in boron-doped Czochralski silicon.* Journal of Applied Physics, 1999. **86**(6), pp. 3175-3180.

6 References

Appendix A: Deposition parameters

Set 1: Silane flow variation

Overview of deposition parameters for a-SiN$_x$:H on *p*-type Czochralski (CZ) silicon, Set 1: Silane flow variation. Deposited using Oxford Plasmalab System 133.

Sample number		Temp. (°C)	Power (W)	SiH$_4$ flow (sccm)	NH$_3$ flow (sccm)	N$_2$ flow (sccm)	Pressure (mTorr)	Time (min)	Double sided	Heat treat.
51	a	400	40	5	20	980	800	7.30	x	
	b	400	40	5	20	980	800	7.30	x	x
	c-1	400	40	5	20	980	800	7.30		
	c-2	400	40	5	20	980	800	7.30		x
52	a	400	40	10	20	980	800	7.21	x	
	b	400	40	10	20	980	800	7.21	x	x
	c-1	400	40	10	20	980	800	7.21		
	c-2	400	40	10	20	980	800	7.21		x
53	a	400	40	15	20	980	800	7.14	x	
	b	400	40	15	20	980	800	7.14	x	x
	c-1	400	40	15	20	980	800	7.14		
	c-2	400	40	15	20	980	800	7.14		x
54	a	400	40	20	20	980	800	7.06	x	
	b	400	40	20	20	980	800	7.06	x	x
	c-1	400	40	20	20	980	800	7.06		
	c-2	400	40	20	20	980	800	7.06		x
55	a	400	40	30	20	980	800	6.30	x	
	b	400	40	30	20	980	800	6.30	x	x
	c-1	400	40	30	20	980	800	6.30		
	c-2	400	40	30	20	980	800	6.30		x
	d	400	40	30	20	980	800	6.30	x	

Sample number		Temp. (°C)	Power (W)	SiH$_4$ flow (sccm)	NH$_3$ flow (sccm)	N$_2$ flow (sccm)	Pressure (mTorr)	Time (min)	Double sided	Heat treat.
56	a	400	40	40	20	980	800	5.88	x	
	b	400	40	40	20	980	800	5.88	x	
	c-1	400	40	40	20	980	800	5.88		x
	c-2	400	40	40	20	980	800	5.88		x
	d	400	40	30	20	980	800	6.30	x	
57	a	400	40	50	20	980	800	5.53	x	
	b	400	40	50	20	980	800	5.53	x	
	c-1	400	40	50	20	980	800	5.53		x
	c-2	400	40	50	20	980	800	5.53		x

Set 2: Time variation

Overview of deposition parameters for a-SiN$_x$:H on *p*-type Czochralski (CZ) silicon, Set 2: Time variation. Deposited using Oxford Plasmalab System 133.

Sample number		Temp. (°C)	Power (W)	SiH$_4$ flow (sccm)	NH$_3$ flow (sccm)	N$_2$ flow (sccm)	Pressure (mTorr)	Time (min:sec)	Double sided	Heat treat.
32	a	400	40	20	20	980	800	03:00		
	b	400	40	20	20	980	800	04:08		
	c	400	40	20	20	980	800	05:15		
	d	400	40	20	20	980	800	06:23		
	e	400	40	20	20	980	800	07:30		
	f	400	40	20	20	980	800	08:38		
	g	400	40	20	20	980	800	09:45		
	h	400	40	20	20	980	800	10:53		

Set 3: Gas flow ratio variation in remote PECVD

Overview of deposition parameters for a-SiN$_x$:H on p-type Czochralski (CZ) silicon, Set 3: Gas flow ratio variation in remote PECVD. Deposition is performed in the OTB DEPx 2400 system. Details on the SiH$_4$ and NH$_3$ gas flows for the three plasma sources are given in a separate table below.

Sample number		Temp. (°C)	Current (A)	Voltage (V)	Average gas flow ratio	Ar flow (slm)	Pressure (mTorr)	Time (s)	Double sided	Heat treat.
1	a	407±7	80	44.2	0.108	2	185	29.7	x	
	b	407±7	80	44.2	0.108	2	185	29.7	x	x
	c	407±7	80	44.2	0.108	2	185	29.7		
2	a	407±7	80	44.2	0.181	2	185	29.7	x	
	B	407±7	80	44.2	0.181	2	185	29.7	x	x
	c	407±7	80	44.2	0.181	2	185	29.7		
3	a	407±7	80	44.2	0.301	2	185	29.7	x	
	b	407±7	80	44.2	0.301	2	185	29.7	x	x
	c	407±7	80	44.2	0.301	2	185	29.7		
4	a	407±7	80	44.2	0.421	2	185	29.7	x	
	b	407±7	80	44.2	0.421	2	185	29.7	x	x
	c	407±7	80	44.2	0.421	2	185	29.7		

Details on the SiH$_4$ and NH$_3$ gas flows in Set 3: Gas flow ratio variation in remote PECVD.

Sample	Source 1			Source 2			Source 3		
	NH$_3$ (slm)	SiH$_4$ (slm)	Gas flow ratio	NH$_3$ (slm)	SiH$_4$ (slm)	Gas flow ratio	NH$_3$ (slm)	SiH$_4$ (slm)	Gas flow ratio
1	0.35	0.155	0.44	0.3	0.147	0.49	0.53	0.175	0.33
2	0.3	0.095	0.32	0.25	0.087	0.35	0.48	0.115	0.24
3	0.4	0.075	0.19	0.35	0.067	0.19	0.58	0.095	0.16
4	0.5	0.055	0.11	0.45	0.047	0.10	0.68	0.075	0.11

a-SiN$_x$:H /a-SiN$_x$:H stack

Overview of deposition parameters for the a-SiN$_x$:H/a-SiN$_x$:H stack deposited on *p*-type Czochralski (Cz) silicon. Deposited using Oxford Plasmalab System 133.

Sample/layer		Temp. (°C)	Power (W)	SiH$_4$ flow (sccm)	NH$_3$ flow (sccm)	N$_2$ flow (sccm)	Pressure (mTorr)	Time (min)	Double sided	Heat treat.
60d	1	400	40	50	20	980	800	6		
	2	400	40	10	20	980	800	6		

Films on various substrates

Overview of deposition parameters for various a-SiN$_x$:H films:

- Sample 26d and sample 33c from the specialization project work [43]
- Sample 31d, which was used in the laser-contact experiment
- Sample 28c, deposited on *n*-type silicon
- Sample 45c—d, deposited on FZ silicon

Deposited using Oxford Plasmalab System 133.

Sample number		Temp. (°C)	Power (W)	SiH$_4$ flow (sccm)	NH$_3$ flow (sccm)	N$_2$ flow (sccm)	Pressure (mTorr)	Time (min)	Double sided	Heat treat.
26d		400	40	20	20	980	800	6		x
33c		400	60	20	20	980	800	6		
31d		400	40	20	20	980	800	8		x
28c		400	40	20	20	980	800	6		
45	c	400	40	20	20	980	800	6	x	
	d	400	40	20	20	980	800	6	x	x

Appendix B: CV measurement procedure

Overview of measurement procedure for CV measurements on samples 32a-h with varying thicknesses. Sweeps 2-10 were performed to obtain a shift in the CV curve towards negative voltages, and sweeps 11-15 a shift towards positive voltages. The results obtained are described in Section 4.5.2.

Sweep number	Start voltage (V)	End voltage (V)	Soak time (s)	Reverse sweep
1	0	-10	0	Yes
2	0	-10	0	Yes
3	0	-10	0	Yes
4	0	-10	0	Yes
5	0	-20	0	Yes
6	0	-20	0	Yes
7	0	-30	0	Yes
8	0	-30	0	Yes
9	-30	0	30	No
10	-30	0	30	No
11	10	-15	30	Yes
12	10	-15	30	Yes
13	20	-15	30	Yes
14	20	-15	30	Yes
15	30	-15	30	No